Université du Québec
Institut National de la Recherche Scientifique
Énergie, Matériaux et Télécommunications

NOVEL TECHNIQUES FOR TERAHERTZ SUB-WAVELENGTH IMAGING

Par

Ho Sze Phing

Thèse présentée pour l'obtention du grade de
du grade de Philosophiae doctor (Ph.D.)
en Sciences de l'Énergie et des Matériaux

Jury d'évaluation

Président du jury et examinateur interne	Dr. Francois Vidal INRS-EMT
Examinateur externe	Dr. Arkady Major University of Manitoba
Examinateur externe	Dr. Pablo Bianucci University of Concordia
Directeur de recherche	Dr. Roberto Morandotti INRS-EMT
Codirecteur de recherche	Dr. Matteo Clerici Heriot-Watt University

ACKNOWLEDGEMENT

I am deeply indebted to my advisor, Prof. Roberto Morandotti, for his support and advice in the frontier research associated to THz science: my entire PhD endeavor would not have been possible without him. I benefitted from a wealth of opportunities and experiences during my time in Prof. Morandotti's group, which helped me to develop a degree of confidence, numerous laboratory skills, a diverse interdisciplinary knowledge, a degree of independence to direct my own research, the ability to improve my public speaking abilities and finally, to become a better-rounded researcher overall. I would also like to thank Prof. Jalil Ali, whose guidance and advice helped me develop the broad perspective I would use throughout my graduate career. His support and encouragement assisted me to persevere in completing the Ph. D. program.

My gratitude goes to Dr. Marco Peccianti and Dr. Matteo Clerici, for their tremendous patience and effort in guiding me throughout my doctoral studies. It would have been perhaps impossible to get the study done without their assistance, profession and expertise; I also acknowledge Dr. Alessia Pasquazi and Dr. Lucia Caspani, for their priceless theoretical support, which strengthen the validity of my experimental results. Their assistance enriches the content of my dissertation with important and meaningful theoretical findings. I would also like to thank Dr. Anna Mazhorova, for her suggestions and comments during the implementation of the experiment activities at the final stage of my study in the Ultrafast Optical Processing (UOP) laboratory in INRS-EMT, University of Quebec.

Many thanks also go to Prof. Tsuneyuki Ozaki for the enlightening discussion and for freely sharing thoughts and ideas with me. My special thanks to Rob Helsten, Antoine Laramée and all the technicians at the machine shop of INRS-EMT. They always helped me to fix my laboratory issues in spite of their busy schedule. I would like to thank all the past and present members of the UOP group, and especially Hu Yi, Ibraheem Al-Naib, Yoann Jestin, Oded Yaakobi, Rafik Naccache, Amir Tehranchi, Gargi Sharma, Mostafa Shalaby, Manoj Mridha, Domenico Bongiovanni, Christian Reimer, for their help, friendship and companionship along my study. Last but not least, I would like to gratefully acknowledge a fellowship, the Skim Latihan Akademik IPTA (SLAI) Fellowship, from the Ministry of Education Malaysia (MOE) for the financial support throughout my study.

ABSTRACT

Research activities at terahertz (THz) frequencies are the result of relatively recent developments. In spite of the hurdles associated to both theory and technical methods in THz generation and detection, THz technology has recently became a fertile ground for spectroscopy due to its capability in recognizing the composition of materials from the absorption spectra. By far, most of the applications exploiting THz radiation can be categorized into THz spectroscopy and imaging. The performance of THz imaging is severely restricted by the diffraction limit according to the so-called Rayleigh criterion, according to which the spatial resolution is limited by the relatively long radiation wavelength. For this reason, several near-field techniques have been developed to exceed the diffraction limit, i.e. aperture-based approaches (e.g. sub-wavelength (sub-λ) apertures [1,2] and optical gating beams [3,4]), apertureless-based approaches (e.g. metal tips [5-7]) and illumination with highly localized sources via optical rectification (OR) [8-10]. The latter technique has been the subject of an intense development within the framework of this thesis. In particular, a precise implementation of the imaging protocol is essential for properly performing time-resolved THz imaging. In the following chapters we will show that sub-λ sources interact in a non-trivial way with certain samples. The complete understanding of this interaction is fundamental in image reconstruction (even in other electromagnetic spectral regions). This interaction significantly affects the source-field reconstruction via the knife-edge (KE) measurement technique [11-13].

The research activity presented here was aimed at developing an in-depth understanding in the characterization of sub-λ THz sources, including the inherent features arising from the interaction of sub-λ source objects and the exact extraction of the sub-λ THz source profile. It will be appreciated that the resulting reconstruction accuracy fundamentally exceeds the state-of-the-art (background) associated to this investigation.

I will discuss the fundamental origin of the inherent aberrations in the KE characterization of sub-λ sources (i.e. non-separable space-time nature of the dependence between source and field), also casting the proper Green-function of the imaging system that enables an aberration-free reconstruction. In addition, extensive experimental evidence will be introduced in support of those concepts. It will be also highlighted how this specific aberration is always present in the

optical KE approach where the detection is usually performed monitoring the transmitted power only (as normally performed in the optical realm).

Building-up on the previous concepts, the investigation will extend towards other inherent limitations of the KE technique. In usual implementations, the KE is a mechanical technique based on an opaque sharp blade (usually metallic) progressively clipping portions of a propagating field. The precise characterization of a source is inherently limited by the physical distance between the blade and the source generation plane. Within the framework of this thesis, a novel all-optical KE (AOKE) technique is then demonstrated. It relies on an ultra-thin layer of photo-excited free carriers exploited as the virtual blade at the output facet of a THz generation crystal. This is a completely optical solution and eliminates the need of a mechanical shield, placing the actual blade practically "inside" the generation crystal. The time-resolved sub-λ imaging of a source rich of sub-λ features will be experimentally proved.

In the last part of this thesis the bandwidth limitation of common THz solid-state detection means will be addressed. Time resolved detection of large bandwidth THz pulses is a key technology that finds applications in a variety of different fields, such as medical imaging, security and quality control. Taking inspiration from common forms of broadband THz detection operating only in gaseous media, this thesis will introduce the first demonstration of a solid state device exploiting electric field induced second harmonic generation (EFISH) in an electrically biased thin silica (SiO_2) sample, free from the number of fundamental bandwidth limitations normally found in nonlinear detecting crystals or photo-conductive antennas.

To conclude, I believe that the main contribution of this thesis is the possibility of exploring new approaches towards the characterization and beam profiling of coherent THz radiation, with potential impact in all those fields (e.g. in microscopy) where the diffraction limit and spectral bandwidth of current THz probing technologies lead to significant practical hurdles.

RÉSUMÉ EN FRANÇAIS

1 Introduction

L'imagerie Térahertz (THz) est récemment apparue comme une puissante technique pour l'analyse et la caractérisation des matériaux dans les secteurs militaires, biomédicaux, pharmaceutiques, aérospatiaux et de la sécurité, ceci en raison de son importante capacité à extraire certaines informations comme l'épaisseur et la densité d'un matériau [1]. À ce jour, il n'existe toujours pas de définition généralement acceptée délimitant le domaine des fréquences du rayonnement THz. Cependant, une définition pratique repose sur les limites des technologies micro-ondes et infrarouges, définissant ainsi le spectre THz entre des centaines de GHz et des dizaines de THz. Néanmoins, certains auteurs définissent le rayonnement THz dans la gamme de longueurs d'onde comprises dans l'intervalle 0.1-1.0 mm [2,3], tandis que d'autres peuvent étendre la limite inférieure de cette gamme jusqu'à 30 μm [4].

En sandwich entre les ondes micro-ondes (électronique) et infrarouges (photonique), les technologies utilisant la bande de fréquence THz sont, par comparaison peu développées. En effet, le faible niveau de maturité des sources et détecteurs THz a fait en sorte que cette région du spectre électromagnétique a été relativement peu explorée, et pour cette raison dénommée le « gap THz » (Fig. 1). Néanmoins, au cours des deux dernières décennies, ce fossé technologique a été progressivement rempli, comme en témoigne la popularité croissante des conférences portant sur ce sujet ainsi que la quantité de publications dans les revues scientifiques relatives aux fréquences THz [1,4]. La plupart des applications exploitant le rayonnement THz peuvent être classées dans les domaines de la spectroscopie et de l'imagerie. Les performances de l'imagerie THz sont sévèrement limitées par la limite de diffraction selon le critère de Rayleigh, dans lequel la résolution spatiale est limitée par la longueur d'onde relativement longue du rayonnement. Pour cette raison, plusieurs techniques de champ proche ont été mises au point afin de surmonter la limite de diffraction, comme par exemple la technique de l'ouverture sous-longueur d'onde (sous-λ) [5,6], le déclenchement par faisceau optique (optical gating beam) [7,8], la pointe en métal [9,11] et l'éclairage avec une source très localisée par redressement optique ("optical rectification" ou OR) [12,14]. Cette dernière technique a fait l'objet de développements dans le cadre de cette thèse. Une mise en œuvre précise du protocole d'imagerie

est essentielle dans le domaine de l'imagerie THz résolue en temps, ce qui justifie l'intérêt pour le développement de techniques précises de profilage du faisceau pour les sources THz.

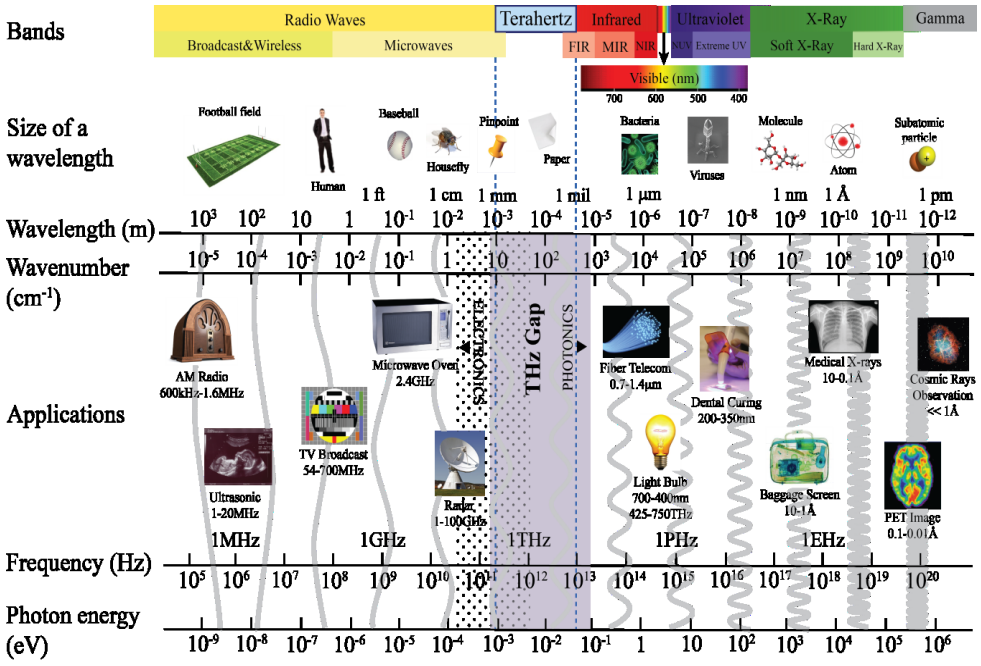

Figure 1 **La bande THz dans le spectre électromagnétique.**

2 Objectifs et organisation de la thèse

Cette thèse vise à développer les connaissances concernant la caractérisation des sources THz. Elle débute avec la compréhension de l'effet d'aberration inhérente rencontrée dans le profilage de la source sous-λ THz utilisant la technique de la lame de couteau (« knife-edge » ou KE) standard et avec la mise de l'avant d'une solution à ce problème. En outre, une technique KE tout-optique (« all-optical knife-edge » ou AOKE) est proposée pour caractériser la source sous-λ, dans le but d'éliminer l'utilisation de lames réelles. De plus, nous avons réalisé ce qui est, à notre connaissance, le premier dispositif à l'état solide pour la détection cohérente de THz. Ce dispositif utilise la génération de second harmonique induite par le champ THz (« THz field-induced second harmonic generation » ou TFISH) grâce à une micro-fente entre une paire d'électrodes immergées dans de la silice. La thèse est organisée comme suit. Dans le premier chapitre, nous énonçons les objectifs de cette thèse et présentons les notions de base pertinentes sur le sujet, c'est-à-dire : le fond de rayonnement THz, la génération et la détection de THz, le choix du milieu non-linéaire utilisé dans la génération et la détection de THz, la spectroscopie

THz résolue en temps (« THz time-domain spectroscopy » ou THz-TDS), l'imagerie THz et les approches permettant de faire l'imagerie THz sous-λ. Dans le second chapitre, nous nous sommes concentrés sur la formalisation des critères clés pour la caractérisation des sources THz sous-λ au moyen de la technique KE standard, en nous appuyant sur une étude expérimentale. Dans le troisième chapitre, en s'appuyant sur l'expérience acquise dans la caractérisation spatio-temporelle de la technique KE, nous présentons la démonstration d'une nouvelle technique KE tout-optique (AOKE). Dans le quatrième chapitre, nous introduisons le premier dispositif à l'état solide pour la détection THz cohérente au moyen de la génération de second harmonique induite par le champ électrique (« electric field-induced second harmonic generation » ou EFISH), en exploitant une structure THz sous-λ. Dans le dernier chapitre, nous présentons les conclusions et quelques remarques finales.

3 Reconstruction exacte de sources THz sous-longueur d'onde au moyen de la technique du « knife-edge »

La résolution spatiale de l'imagerie THz est fortement limitée en raison de sa grande longueur d'onde, qui se situe entre le rayonnement infrarouge et le rayonnement micro-onde. Plusieurs techniques de champ proche ont été mises en œuvre avec succès pour obtenir une résolution sous-λ en imagerie THz, dont les ouvertures sous-λ, les pointes, ou d'autres formes de discrimination spatiale impliquant un balayage de la trame sur l'échantillon à imager [9,15-19]. En outre, Yuan *et al*. ont démontré que le rapport signal-sur-bruit (« signal-to-noise ratio » ou SNR) pourrait être amélioré par la génération d'un champ THz spatialement localisé sur des dimensions sous-λ en exploitant la OR d'une pompe optique focalisée sur un cristal non linéaire [14], ce qui constitue une méthode alternative de faire de l'imagerie THz. Toutefois, le profilage des sources sous-λ est encore un sujet de recherche expérimental et théorique. Les caractéristiques spatiales d'une source THz sous-λ ne sont pas accessibles en utilisant des techniques KE en raison de la nature spatio-temporelle non séparable du champ rayonné et des modifications systématiques induites par la lame elle-même. Dans cette thèse, nous montrons que le couplage espace-temps peut être résolu et que le profil du champ de la source peut être exactement reconstruit en combinant le KE avec un échantillonnage électro-optique ("electro-optical" ou EO) résolu en temps. Une technique de caractérisation spatio-temporelle du champ a

été étudiée en s'appuyant sur la combinaison de la technique KE et de l'échantillonnage EO en exploitant les capacités uniques de résolution temporelle du champ électrique du THz-TDS. Des impulsions de 800 nm, 100 fs, 5 nJ à taux de répétition de 80 MHz, délivrées par un oscillateur Ti:saphir ultrarapide ont été étroitement focalisées sur un cristal <110> de ZnTe de 20 μm d'épaisseur, collé sur un substrat <100> de ZnTe de 500 μm d'épaisseur, afin de générer un rayonnement THz. Le KE est effectuée par l'intermédiaire d'une lame d'aluminium directement fixée à la surface du cristal de génération en translatant le cristal latéralement à l'échelle du micromètre, comme le montre la Fig. 2.

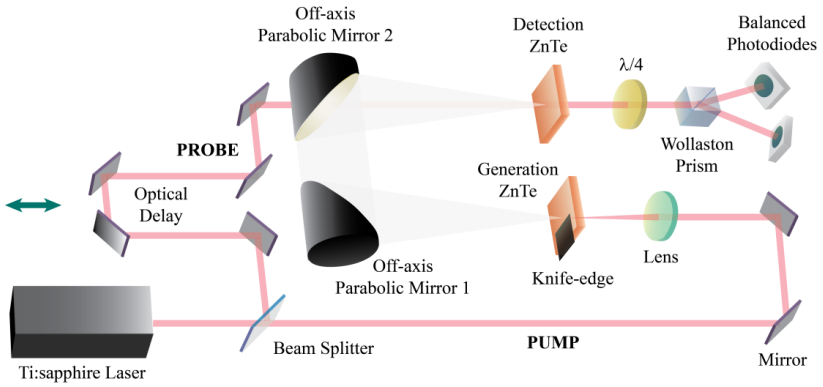

Figure 2 **Montage expérimental pour la génération et la caractérisation THz en échelle sous-λ.**

En prenant la dérivée du champ électrique résolu dans le temps suivant de la coordonné de déplacement de la lame, il est possible de récupérer le profil spatio-temporel de la source. Ceci révèle une répartition de champ asymétrique inattendue le long de la coordonnée spatiale (Fig. 3(b)).

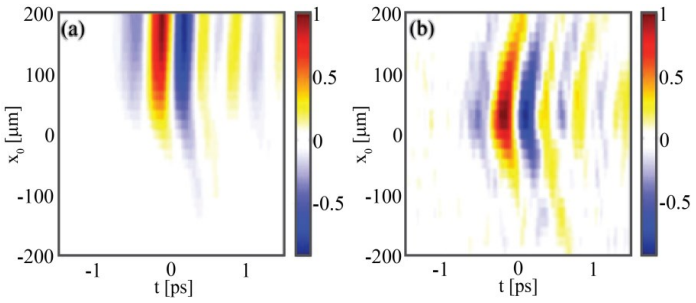

Figure 3 **(a) Champ électrique mesuré au point focal du second miroir parabolique hors axe en fonction de la coordonnée de la lame x_0 et du temps; (b) champ électrique récupéré par différenciation spatiale.**

Un modèle analytique décrivant la relation entre la lame et la source sous-λ a été développé afin de comprendre l'origine physique de cette asymétrie. Une erreur systématique affectant la résolution du champ a été mise en évidence en recourant à la formulation exacte de Sommerfeld du problème de la diffusion du rayonnement par un demi-plan conducteur infini. Une méthode simple pour récupérer la structure spatio-temporelle complète du champ échantillonné a été développée en introduisant une fonction de transfert asymétrique (Fig. 4). En exploitant la résolution temporelle du champ électrique associée à la THz-TDS, nous avons abordé théoriquement, numériquement et expérimentalement la question de l'aberration et avons fourni une méthode pour récupérer la structure spatio-temporelle complète du champ échantillonné.

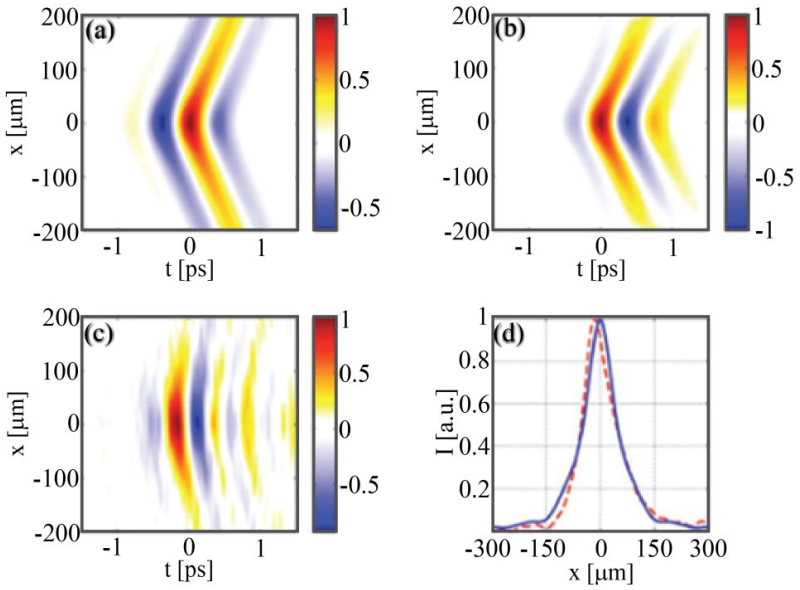

Figure 4 **Les résultats de l'inversion des données en tenant compte de la fonction de transfert : (a) champ spatio-temporel THz simulé; (b) champ récupéré obtenu par KE + TDS sous des hypothèses de symétrie géométrique; (c) champ expérimental calculé dans les mêmes conditions; (d) profils obtenus avec (solide) et sans (en pointillés) la fonction de transfert KE asymétrique.**

4 Profilage du faisceau térahertz au plan d'émission via une technique de lame de couteau tout-optique

Bien que la fonction de transfert soit conçue pour la reconstruction exacte du profil du champ THz sous-λ, la technique de KE classique reste une technique mécanique, dans laquelle les résultats de la caractérisation sont fortement dépendants de la distance (c.-à-d. des distances nettement sous-λ) de la lame physique par rapport au plan de génération. Nous avons proposé et démontré une nouvelle technique KE optique (AOKE) utilisant une couche ultra-mince de porteurs de charge libres photo-excités comme lame virtuelle dans le plan exact de la source THz pour bloquer le champ THz dans le processus de caractérisation. L'utilisation d'une lame physique fixée à une distance sous-λ du plan de génération peut ainsi être éliminée, ce qui est plus avantageux en pratique. Le montage expérimental est esquissé dans ses principaux éléments sur la Fig. 5 (a): les impulsions THz sont générées par OR d'impulsions optiques femtosecondes [20] générées par un amplificateur régénératif Ti:saphir (Spectra-Physics *Spitfire).* Cette source émet un train d'impulsions de 120 fs centrées à λ = 800 nm, à un taux de répétition de 1 kHz. Le faisceau d'entrée est divisé en trois lignes, c.-à-d. la ligne optique de la pompe (*pompe, o*), la ligne de la sonde optique et ligne de la pompe ultraviolette (« ultraviolet » ou UV, à 400 nm) (*pompe, UV*). Dans la ligne *pompe, o*, le train d'impulsions de puissance moyenne de 200 mW éclaire un cristal de ZnTe <110> de 20 μm d'épaisseur pour la génération des THz.

Un système d'imagerie composé de trois miroirs paraboliques reconstitue le plan de Fourier de la surface émettrice du cristal sur un second cristal de ZnTe, de 3 mm d'épaisseur, utilisé pour la détection EO des THz. Le champ est échantillonné au centre du plan de Fourier qui, par définition, renvoie le profil de champ moyen (pas la puissance) dans le plan de la source. Une impulsion femtoseconde UV (λ = 400 nm, énergie de photon de 3.1 eV), se propageant en direction inverse, induit une couche de photo-porteurs par absorption d'un photon unique près de la face de sortie du cristal de ZnTe émettant le rayonnement THz. Cette impulsion UV est générée par le processus de type I de doublage de fréquence de la source à 800 nm dans un cristal de BBO de 0.5 mm d'épaisseur. Un filtre passe-bande centré à 400 nm est utilisé pour isoler le faisceau de second harmonique. Un système d'imagerie constitué des lentilles L_1 et L_2 projette l'image de la lame sur un cristal de génération de THz en utilisant la lumière UV. La

position transverse de la couche conductrice induite optiquement (Fig. 5 (b)) est contrôlée par la translation de la lame. Ce mince masque conducteur a une épaisseur plus petite que la longueur d'onde THz, c'est-à-dire une centaine de nanomètres (l'échelle de la profondeur de pénétration du ZnTe à 400 nm). En outre, il est positionné à une distance sous-λ par rapport à la section de génération dans le volume du cristal. La synchronisation de la génération de porteurs libres et de l'impulsion THz générée est assurée par un retard variable dans la ligne de pompage UV. Les formes d'onde THz dans le domaine temporel sont mesurées alors que le KE se déplace le long de coordonnée x_0 en translatant la lame réelle. Les expériences ont été effectuées sous atmosphère d'azote sec afin d'éliminer l'empreinte THz typique induite par la vapeur d'eau.

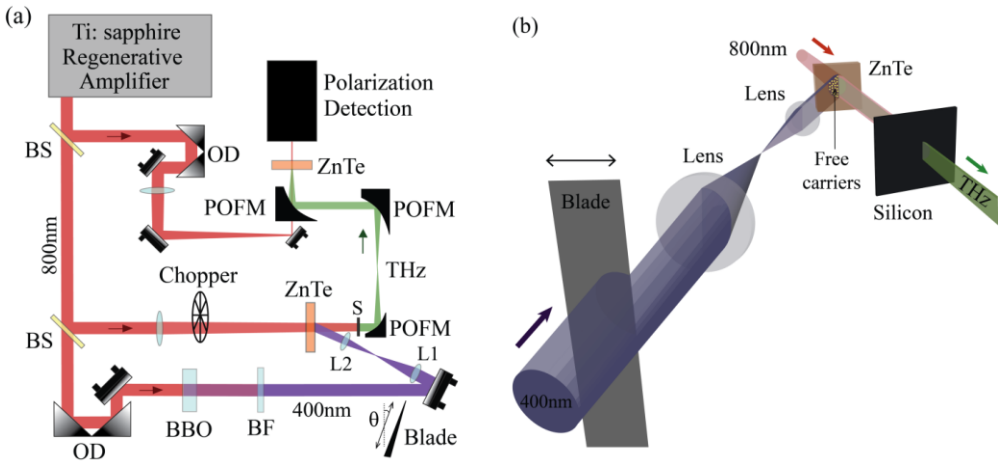

Figure 5 **(a) Montage expérimental (BS: diviseur de faisceau, OD: retard optique, BF: filtre passe-bande, POFM: miroir parabolique hors axe, L1 et L2: lentilles, S: silicium, WP: prisme de Wollaston); (b) porteurs libres induits par l'impulsions UV dans une zone en forme de lame.**

La Fig. 6 (a) illustre la dépendance de l'énergie THz absorbée en fonction du délai de la pompe UV. La mesure AOKE effectuée pour une énergie de pompe UV de 95 μJ (fluence ≈ 330 μJ/cm^2), est représentée sur la Fig. 6 (b), où la puissance THz, obtenue par l'intégrale du champ au carré en fonction du temps, est tracée en fonction de la position de la lame. Puisque la taille du faisceau THz est significativement super-λ, l'AOKE n'introduit pas de changement important dans la phase du champ [21]. Ceci est également mis en évidence sur la Fig. 6 (c) qui présente les mesures AOKE résolues autour de la fréquence 1 THz (λ = 300 μm), obtenues en prenant la racine carrée de la densité spectrale de puissance à 1 THz. (La courbe correspond étroitement à celle obtenue à partir du spectre complet de densité spectrale à tous les délais considérés.) Le

champ THz, $E_{THz}(x_0, y_0, t)$ reconstruit est illustrée dans l'encart de la Fig. 6 (d) pour un retard de la pompe $t_{pompe,uv}$ = 6 ps, selon l'hypothèse courante de la séparabilité complète en x et y du profil de champ, c.-à-d. $E_{THz}(x_0, y_0, t) = a(x_0, t)b(y_0, t)$. La forme d'onde temporelle THz mesurée par le système TDS pour chaque retard de la lame forme une carte spatio-temporelle $EM(x_0, t)$. Le champ THz, $E_{THz}(x_0, t)$ est évalué en effectuant une dérivée spatiale de la carte $EM(x_0, t)$. Le profil d'intensité THz est représenté par la ligne pointillée rouge sur la Fig. 6(d). La taille du profil d'intensité THz, c.-à-d. en unités arbitraires $I_{THz}(x) = \int_{-\infty}^{\infty} \left|E_{THz}(t)\right|^2 dt$ (défini comme la puissance à $1/e^2$ du sommet) se trouve être w_{THz} = 0.66 mm. Il est en parfait accord avec la taille estimée $w_{pompe,o}$ = 0.93 mm de la pompe gaussienne à 800 nm en supposant que la taille du faisceau THz généré soit relié à la taille de la pompe par $w_{THz} = w_{pompe,o}/\sqrt{2}$ étant donné que le champ THz est proportionnel à l'intensité optique de pompage [19,22,23].

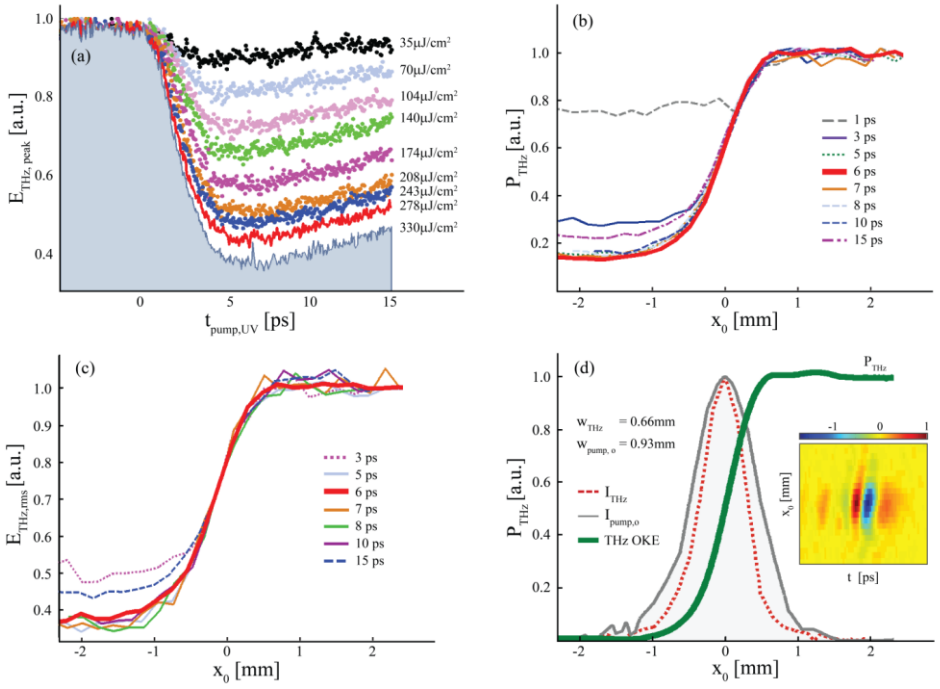

Figure 6 **(a) Pic du champ THz en fonction du retard de la pompe UV en fonction du délai de la pompe UV; (b) puissance THz mesurés par AOKE en fonction de la position de la lame; (c) champ à 1 THz mesuré par AOKE en fonction de la position de la lame; (d) puissance THz et intensité THz mesurée par AOKE à un retard de la pompe UV de 6 ps et intensité de la pompe UV en fonction de la position de la lame. L'encart montre la carte spatio-temporelle reconstruite.**

Nous avons également validé l'AOKE pour la caractérisation des sources sous-λ THz, en particulier au plan de la source THz. Un motif d'éclairage constitué de franges lumineuses étroites a été généré par un biprisme de Fresnel en BK7 (indice de réfraction 1.51), ayant un angle d'apex de 177 ° (c.-à-d. l'angle de réfraction θ_r = 1.5 °), placé dans le trajet du faisceau pompe, avant le cristal de ZnTe générateur. L'écartement des franges, d_p, du champ d'interférence est simplement déterminé par l'optique géométrique comme $d_p = \lambda / [2\,(n\text{-}1)\,\theta_r] \approx$ 30 μm, où λ = 800 nm est la longueur d'onde de la pompe, n est l'indice de réfraction du biprisme et θ_r est l'angle de réfraction. La Figure 7(a) montre le champ spatio-temporel reconstruit $E_{THz}(x_0, t)$, évalué en prenant la dérivée spatiale de la carte, $EM(x_0, t)$, obtenue des mesures expérimentale AOKE résolues en temps de la source THz sous-λ. La Figure 7(a) montre que les franges THz sont résolues à l'échelle de 10 μm, qui correspond en fait à la limite de diffraction du télescope utilisé pour projeter la lame en utilisant un faisceau pompe de 400 nm. Ce résultat est comparé avec la Fig. 7 (b) qui représente la prédiction numérique de la distribution du champ THz attendue sur la section de découpage. Dans l'expérience, des pas de translation de la lame optique de 5 μm ont été utilisés. Une faible modulation sous-λ superposée au profil super-λ (Fig. 7 (b)) est attendue. La limite de diffraction fait en sorte que cette modulation disparaît rapidement suivant la coordonnée de propagation du faisceau THz et elle peut être observée seulement en découpant le champ à une distance sous-λ du plan de génération. L'impulsion THz reconstruite sur la Fig. 7(a) montre une forte contribution des franges sous-λ, ce qui indique que les données sont recueillies à proximité du plan de production. Ceci est particulièrement évident lorsque les champ reconstruit et calculé sont représentés dans l'espace transformé $E(k, \omega)$ (respectivement Fig. 7 (c) et Fig. 7(d)). Dans figures nous représentons les locus $k = \pm \omega/c$, qui séparent les régimes super-λ ($|k| < |\omega|/c$) et sous-λ ($|k| > |\omega|/c$). Les composants sous-λ très visibles (correspondant à $k/2\pi$ = 0.025 μm^{-1} et $\omega/2\pi$ = 1 THz) contiennent l'information sur la modulation périodique caractérisant le profil spatial THz. Il est à noter qu'il existe une forte asymétrie dans le profil du champ THz reconstruit et une plus forte contribution des franges sous-λ en comparaison de ceux prédits par le modèle numérique prenant en compte la modulation THz sous-λ. Ceci est attendu pour un système KE + TDS qui implique une fonction de transfert $\bar{T}(k, \omega)$, entre les champs incident et reconstruit dans l'espace de Fourier:

$$\breve{\mathrm{E}}^{(R)}(k_x,\omega) \propto \breve{T}(k_x,\omega)\breve{\mathrm{E}}^{(i)}(k_x,\omega) \tag{2.1}$$

$$\breve{T}(k_x,\omega) \begin{cases} \sqrt{1+\dfrac{ck_x}{\omega}} & \text{for} \quad k_x > -\dfrac{\omega}{c} \\ 0 & \text{for} \quad k_x < -\dfrac{\omega}{c} \end{cases} \tag{2.2}$$

où c est la vitesse de la lumière. Cette fonction coupe les composantes superluminiques correspondant à la région délimitée par les lignes droites $k_x = -\omega/c$ et $\omega = 0$, mais amplifie fortement les détails dans la région entre $k_x = \omega/c$ et $\omega = 0$. Comme montré dans [21], le système KE + TDS est particulièrement approprié pour détecter les faibles détails sous-λ en autant que la lame est positionnée à proximité immédiate de la source sous-λ à être caractérisée. La technique AOKE proposée satisfait à cette condition et, en outre, permet de cartographier le champ sous-λ à l'intérieur du milieu d'indice de réfraction élevé où le champ THz est généré ou là où la modulation est imposée.

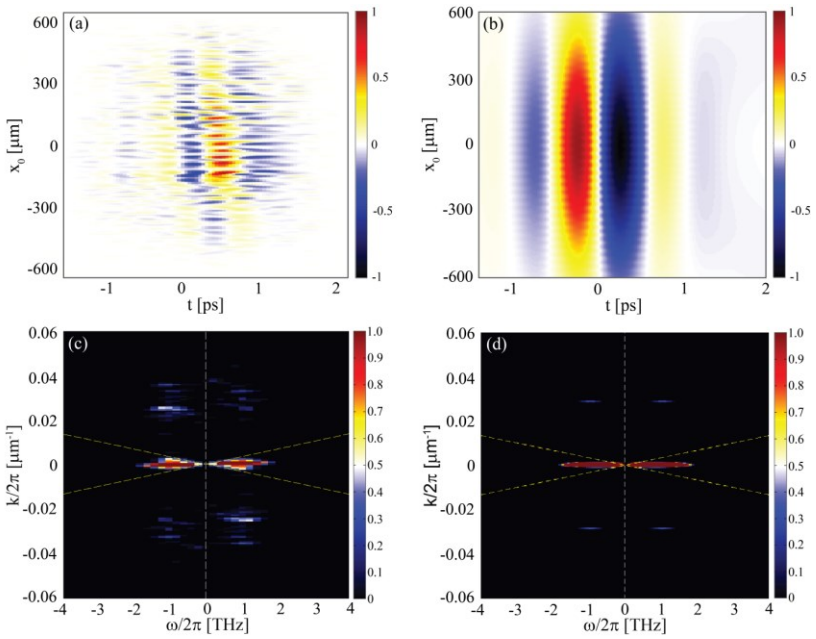

Figure 7 **Champ THz reconstruit dans l'espace-temps et l'espace transformé. (a) Profil spatio-temporel reconstruit de la source sous-λ THz produite par le biprisme et (b) la simulation numérique correspondante. (c) Spectre de Fourier expérimental obtenu à partir de (a), et (d) prédiction de la simulation numérique correspondante.**

5 Détection cohérente d'impulsions térahertz utilisant une micro fente dans un milieu solide polarisé

Les expériences discutées plus haut ont été effectuées en utilisant un cristal de ZnTe comme milieu de détection, où l'émission THz a été caractérisée par échantillonnage EO. Le champ THz induit une biréfringence instantanée dans le milieu EO, ce qui est facilement détecté au moyen d'un deuxième faisceau dans le proche infrarouge, lequel a été séparé du rayon de pompe. L'efficacité de détection et la largeur de bande des cristaux EO ne sont pas seulement limitées par l'absorption et le désaccord de phase, elles sont également perturbées par les multiples réflexions internes dans le cristal. En outre, les champs THz de plusieurs centaines de kilovolts par centimètre peuvent induire des retards de phase plus grands que π dans le faisceau sonde passant à travers le cristal d'épaisseur millimétrique. Dans ce cas, un cristal de détection mince est souhaitable parce que ces grands retards de phase produisent une forte rotation de la polarisation du faisceau sonde, ce qui écarte l'échantillonnage EO de la réponse linéaire et produit une distorsion de la forme d'onde détectée. La détection cohérente par polarisation électrique dans l'air (« air-biased-coherent-detection » ou ABCD), grâce à la faible dispersion de l'air, permet de mesurer des champs THz à très large bande passante (> 20 THz), mais ne peut pas être facilement miniaturisé à l'échelle de quelques centimètres. En outre, elle nécessite généralement des sources de tension dans le domaine des kV, car le SNR du signal détecté dépend de l'amplitude du champ de polarisation E_{bias} [24]

$$SNR = \frac{2I_{\omega}E_{THz}E_{bias}}{\delta I_{\omega}[(E_{THz})^2+(E_{bias})^2+2E_{THz}E_{bias}]}\ , \tag{3.1}$$

et il est limité par la tension de claquage de l'air. Dans le cadre de ce travail de thèse nous avons démontré la caractérisation cohérente des ondes THz basé sur TFISH dans un dispositif à l'état solide, composé d'une mince couche de silice polarisée au moyen d'une paire d'électrodes d'or ayant un écart de l'ordre du micron. Pour un tel dispositif, les dimensions de la région d'interaction peuvent être réduits au millimètre ou moins, et la puissance sonde nécessaire pour la détection est comparable à celle employée pour l'échantillonnage EO. Nous avons effectué la détection résolue en temps d'impulsions THz d'un seul cycle en exploitant la technique EFISH dans un échantillon de silice (SiO_2) mince polarisé électriquement. Un champ électrique THz

cohérent a pu effectivement être enregistré au moyen du TFISH lorsqu'un potentiel de quelques milliers de volts est appliqué entre deux électrodes d'or (Au) imbriquée dans du SiO_2.

Les mesures ont été prises à l'aide du montage THz-TDS illustré sur la Fig. 8 (a). L'impulsion d'entrée est fournie par un amplificateur régénératif Ti:saphir de longueur d'onde centrale de 800 nm, avec 120 fs de durée d'impulsion, et une fréquence de répétition de 1 kHz. Cette impulsion d'entrée polarisée linéairement (selon *x*, dans notre cas) est divisée en pompe et sonde respectivement pour la génération et la détection THz. Le rayonnement THz est généré par OR à partir d'un cristal de ZnTe et ensuite focalisé sur la fente métallique de détection après une propagation à travers plusieurs miroirs paraboliques hors axe. Nous avons pu enregistrer le signal THz avec la technique proposée en échangeant la détection par le cristal de ZnTe pour notre dispositif de micro-fente et les photodiodes pour un tube photomultiplicateur (« photomultiplier tube » ou PMT). Le faisceau sonde de ~3 μJ a été focalisé à l'aide d'une lentille de 100 mm à travers un trou sur le dernier miroir parabolique dans la trajectoire du faisceau THz, de sorte que le faisceau THz et le faisceau sonde se chevauchent à l'endroit même où le champ THz induit une impulsion de second harmonique (« second harmonic » ou SH) via le processus de mélange à quatre ondes dans la fente de SiO_2.

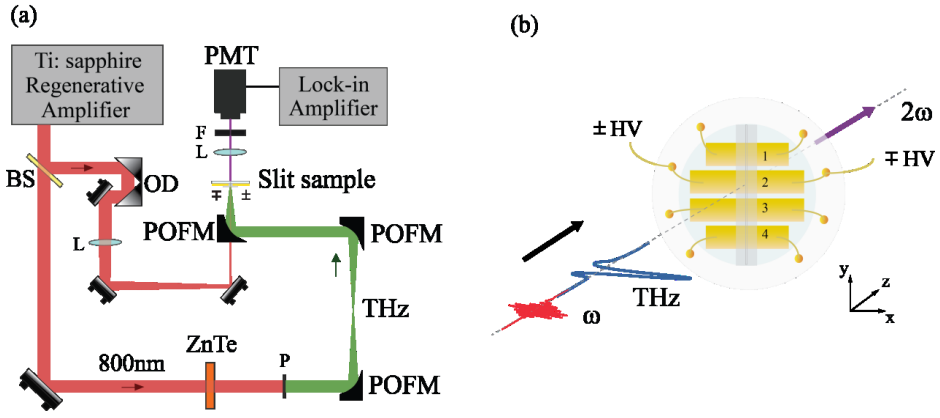

Figure 8 **(a) Montage expérimental (BS: diviseur de rayon, OD: retard optique, L: lentille, POFM: miroir parabolique hors-axe, ZnTe: zinc tellurure, P: polyéthylène, F: filtre, PMT: tube photomultiplicateur). (b) L'impulsion sonde optique polarisée suivant x et l'impulsion THz se propagent à travers la fente métallique le long de l'axe *z* (FS: silice fusionné, HV: haute tension).**

La fente est située au point focal et une polarisation de ±2.5 kV est appliquée, fournie par un modulateur de haute tension, délivrant une onde carrée bipolaire synchronisée avec les impulsions laser. Le signal de SH est filtré par un filtre passe-bande centré à 400 nm et détecté par un PMT. Le signal recueilli par le PMT est mesuré par un amplificateur à verrouillage synchronisé avec la modulation de fréquence de la polarisation de 500 Hz. Les polarisations des champs sont parallèles les unes aux autres et orientées suivant le long côté de la fente, comme le montre la Fig. 8 (b) (polarisation TM de la fente). En faisant varier le retard entre l'onde THz et le faisceau sonde, le signal de SH du faisceau sonde est observé lorsque le faisceau sonde et l'onde THz se chevauchent dans le temps. L'intensité du signal SH est mesurée en fonction du retard temporel entre l'onde THz et le faisceau sonde.

La Figure 9 (a) montre la forme d'onde THz détectée d'une manière cohérente. Notons que, si le champ de polarisation AC n'est pas appliqué, il est quand même possible de mesurer un signal d'interaction incohérente. Pour la détection cohérente, l'amplificateur de verrouillage est déclenché à la fréquence de répétition du laser et le signal enregistré est représentée à la Fig. 9 (b). Ce signal est proportionnel à l'intensité du champ THz plutôt qu'au carré du champ électrique. Ceci est une conséquence du désaccord de phase entre deux processus de mélange à quatre ondes qui sont responsables de l'interaction de TFISH (voir p. ex. [25]).

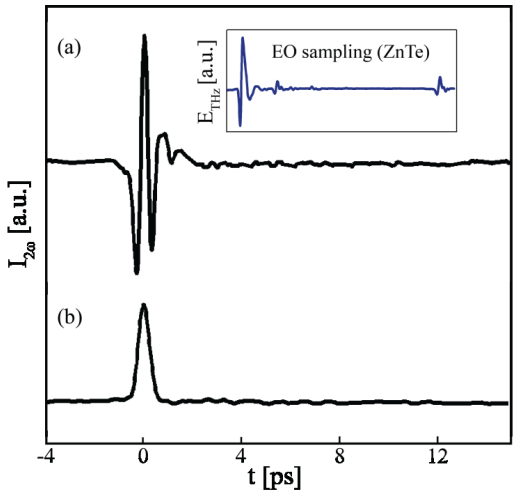

Figure 9 **Comparaison de formes d'ondes THz dans le domaine temporel mesurées (a) avec et (b) sans champ polarisé alternatif. L'encart supérieur montre les réflexions internes du cristal, accompagnées par les réflexions entre les cristaux de génération et de détection lors de mesures d'échantillonnage EO.**

Les formes d'onde mesurées à différentes valeurs de la polarisation AC sont illustrées à la Fig. 10 (a). L'augmentation du signal avec le potentiel de polarisation indique que le signal de TFISH est amplifié par le terme croisé à mesure que le potentiel de polarisation AC augmente. Cependant une dégradation du signal de SH est observée lorsque la polarisation AC est supérieure à ±2.5 kV, ce qui réduit la gamme dynamique (ligne rouge sur la Fig. 10 (b)) et le SNR (ligne bleue dans la Fig. 10 (b)). Typiquement, le bruit dans le signal détecté est déterminé par le bruit de grenaille, qui est proportionnel à la puissance optique moyenne, le bruit de fond de du PMT et le bruit de l'électronique. L'origine et le mécanisme du phénomène particulier de la dégradation de la gamme dynamique aux plus fortes valeurs du potentiel de polarisation est encore sous étude. La Figure 10 (c) montre les spectres d'amplitude de l'impulsion THz détectés pour différents potentiels de polarisation AC.

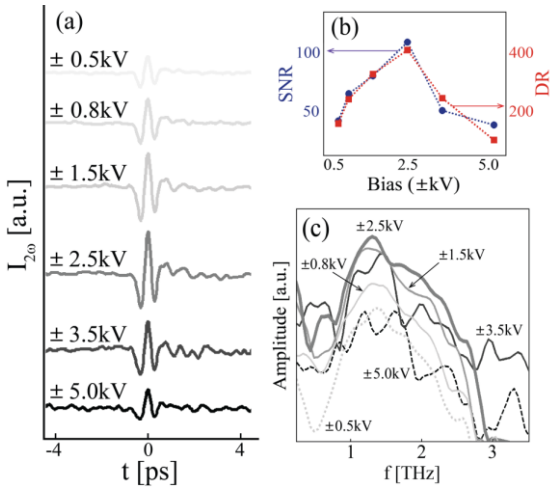

Figure 10 **(a) La dépendance de l'intensité de SH mesurée en fonction du potentiel de polarisation AC avec une énergie fixe de la sonde de ~3 μJ, mesurée dans de l'azote gazeux sec. (b) Gamme dynamique correspondante (ligne rouge) et rapport signal-sur-bruit (ligne bleue). (c) Spectres d'amplitude obtenus des formes d'onde dans le domaine temporel.**

Nous avons donc caractérisé avec succès l'impulsion THz au moyen du SH en utilisant une couche ultra-mince de SiO_2 ayant une épaisseur à l'échelle sous-λ déposée dans une fente. Non seulement la technique démontrée évite le problème du désaccord de phase en cristal épais et la forte réflexion de Fabry-Pérot en cristal EO mince, mais élimine également les réflexions optiques externes se produisant dans le trajet de la propagation entre les cristaux de génération et de détection. Une énergie inférieure de la sonde, par rapport à celle requise dans la technique

ABCD, peut être utilisée pour la détection, tandis que le reste du faisceau d'entrée, divisé en pompe-sonde, peut être utilisé pour optimiser la génération des THz. D'ailleurs, la faible énergie requise permet également d'effectuer facilement les mesures en utilisant un oscillateur de haute énergie, qui est devenu l'un des systèmes laser les plus largement utilisés dans les domaines de recherche connexes actuellement.

6 Conclusions

Le but de ce travail a été de mettre en œuvre de nouvelles approches pour la caractérisation précise de l'émission THz, ce qui est essentiel pour améliorer et manipuler des sources THz dans les applications pratiques. La technique KE est une technique de caractérisation bien établie qui est largement utilisée dans le profilage des faisceaux laser. Nous avons déterminé les critères importants à considérer lorsque le champ THz est caractérisé par la technique KE standard. Pour valider la technique KE standard pour son application à la caractérisation des sources THz sous-λ, nous avons d'abord étudié l'origine des aberrations inhérentes, induites par la combinaison de la technique KE et l'échantillonnage EO dans un montage TDS. L'aberration est observée en résolvant le profil spatio-temporel du champ électrique, où une distribution de champ asymétrique inattendue a été obtenue suivant la coordonnée spatiale. Nous avons abordé cette question en tenant compte de la transmission du champ électromagnétique au-delà d'un demi-plan parfaitement conducteur au moyen de l'approche exacte de Sommerfeld. Par ailleurs, nous avons également montré que la technique KE standard introduit une aberration dans le profil spatio-temporel qui pourrait limiter la fiabilité de certains protocoles d'imagerie sous-λ basés sur le balayage de trame. Il est important de noter que l'aberration dépend de la distance entre l'objet à imager et le plan de génération THz. Nous avons dérivé la forme explicite de la fonction de transfert de la mesure KE qui permet de récupérer le profil de la source d'origine à partir des données mesurées.

En dépit du développement de la fonction de transfert pour la récupération exacte du profil, comme mentionné ci-dessus, la technique KE reste une technique mécanique qui requiert une lame physique placée sur le plan d'émission de la source. C'est pourquoi nous avons développé une nouvelle technique KE tout optique (AOKE) pour caractériser la source THz, qui élimine

l'utilisation d'une lame physique disposée à une distance nettement sous-λ du plan de génération THz. La technique AOKE proposée repose sur la création d'une couche très mince de porteurs libres photo-excités agissant comme une lame virtuelle située exactement sur le plan de génération THz pour bloquer l'émission THz. Un rayonnement UV est utilisé pour projeter une image nette de la lame sur la facette de sortie de cristal de génération, la zone photo-excitée empêchant la transmission des THz. Ainsi, la mesure AOKE peut être vue comme une « mesure KE avec lame distante », utilisant en fait une lame virtuelle. Cette technique a d'abord été testée sur une source THz super-λ, et ensuite appliquée à la caractérisation d'une source THz avec un motif de grille sous-λ pour valider son utilité sur des sources avec différentes tailles et formes. Nous nous attendions à une dépendance quadratique entre le profil d'intensité des franges et le profil d'intensité THz, et donc à très fort contraste de chaque frange dans la mesure AOKE. Le profil spatio-temporel correspondant a montré que le motif grillagé de la source THz est résolu avec une résolution de 10 μm, ce qui correspond à la limite de diffraction du système d'imagerie utilisé pour projeter l'image en forme de lame par rayonnement UV.

Les caractérisations discutées plus haut ont été effectuées en utilisant un cristal EO, c.-à-d. un cristal de ZnTe pour la détection. Cependant, la détection THz à travers un cristal EO est généralement limitée par l'absorption et le désaccord de phase. De plus, il souffre également de réflexions multiples à l'intérieur du cristal. Par ailleurs, le fait qu'un champ THz fort donne lieu à des retards de phase supérieurs à π dans le faisceau sonde optique quand il se propage à travers le cristal EO soulève de l'intérêt pour développer un dispositif différent permettant de surmonter ces limitations. C'est ainsi que, dans la dernière phase de mon étude, nous avons proposé et démontré le schéma ABCD à l'état solide, avec une large bande passante, pour détecter les impulsions THz. Nous avons procédé à une nouvelle mise en œuvre du protocole ABCD se fondant sur la TFISH dans un dispositif composé de SiO_2 de quelques microns d'épaisseur soumis à un champ de polarisation externe. Dans l'expérience, la grande tension de claquage et la forte non-linéarité du verre ont été exploitées pour obtenir une détection à SNR élevé en utilisant une sonde optique de faible énergie. Au meilleur de notre connaissance, il s'agit du premier dispositif à l'état solide pour la détection THz cohérente s'appuyant sur le TFISH. Les résultats préliminaires présentés dans cette thèse ont été obtenus en mesurant des impulsions THz au moyen d'une fente de 30 μm comportant deux électrodes d'or imbriquées dans du SiO_2. Le

faisceau THz a été focalisé sur la même zone de détection dans l'espace et dans le temps que l'impulsion sonde. Les résultats ont été comparés aux mesures des impulsions THz par échantillonnage EO. Un rapport du SNR de près de 100 a été obtenu en présence d'une polarisation externe de 2.5 kV. Un signal d'interaction incohérent peut être détecté en l'absence de polarisation externe. Ce signal est proportionnel à l'intensité THz plutôt qu'au champ THz au carré, qui est attribuée à la non-concordance des deux processus de mélange à quatre ondes qui décrivent l'interaction TFISH.

Pour résumer, le travail présenté dans cette thèse fournit des perspectives captivantes en ce qui concerne la compréhension et les approches pour caractériser l'émission THz, et ouvre les portes pour un plus grand choix de matériaux et de méthodes pour mesurer les impulsions THz.

7 References

[1] D. M. Mittleman, "Frontiers in terahertz sources and plasmonics," *Nature Photon* **7**, 9, 666- 669 (2013).

[2] E. Brüdermann, H.-W. Hübers and M. F. Kimmitt, *Terahertz Techniques.* Springer-Verlag Berlin Heidelberg (2012).

[3] K. E. Peiponen, A. Zeitler & K.-G. Makoto, *Terahertz Spectroscopy and Imaging.* Springer-Verlag Berlin Heidelberg, USA (2013).

[4] X.-C. Zhang and J. Xu, *Introduction to THz Wave Photonics.* Springer Science+Business Media, New York (2010).

[5] O. Mitrofanov, I. Brener, R. Harel, J. D. Wynn, L. N. Pfeiffer, K. W. West and J. Federici, "Terahertz near-field microscopy based on a collection mode detector," *Appl. Phys. Lett.* **77**, 22, 3496-3498 (2000).

[6] O. Mitrofanov, I. Brener, M. C. Wanke, R. R. Ruel, J. D. Wynn, A. J. Bruce and J. Federici, "Near-field microscope probe for far infrared time domain measurements," *Appl. Phys. Lett.* **77,** 4, 591-593 (2000).

[7] D. V. Palanker, G. M. H. Knippels, T. I. Smith and H. A. Schwettman, "Fast IR imaging with sub-wavelength resolution using a transient near-field probe," *Nucl. Instrum. Meth. Phys. Res. Sect. B* **144**, 1-4, 240-245 (1998).

[8] D. V. Palanker, G. M. H. Knippels, T. I. Smith and H. A. Schwettman, "IR microscopy with a transient photo-induced near-field probe (tipless near-field microscopy)," *Opt. Commun.* **148**, 4-6, 215-220 (1998).

[9] S. Hunsche, M. Koch, I. Brener and M. C. Nuss, "THz near-field imaging," *Opt. Commun.* **150**, 1-6, 22-26 (1998).

[10] B. Knoll and F. Keilmann, "Near-field probing of vibrational absorption for chemical microscopy," *Nature* **399**, 134-137 (1999).

[11] H.-T. Chen, R. Kersting and G. C. Cho, "Terahertz imaging with nanometer resolution," *Appl. Phys. Lett.* **83**, 15, 3009-3011 (2003).

[12] J. Z. Xu and X.-C. Zhang, "Optical rectification in an area with a diameter comparable to or smaller than the center wavelength of terahertz radiation," *Opt. Lett.* **27,** 12, 1067-1069 (2002).

[13] T. Yuan, S. P. Mickan, J. Z. Xu, D. Abbott and X.-C. Zhang, "Towards an apertureless electro-optic T-ray microscope," CFD3, *The Conference of Laser and Ellectro-Optics (CLEO).* Long Bech, CA (2002)

[14] T. Yuan, J. Z. Xu and X.-C. Zhang, "Development of terahertz wave microscopes," *Infrared Phys. Technol.* **45,** 5-6, 417-425 (2004).

[15] O. Mitrofanov, M. Lee, J. W. P. Hsu, L. N. Pfeiffer, K. W. West, J. D. Wynn and J. F. Federici, "Terahertz pulse propagation through small apertures," *Appl. Phys. Lett.* **79**, 7, 907 (2001).

[16] M. A. Seo, A. J. L. Adam, J. H. Kang, J. W. Lee, K. J. Ahn, Q. H. Park, P. C. M. Planken and D. S. Kim, "Near field imaging of terahertz focusing onto rectangular apertures," *Opt. Express* **16**, 25, 20484-20489 (2008).

[17] F. Federici, O. Mitrofanov, M. Lee, J. W. P. Hsu, I. Brener, R. Harel, J. D. Wynn, L. N. Pfeiffer and K. W. West, "Terahertz near-field imaging," *Phys. Med. Biol.* **47**, 21, 3727-3734 (2002).

[18] Q. Chen, Z. Jiang, G. X. Xu and X.-C. Zhang, "Near-field terahertz imaging with a dynamic aperture," *Opt. Lett.* **25**, 15, 1122-1124 (2000).

[19] H. Bethe, "Theory of diffraction by small holes," *Phys. Rev.* **66**, 7-8, 163-182 (1944).

[20] A. Rice, Y. Jin, X. F. Ma, X.-C. Zhang, D. Bliss, J. Larkin and M. Alexander, "Terahertz optical rectification from <110> zinc-blende crystals," *Appl. Phys. Lett.* **64**, 11, 1324-1326 (1994).

[21] M. Peccianti, M. Clerici, A. Pasquazi, L. Caspani, S. P. Ho, F. Buccheri, J. Ali, A. Busacca, T. Ozaki and R. Morandotti, "Exact reconstruction of THz sub-λ source features in knifeedge measurements," *IEEE J. Sel. Topics Quantum Electron.* **19**, 1, 8401211 (2013).

[22] M. A. C. De Araújo, R. Silva, E. De Lima, D. P. Pereira, and P. C. De Oliveira, "Measurement of Gaussian laser beam radius using the knife-edge technique: improvement on data analysis," *Appl. Opt.* **48,** 2, 393-396 (2009).

[23] A. Tomasino, A. Parisi, S. Stivala, P. Livreri, A. C. Cino, A. C. Busacca, M. Peccianti and R. Morandotti, "Wideband THz time domain spectroscopy based on optical rectification and electro-optic sampling," *Sci. Rep.* **3**, 3116, 1-8 (2013).

[24] X. Lu and X.-C. Zhang, "Balanced terahertz wave air-biased-coherent detection," *Appl. Phys. Lett.* **98**, 15, 151111 (2011).

[25] M. Clerici, D. Faccio, L. Caspani, M. Peccianti, O. Yaakobi, B. E. Schmidt, M. Shalaby, F. Vidal, F. Legare, T. Ozaki and R. Morandotti, "Spectrally resolved wave-mixing between near- and far-infrared pulses in gas," *New J. Phys.* **15**, 125011 (2013).

TABLE OF CONTENTS

LIST OF FIGURES

LIST OF EQUATIONS

$$E(t) = E_0(t)e^{-i\omega t} \tag{1.1}$$

$$\vec{P}(t) = \chi^{(1)}\vec{E}(t) + \chi^{(2)}\vec{E}^2(t) + \chi^{(3)}\vec{E}^3(t) + \cdots \equiv \vec{P}^{(1)}(t) + \vec{P}^{(2)}(t) + \vec{P}^{(3)}(t) + \cdots \tag{1.2}$$

$$\vec{E}_{THz}(t) \propto \frac{\partial^2}{\partial t^2}\vec{P}_{OR}^{(2)}(t) \tag{1.3}$$

$$\tilde{E}(\omega) \equiv A(\omega)e^{-i\phi(\omega)} = \int dt\, E(t)e^{-i\omega t} \tag{1.4}$$

$$\Delta = \frac{\lambda}{2n\sin\theta} \tag{1.5}$$

$$\Delta = \frac{1.22\lambda}{2n\sin\theta} \tag{1.6}$$

$$\Delta = 1.22\lambda\frac{f}{D} \tag{1.7}$$

$$\breve{G} \propto \frac{1}{\sqrt{(\omega/c)^2 - k_x^2}} \tag{2.1}$$

$$U(x_0, t) = \int_{-\infty}^{x_0} I(x, t)dx \tag{2.2}$$

$$e(x_0, t) \propto \int_{-\infty}^{x_0} e^{(i)}(x, t)dx \tag{2.3}$$

$$e(x = 0, z \to \infty, t) \propto \int_{-\infty}^{\infty} \mathbf{e}(x, z = 0, t)dx \tag{2.4}$$

$$e(x, y, z_{out}) = \iint_{-\infty}^{\infty} e(\xi, \eta, z = 0)h(x - \xi, y - \eta)d\xi d\eta \tag{2.5}$$

$$e(x = 0, y = 0, z_{out}) = \iint_{-\infty}^{\infty} e(\xi, \eta, z = 0)h(-\xi, -\eta)d\xi d\eta$$

$$\approx \iint_{-\infty}^{\infty} e(\xi, \eta, z = 0)d\xi d\eta \tag{2.6}$$

$$\mathbf{e}(\mathbf{r}, t) = 2\mathrm{Re}\int_{-\infty}^{\infty} \mathbf{E}(\mathbf{r}, \omega)e^{-i\omega t}\frac{d\omega}{2\pi} \tag{2.7}$$

$$\breve{\mathbf{E}}(k_x, k_y, z) = \iint_{-\infty}^{\infty} \mathbf{E}(x, y, z)e^{-ik_x x - ik_y y}dxdy \tag{2.8}$$

$$\mathbf{e}(x,y,z,t) = 2Re\iiint_{-\infty}^{\infty} \breve{\mathbf{E}}\left(k_x,k_y,z,\omega\right)e^{-ik_x x+ik_y y-i\omega t} \times \frac{dk_x dk_y d\omega}{(2\pi)^3} \tag{2.9}$$

$$\breve{\mathbf{E}}(k_x=0,k_y=0,z=0^+,\omega)\cdot\hat{\boldsymbol{u}} \tag{2.10}$$

$$\breve{\mathrm{E}}(k_x=0,\omega) = \breve{\mathrm{E}}^{(i)}(k_x=0,\omega) - \int_{-\infty}^{\infty}\frac{2i}{s_x}\sqrt{1+\frac{cs_x}{\omega}}\,\breve{\mathrm{E}}^{(i)}(s_x,\omega)\,e^{is_x x_0}\frac{ds_x}{2\pi} \tag{2.11}$$

$$\mathrm{e}_R(x_0,t) \propto \mathrm{Re}\iint_{-\infty}^{\infty}\sqrt{1+\frac{cs_x}{\omega}}\,\breve{\mathrm{E}}^{(i)}(s_x,\omega)e^{is_x x_0-i\omega t}\frac{ds_x d\omega}{(2\pi)^2} \tag{2.12}$$

$$\mathrm{e}_R(x_0,t) \propto \iint_{-\infty}^{\infty} H\left(1+\frac{ck_x}{\omega}\right)\sqrt{1+\frac{ck_x}{\omega}}\,\breve{\mathrm{E}}^{(i)}\times(k_x,\omega)e^{ik_x x_0-i\omega t}\frac{dk_x d\omega}{(2\pi)^2} \tag{2.13}$$

$$\breve{\mathrm{E}}^{(R)}(k_x,\omega) \propto H\left(1+\frac{ck_x}{\omega}\right)\sqrt{1+\frac{ck_x}{\omega}}\,\breve{\mathrm{E}}^{(i)}(k_x,\omega) \tag{2.14}$$

$$\breve{T}(k_x,\omega) \equiv \begin{cases}\sqrt{1+\frac{ck_x}{\omega}} & \text{for } k_x > -\frac{\omega}{c}\\ 0 & \text{for } k_x < -\frac{\omega}{c}\end{cases} \tag{2.15}$$

$$\breve{T}_-(k_x,\omega) \equiv \begin{cases}-\sqrt{1-\frac{ck_x}{\omega}} & \text{for } k_x > \frac{\omega}{c}\\ 0 & \text{for } k_x < \frac{\omega}{c}\end{cases} \tag{2.16}$$

$$\breve{\mathrm{E}}_{\pm}^{(i)}(k_x,\omega) \propto \pm H\left(1\pm\frac{ck_x}{\omega}\right)\sqrt{\frac{\omega}{\omega\pm ck_x}}\,\breve{\mathrm{E}}_{\pm}^{(R)}(k_x,\omega) \tag{2.17}$$

$$E = \frac{hc}{\lambda} \tag{3.1}$$

$$\delta_p = \frac{1}{\sqrt{2\omega\mu_0\sigma}} = \frac{1}{\alpha} \tag{3.2}$$

$$\alpha = \frac{1}{d}\ln\frac{A_R}{A_S} \tag{3.3}$$

$$\theta_\mathrm{d} = (n-1)\theta_\mathrm{r} \tag{3.4}$$

$$D = a(\cot\theta_\mathrm{d} - \tan\theta_\mathrm{r}) \tag{3.5}$$

$$I(x,y,z_1) = 2\{1+\cos[2k(n-1)\theta_\mathrm{r}x]\} \tag{3.6}$$

$$d_p = \frac{\lambda}{2\theta_\mathrm{d}} = \frac{\lambda}{2(n-1)\theta_\mathrm{r}} \tag{3.7}$$

$$\check{E}^{(R)}(k_x,\omega) \propto \check{T}(k_x,\omega)\check{E}^{(i)}(k_x,\omega) \tag{3.8}$$

$$\check{T}(k_x,\omega) \equiv \begin{cases} \sqrt{1+\frac{ck_x}{\omega}} & \text{for } k_x > -\frac{\omega}{c} \\ 0 & \text{for } k_x < -\frac{\omega}{c} \end{cases} \tag{3.9}$$

$$SNR \propto 1 - \frac{1}{(E_{THz}+E_{bias})} \tag{4.1}$$

$$E_{2\omega} \propto \chi^{(3)} E_\omega E_\omega E_{THz} \propto \chi^{(3)} I_\omega E_{THz} \tag{4.2}$$

$$I_{2\omega}^{measured} = |E_{2\omega}|^2 = |E_{2\omega}^{THz} + E_{2\omega}^{local}|^2 = |E_{2\omega}^{THz}|^2 + |E_{2\omega}^{local}|^2 + 2E_{2\omega}^{THz}E_{2\omega}^{local}\cos(\phi) \tag{4.3}$$

$$E_{2\omega}^{THz} \propto \chi^{(3)} I_\omega E_{THz} \quad , \quad E_{2\omega}^{local} \propto \chi^{(3)} I_\omega E_{bias} \tag{4.4}$$

$$I_{2\omega}^{measured} \propto (\chi^{(3)} I_\omega)^2 [E_{THz}^2 + E_{bias}^2 \pm 2E_{THz}E_{bias}] \tag{4.5}$$

LIST OF ABBREVIATIONS

Au	Gold
ABCD	Air-biased-coherent detection
BBO	Beta Barium Borate
BF	Bandpass filter
BS	Beam splitter
Cr	Chromium
CW	Continuous wave
DR	Dynamic range
DC-EFISH	DC electric field-induced second harmonic generation
DFG	Difference frequency generation
EFISH	Electric field-induced second harmonic generation
EO	Electro-optic
FDTD	Finite-difference time-domain
FS	Fused silica
GaAs	Gallium arsenide
GaP	Gallium phosphite
HV	High voltage
KE	Knife-edge
KE+TDS	Combination of knife-edge and time-domain spectroscopy

L	Lens
$LiNbO_3$	Lithium niobate
NA	Numerical aperture
N_2O	Dinitrogen monoxide
OD	Optical delay
AOKE	All-optical knife-edge
OR	Optical rectification
PC	Photoconductor
PCA	Photoconductive antenna
PECVD	Plasma-enhanced chemical vapor deposition
PMT	Photomultiplier tube
POFM	Parabolic off-axis mirror
pump,o	Optical pump
pump,UV	Ultraviolet pump
QC	Quantum cascade
S	Silicon
SH	Second harmonic
SHG	Second harmonic generation
SiH4	Silane
SiO_2	Silica
SNR	Signal-to-noise ratio

Sub-λ	Sub-wavelength
Super-λ	Super-wavelength
T	Transfer function
TDS	Time-domain spectroscopy
TFISH	Terahertz field-induced second harmonic generation
THz	Terahertz
THz-TDS	Terahertz time-domain spectroscopy
Ti	Titanium
UV	Ultraviolet
WP	Wollaston prism
ZnTe	Zinc telluride
λ/4	Quarter waveplate

1 INTRODUCTION

1.1 Background

Historically, THz radiation has been investigated for a while. Before the early 80s, it was classically referred as the field of far-infrared waves or millimeter/submillimeter waves. It occupies a relatively large portion (especially as meant in the past two decades) of the electromagnetic spectrum between the infrared and microwave bands. To date, there is still no commonly agreed definition of the upper and lower frequency limits of THz radiation. Probably, a quite effective definition relies on the limits of common microwave and infrared technologies, placing the THz spectrum between hundreds of GHz to tens of THz. Nevertheless, it is quite usual to come across differently defined ranges while reading through scientific articles and books. Some authors refer THz radiation to the range of 0.1–1.0 mm in wavelength [14,15] while others extend this range to wavelengths as short as 30 μm [16]. THz radiation is invisible to us, although it naturally fills up the space of our daily life, as it is emitted, for instances, from such natural sources ranging from cosmic background radiation to blackbody radiation. Most of the radiation emitted in the universe is in this range but the Earth's atmosphere is opaque to most of the far-infrared band, mainly due to the presence of water vapour [15]. Hence, historically, THz technologies were initially developed mainly within the astronomy community, e.g. high-altitude telescopes were used for ground-based observations in sub-millimeter wavelengths of the cosmic far-infrared radiation. Nevertheless, this part of the electromagnetic spectrum remains the least explored region of the spectrum – mainly due to the technical difficulties involved in making efficient and compact THz sources and detectors.

Research on electromagnetic waves has been traditionally divided into two different fields, the first covering the typical bands of electronics - classically referred as electromagnetism, and the second based on the manipulation of light (classically referred as optics) exploiting the so-called field-matter interaction in photonic structures and (in modern times) becoming increasingly related to the concept of photon (in a broader sense we also include here X-ray technologies). Sandwiched between the microwave (electronics) and infrared (photonics) part of the electromagnetic spectrum, the THz band is by comparison underdeveloped, as THz waves

simply do not fit into either category based on a technological point of view. The field of microwaves and optics differ significantly on the theoretical framework and technical approaches for the generation and detection of radiation. The most important challenge within the microwave realm is the fabrication of electronic devices capable of operations at frequencies substantially above a few hundred of GHz [17]. The access to the THz band has been then achieved by way of bulky devices that nonlinearly multiplied the frequency emitted by those devices [18,19]. The characteristic electronic cut-off at high frequency results from the significant carrier transit times in the active regions of semiconductor devices, a fact that also inherently implies that fast devices must have exceptionally small active areas, hence very limited power throughputs.

On the optical side of the spectrum, interband semiconductor diode lasers have been designed for operation at visible and near-infrared frequencies. It is noteworthy that the concept of light generation by the radiative recombination of conduction band electrons cannot be simply extended into the mid infrared since suitable semiconductors are not available [20]. Recent research shows several attempts in applying the concept of quantum cascade (QC) lasers in which inter-sub-band or inter-miniband transitions in layered semiconductor heterostructures may be used to generate light in the mid- and far-infrared range [21]. In addition, in the following chapter, the demonstration of THz sources based on bulky nonlinear devices will be extensively tackled. Although this very popular approach has been driving the THz research field for the past 20 years, it is also only marginally suitable for broad diffusion and marketing of THz technologies.

The low maturity level of THz sources and detectors stemming from the difficulties mentioned above has led to the fact that this relatively unexplored region of the electromagnetic spectrum has been termed the “THz gap” (Fig. 1.1), which makes THz science and applications still a scientific frontier.

The above-mentioned technology gap has been gradually filled in a number of creative ways, mainly in the last two decades. The ongoing efforts are mostly motivated by the unique advantages provided by THz radiation. The spectral region of THz radiation includes many material fundamental resonances in condensed matter, including lattice vibrations (phonons),

superconducting energy gaps, spin quasi-particles etc. Rotational and vibrational modes are electromagnetic fingerprints of many important materials and normally lie within the THz band.

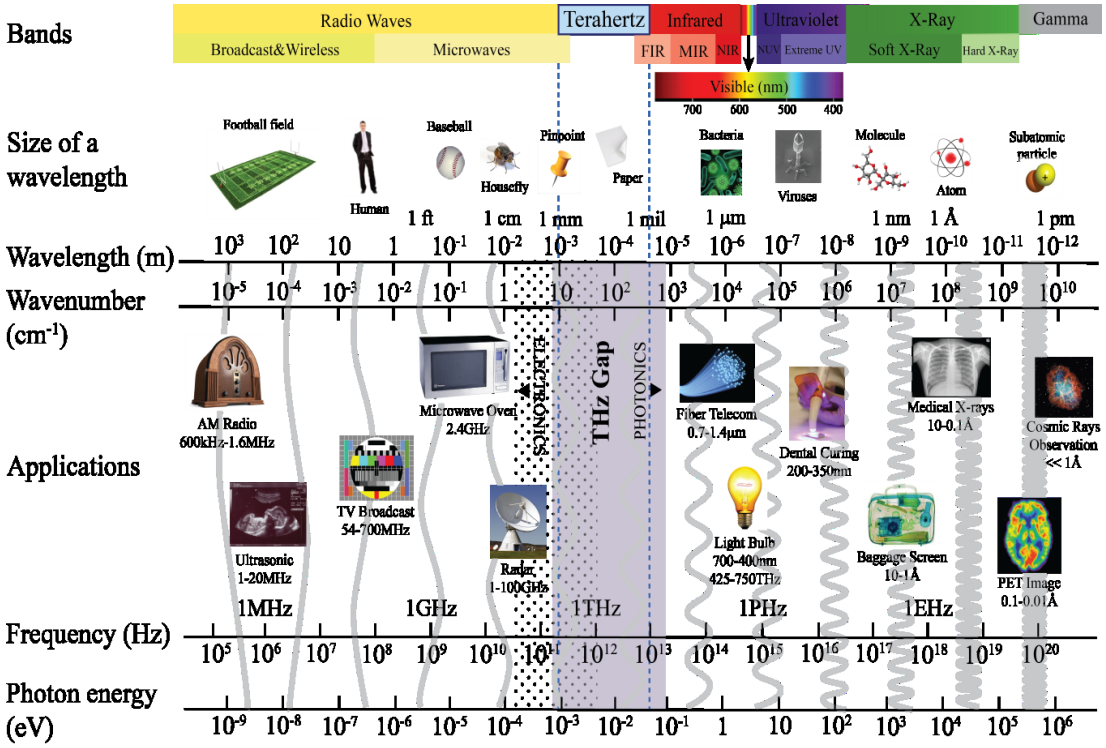

Figure 1.1 The THz band within the electromagnetic spectrum.

The extreme contrast of THz properties in different media is useful for applications in imaging and inspection. On the one hand, a strongly polar liquid such as water is highly absorptive in the THz region, whereas metals are highly reflective at the same frequencies due to their high electrical conductivity. On the other hand, nonpolar and nonmetallic materials such as paper, plastics, clothes, wood and ceramics that are usually opaque at optical wavelengths, are transparent to THz radiation.

For what concerns safety, THz radiation is also considered harmless for both the samples and the operator due to its low photon energy (4 meV at 1 THz). In fact, interest in THz radiation flourishes from its ability to penetrate deep into organic materials without the risk of damage related to radiation ionization such as X-rays (photon energy in the keV scale).

THz imaging is capable to provide localized information on macroscopic objects since THz possesses a range of wavelengths spanning from mm to tens of microns. In comparison with microwaves, which are capable to “see through”, THz waves provide a higher resolution since their wavelengths are shorter than those of microwaves. Meanwhile, infrared provides much better resolution compared with THz, however, it is not capable to see through the covers and dielectric materials, as required for material and packaging inspection. Thanks to the burgeoning research activities associated to THz during the past few years, higher spatial resolution down to nm could be achieved in THz imaging by employing the so-called near-field techniques. Nevertheless, there is still a wide range of possibilities associated to THz, resulting in the continuous growth of the THz community [16,22].

The research activity in broadband THz pulses began approximately in the late 1970s and early 1980s with the study of the response of photoconductors (PCs) to laser pulses [23-27]. Auston pioneered the first ultrafast photoconductive switches based on the concept of Hertzian dipoles, also referred now as Auston switches [28]. Those are simply comprised of metallic electrodes patterned on a material having sub-picosecond recombination times. Such switches have been the foundation of far-infrared generation and detection since their discovery [29] and of the well-known photoconductive antennas (PCAs). Photoconductive antennas are today widely applied in THz generation and detection.

In late 1980s, THz time-domain spectroscopy (THz-TDS) has been introduced by Grischkowsky's group utilizing a PCA system [30,31]. This certainly added momentum to the field of THz generation and detection, in turn seeding the emergence of new research fields, including the extraction of material parameters from THz-TDS measurements, as well as a series of novel applications stemming from the newly developed techniques.

Nonlinear crystals with high second-order susceptibility represent another class of traditional THz generators via the so-called optical rectification (OR) process, and of THz detectors through the technique called electro-optic (EO) sampling, respectively. Rice *et al.* provided the first experimental evidence of THz generation via OR in crystal semiconductors, although the process itself has been identified much before [32]. THz detection via EO sampling was demonstrated soon after Rice's demonstration [33].

1.2 THz generation and detection

1.2.1 THz generation via optical rectification (OR)

In the TDS approach, the pulse electric-field waveform is reconstructed in the time-domain and its frequency content is computationally analyzed via a Fourier Transformation. Among the various mechanisms for THz generation, such as photo-carrier acceleration in PCAs, OR in electro-optic crystals, plasma oscillations, electronics nonlinear transmission lines and ambient air, PCAs and OR are the two most common approaches for generating broadband and pulsed THz beams. The latter is the generation technique of choice in most of the experimental investigation presented in this thesis.

The interaction between electrons in a particular material with the external electromagnetic waves is the foundation for most of the optical phenomena in which the electrons displacement sustains the polarization field. As the magnetic polarization is always negligible at optical frequencies, the optical response of a medium is dominated by the electric dipole oscillations associated to electrons. The electric dipole moments are proportional to the amplitude of the applied optical field in the linear optical regime, where the optical response of the medium oscillates with the same frequency of the external field. Following the classical bounded-electron description, the nonlinear regime occurs when the applied field is strong enough to induce a large electron displacements from its static location [34]. This displacement results in a generally inharmonic response. In addition, when the electrons moves along an asymmetric bonding potential, the system exhibits a quadratic nonlinear polarization, and emits frequency products of the driving field. As results, femtosecond laser pulses with a broad spectrum can generate broadband THz pulses upon nonlinear frequency conversion. In particular the OR is a second order optical nonlinear process that enables the generation of few cycle THz waveforms roughly in the temporal scale of the optical pulse envelope. Optical rectification is a popular choice for THz pulse generation via high-energy ultrafast sources (μJ to mJ pulse energies) because the pump laser saturation threshold is much higher than that in PCAs [35-40].

Optical rectification was first observed in 1962 by Bass *et al.* using Ruby lasers in a KDP crystal [41]. Almost ten years later, generation of far-infrared radiation through OR was first demonstrated using $LiNbO_3$ [42]. A very significant experimental effort has been devoted in

literature to the investigation of the EO properties of different crystals and materials in order to optimize the generation of THz through OR. The most suitable materials include traditional semiconductors such as GaAs, GaSe, InP and ZnTe [32,42-45], organic crystals such as the ionic salt 4-dimethylamino-*N*-methyl-4-stilbazzolium-tosylate (DAST) [46], and many others [47-49].

Optical rectification can be described as a quadratic difference-frequency generation (DFG) process occurring when wide-band optical illuminations are considered. In a quite simplified description, the components at different excitation frequencies mix in a DFG process, generating lower-frequency products. It is possible to demonstrate that for transform-limited pulses, the waveform arising from this process resembles the second derivate of the driving pulse envelope.

Hence, the second-order nonlinear susceptibility ($\chi^{(2)}$) of a semiconductor crystal can be exploited for the generation of THz radiation. The second-order susceptibility determines the magnitude of the induced polarization and therefore directly determines the efficiency of the process [43]. The overall efficiency of DFG process generally depends on the phase matching condition between the fields involved, i.e. the conservation of the total optical momentum in the frequency mixing. However, the processes of OR basically cancel out the phase contribution of the pump phase. It turns out that the only significant mismatch is then between the group velocity of the pump pulse and the phase velocity of the THz wave, therefore requiring matching between the THz refractive index and the optical group index.

Let us consider a rectified polarization induced by an ultrafast optical pulse. An optical pulse can be expressed as

$$E(t) = E_0(t)e^{-i\omega t} \tag{1.1}$$

where $E_0(t)$ is the time-dependent field amplitude, t the time and ω the optical carrier angular frequency. The rectified nonlinear polarization depends on the optical pulse envelope. Hence, the spectral bandwidth of the resulted radiation is proportional to the reciprocal of the duration of the optical pulse. Figure 1.2 shows the electric field of a Gaussian optical pulse propagates through a second-order nonlinear medium and the corresponding nonlinear polarization induced by OR.

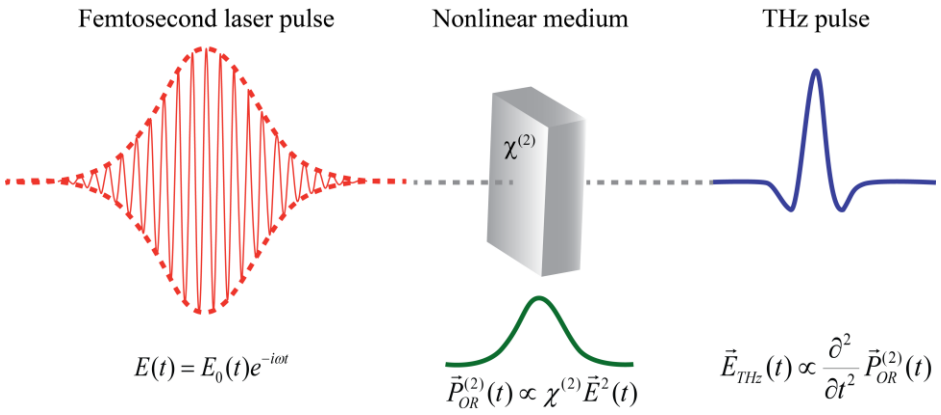

Figure 1.2 **Optical rectification (OR), a second-order nonlinear effect, whereby an ultrafast electric field pulse is rectified in a $\chi^{(2)}$ medium. The ultrafast pump pulse induces a transient polarization, which in turn emits THz pulse. The time evolution of the THz pulse is given by the second time derivative of the polarization transient.**

The time varying polarization is a source of electromagnetic radiation. The optical response can be described by generalizing the polarization field $\vec{P}(t)$ as a power series in the field amplitude $\vec{E}(t)$:

$$\vec{P}(t) = \chi^{(1)}\vec{E}(t) + \chi^{(2)}\vec{E}^2(t) + \chi^{(3)}\vec{E}^3(t) + \cdots \equiv \vec{P}^{(1)}(t) + \vec{P}^{(2)}(t) + \vec{P}^{(3)}(t) + \cdots \qquad (1.2)$$

The quantities $\chi^{(2)}$ and $\chi^{(3)}$ are the second- and third-order nonlinear optical susceptibilities, respectively. Each nonlinear term represents a number of possible interactions, providing different frequency mixing mechanisms. It can be demonstrated that for the non-purely-monochromatic case, the second order polarization term is the source of a quasi-static field component, proportional to the second derivative with respect to the time *t* of the polarization term for the OR, $\vec{P}_{OR}^{(2)}(t)$, as shown in Fig. 1.2,

$$\vec{E}_{THz}(t) \propto \frac{\partial^2}{\partial t^2}\vec{P}_{OR}^{(2)}(t) \qquad (1.3)$$

where the time-domain polarization transient is expressed by $\vec{P}_{OR}^{(2)}(t) \propto \chi^{(2)}\vec{E}^2(t)$, indicated by the second term in Eq. (1.2) [48].

1.2.2 THz detection via electro-optic (EO) sampling

A variety of techniques have been developed for the detection of THz pulses, including optically gated PCAs [29], interferometric techniques aided by helium cooled bolometers [50], pyroelectric detectors [51], and EO sampling [33,52-54]. In the framework of imaging applications, EO detection provides a convenient process where spatially resolved THz imaging can be accomplished without spatially scanning the object. Based on this technique, the detection of a THz beam spatial profile has been realized [55]. In this thesis, we will focus on the THz pulse detection via EO sampling, which will be explained as follows.

Free-space EO sampling utilizes second-order nonlinear crystals to couple the polarization state of a probe pulse and the field amplitude of a co-propagating THz pulse. The underlying mechanism is the Pockels effect. Fundamentally, it is a nonlinear coupling effect between a quasi-static electric field and a laser beam in the sensor crystal [38,56]. Similarly to the generation process, the de-synchronization between the optical pulse envelope and the THz phase front determines the actual bandwidth of the detection. The probe pulse, often an ultrashort pulse, plays the role of sampling the THz electric field at a specific instant.

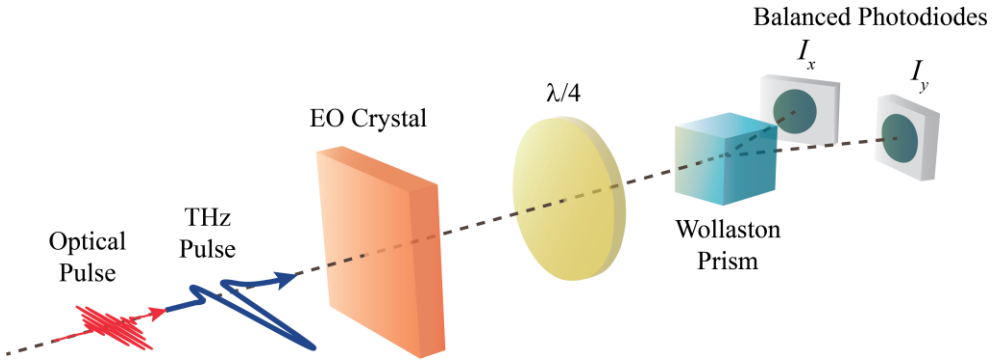

Figure 1.3 **Schematic diagram of the free-space EO sampling apparatus (EO: electro-optical; $\lambda/4$: quarter-waveplate; I_x, I_x: intensity detected at photodiodes)**

Figure 1.3 illustrates a typical setup for the free-space EO sampling used to measure field-induced birefringence. Ideally, the optical group velocity matches well the THz phase velocity in the EO crystal, therefore the optical pulse will feel a constant electric field induced by the co-propagating THz pulse. A quarter-wave plate ($\lambda/4$) and a polarizer (a Wollaston prism) are used

to extract the two circular polarization components of the transmitted optical field. Their power is then compared by using the two inputs of a balanced photodetector. For a linearly polarized field impinging on the detection crystal, a THz-induced birefringence results in an increased ellipticity of the output polarization. A pair of balanced photodetectors reveals the unbalance in the power carried by the two circularly polarized components.

1.2.3 The crystal of choice: Zinc Telluride (ZnTe)

Incidentally, one of the most effective and popular sources of high energy ultrafast optical pulses, the broadly available Ti:Sapphire lasers, possesses its peak emission efficiency around a wavelength of 800 nm, which is quite optimal to obtain velocity matching in Zinc Telluride (ZnTe) crystals, even for significant crystal thicknesses. For this reason, the ZnTe crystals represent the medium of choice for generation and detection in many TDS systems [16].

ZnTe is a zincblende crystal and possesses a noncentrosymmetric structure, in other words, it has no inversion symmetry. Figure 1.4 shows the crystal structure of ZnTe, where the asymmetric charge distribution due to the inclination of the electron charge distribution towards the Te atoms can be observed in the relevant chemical bond caused by the higher electronegativity of Te. In turn, this contributes to an asymmetric potential energy along the chemical bond.

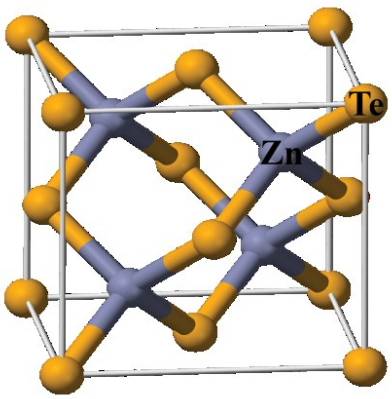

Figure 1.4 **Lattice structure of a ZnTe crystal, contributing to the asymmetric charge distribution and hence the asymmetric potential energy [57].**

ZnTe belongs to the crystal class of $\bar{4}3m$, comprising one independent component among the three non-vanishing contracted matrix elements as shown in the *d*-matrix below, i.e. $d_{14} = d_{25} = d_{36} = 4$ pm/V.

d-matrix of ZnTe: $\begin{pmatrix} 0 & 0 & 0 & d_{14} & 0 & 0 \\ 0 & 0 & 0 & 0 & d_{14} & 0 \\ 0 & 0 & 0 & 0 & 0 & d_{14} \end{pmatrix}$

In the optical THz generation geometry, a linearly polarized optical beam propagates along the [110] axis of the ZnTe crystal with an angle of θ between the optical field and the [001] axis, as illustrated in Fig. 1.5 (a). THz emission is always optimized by aligning the optical field along the chemical bonds between Zn and Te, i.e. for $\theta = \sin^{-1}\sqrt{2/3}$.

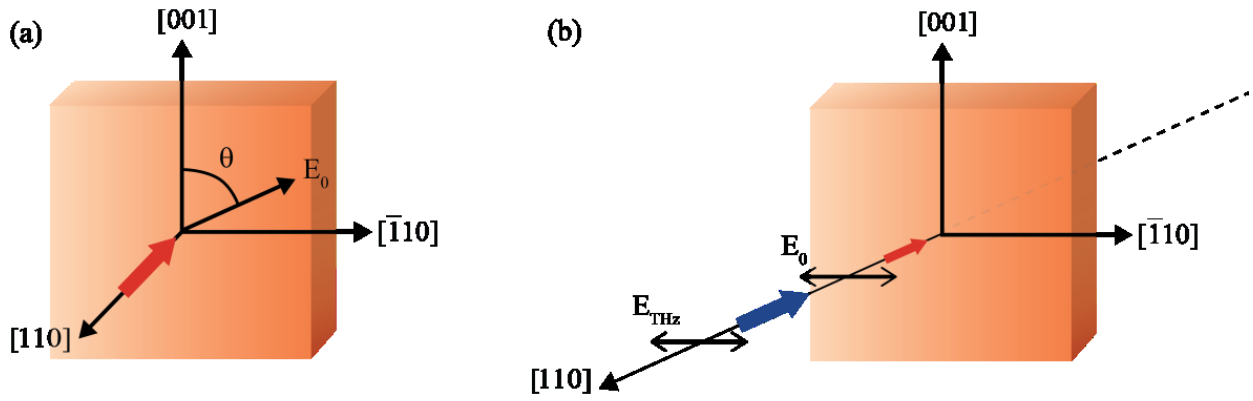

Figure 1.5 **(a) THz generation by projecting a linearly polarized optical beam on a (110) ZnTe crystal at a normal angle. θ is the angle between the optical field and the [001] axis. (b) THz detection where both optical probe and THz field possess a polarization parallel to the $[1\bar{1}0]$ direction of the ZnTe crystal [57].**

Figure 1.5 (b) illustrates the detection of THz via EO sampling using the same nonlinear crystal, i.e. ZnTe. The detectable field-induced birefringence (see Section 1.2.2) reaches its optimum by aligning the polarization state of both THz electric field and optical field parallel to the direction $[1\bar{1}0]$ of an <110>-oriented crystal.

1.2.4 Femtosecond laser

As we can understand from its name, a femtosecond laser is defined by its optical pulse duration in the range of femtoseconds (1 fs = 10^{-15} s), well below 1 picosecond (1 ps = 10^{-12} s) which positions it into the domain of ultrafast lasers or according to another familiar appellation, ultrashort pulse lasers. Due to their characteristic of being ultrafast and ultrashort, femtosecond lasers have been widely used in the study of ultrafast phenomena in the subpicosecond time scale. In addition, the peak intensity is brought to an extremely high level by confining the intensity in a short time period. Hence, such ultrafast and high intensity pulses can be further utilized to investigate their interaction with a material by studying, for example, the induced optical response, as well as the change in the properties of the material, possibly caused by different kinds of optical excitations such as ionizations, transients currents, induced polarizations lattice vibrations, etc.

Ti:sapphire-based lasers are among the most widely diffused bulk femtosecond lasers and experienced a significant revolution in the 1990s following the development of the so-called self-mode locking techniques. By this date, it is one of the mostly used laser sources in THz-related research activities [58].

1.3 Terahertz time-domain spectroscopy

Pump-probe techniques are widely used to investigate transient events by splitting a laser beam into two (as pump and probe beams, respectively). Fundamentally, the experimental scheme for THz-TDS using a femtosecond laser is based on a pump-probe technique.

In a pulsed THz system (shown in Fig 1.6), the optical beam delivered by a Ti:sapphire-based laser is also split into pump and probe beams. Here, one of the beams will be sent through a translational stage to provide a relative time delay (indicated as the optical delay). The optical pump pulse illuminates the emitter and generates the THz pulse, then travels through a distance in free space, and finally focuses on the detector. The THz-induced signals in the detector are measured by the probe pulses. One of the advantages of using a pump-probe technique is that the pump and probe pulses have a defined temporal relationship because they come from the same

source. The probe pulse samples the THz pulse and records its electric field as a function of the time delay while the beam propagates along the optical delay line. The spectral distribution of the THz pulse in the frequency domain can be obtained by computing the Fourier transform of the temporal waveform, $E(t)$ [16],

$$\tilde{E}(\omega) \equiv A(\omega)e^{-i\phi(\omega)} = \int dt\, E(t)e^{-i\omega t} \tag{1.4}$$

where A is the spectrum amplitude, ϕ is the phase, ω is angular frequency and t is the time. The THz field in the frequency domain provides complex values, comprised of both amplitude and phase. Such information is difficult to be accessed via other techniques, thus making THz-TDS a unique method in coherent spectroscopic detection. It means that the THz response of the target sample within the THz bandwidth can be obtained by simply recording the waveform of a THz pulse upon its interaction with the target sample, followed by the extraction of the spectrum associated to the THz pulse through Fourier Transform [31].

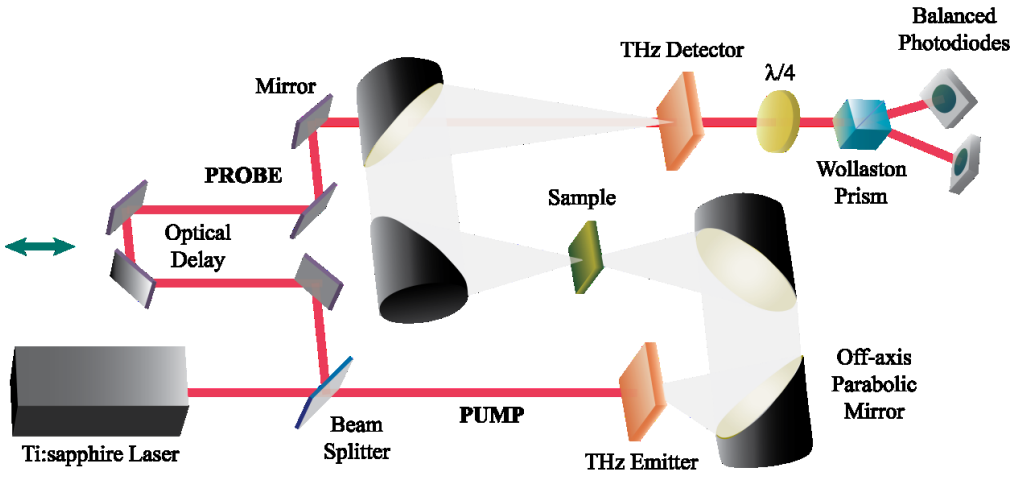

Figure 1.6 **Schematic of a typical setup for the generation and detection of THz pulses using femtosecond optical pulses from a Ti:sapphire based system.**

The THz-TDS is a useful technique to implement dynamic spectroscopy because of its high temporal resolution (provided by its pulse duration in the picosecond scale). Additionally, the background noise can be dramatically suppressed to push up the signal-to-noise ratio of the measurement (especially for performing spectroscopy featured by a high background radiation, typically comparable with the signal), since THz-TDS applies time-gating in sampling the THz

pulses. Figure 1.7 shows an example of a typical THz waveform and its spectrum measured using a standard THz-TDS technique.

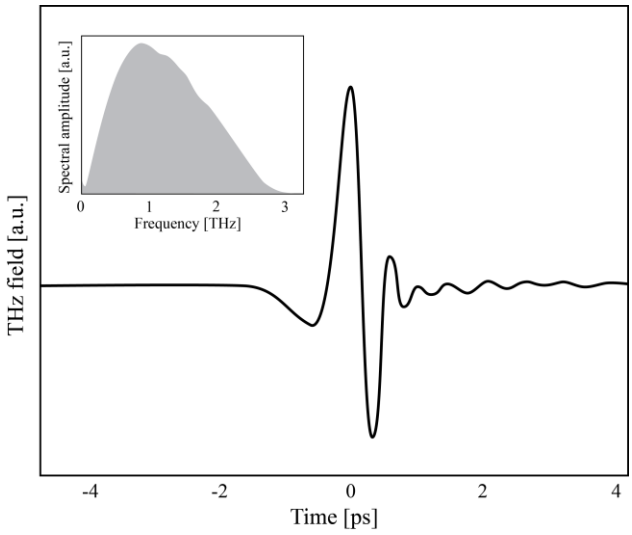

Figure 1.7 **An example of THz waveform generated via optical rectification and detected by electro-optical sampling employing a second-order nonlinear medium. The inset shows the corresponding spectrum obtained from a Fourier transform.**

1.4 Terahertz imaging

In general, THz research activities have mainly focused on developing a stable and reliable THz system, in terms of both generation and detection. More recently, the focal point has gradually shifted to practical applications. Science and technology development using electromagnetic waves at THz frequencies is a relatively new but fertile and intriguing field of research, especially if compared to the study of wave characteristics in the rest of electromagnetics band. By far, most of the applications using THz waves can be mainly sorted into the following two categories, i.e. THz wave spectroscopy and THz wave imaging. The earliest example of THz imaging is the passive submillimeter sensor, which has been used for many decades for space imaging applications. A heterodyne detector either on the Earth or on a satellite is used in these sensing systems to detect the amount of THz radiation emitted by distant galaxies [59,60]. Pulsed table-top THz imaging was first demonstrated by Hu and Nuss in 1995 using a traditional

scanning system to acquire two-dimensional (2D) images for packaging inspection and of biological objects [61]. Since then, many applications utilizing THz imaging have been developed in different fields. As THz applications evolve towards macroscopic imaging, so does the interest in imaging microscopic objects using THz radiation. However, THz far-field imaging is strongly limited by the inherent low spatial resolution imposed by its long wavelength, hampering THz capability in microscopic imaging. Such limitation in terms of spatial resolution associated to far-field imaging and due to the nature of diffraction itself will be explained in the next section.

1.4.1 The diffraction limit

The wave nature of light dominates the formation of images. If an object is imaged through a finite aperture, the image reconstruction is affected by the diffraction introduced by the aperture. As a result, the image of a point object is a finite-sized spot. A stringent criterion for resolving two objects was firstly formulated by Ernst Abbe in the early 1870s in an attempt to improve the performance of optical microscopes. Abbe concluded that two illuminated objects can only be resolved if they are separated by a distance, Δ, greater than $\lambda/(2n\sin\theta)$ [62,63]. Here,

$$\Delta = \frac{\lambda}{2n\sin\theta} \tag{1.5}$$

where λ represents the wavelength, n is the refractive index of material, θ is the angle through which light is collected in radians unit, ($n \sin\theta$) is the numerical aperture (NA). This means that the spot size is not allowed to shrink indefinitely in the so-called Fraunhofer regime (far-field). Abbe stated that the resolution achievable with a certain imaging system is directly related to the wavelength of light and the aperture of the optics involved. Subsequently, Rayleigh formulated the Rayleigh criterion to resolve two adjacent objects, also known as angular resolution.

$$\Delta = \frac{1.22\lambda}{2n\sin\theta} \tag{1.6}$$

Rayleigh criterion states that the two objects are just resolvable when the center of the diffraction pattern of one is directly over the first minimum of the diffraction pattern of the other [64], as shown in Fig. 1.8.

The two objects can only be resolved if they are apart from each other of at least such distance. By substituting the ($n \sin\theta$) term in Eq. (1.6) - with NA ≈ $(2N)^{-1}$ ≈ $D/2f$, where N is the f-number, D is the diameter of the imaging lens, and f is the focal length of lens (equivalent to the distance of the object), the angular resolution can then be further converted to the spatial resolution via multiplying the angle by the distance of the object.

$$\Delta = 1.22\lambda\frac{f}{D} \tag{1.7}$$

Equation (1.7) indicates that the diffraction of light actually limits the spatial resolution of a far-field imaging system to a value comparable to the optical wavelength.

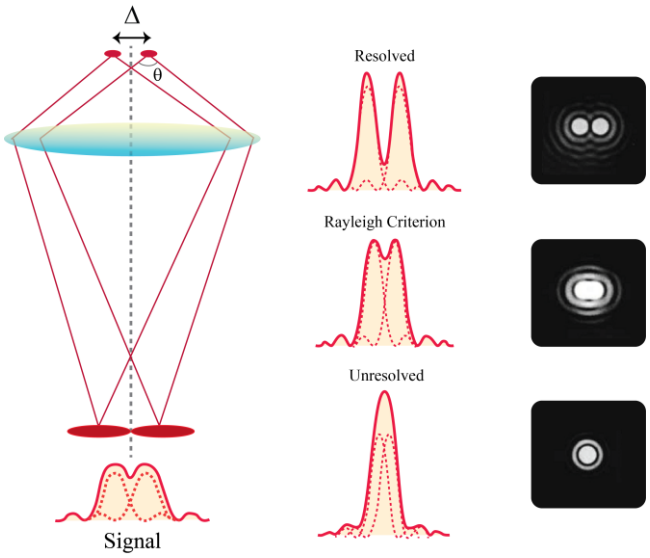

Figure 1.8 **Rayleigh's simple argument states that the two images are just resolvable when the first diffraction minimum of one image coincides with the maximum of another, i.e. the well-known Rayleigh criterion for diffraction-limited imaging system.**

1.4.2 Sub-wavelength spatial resolution in terahertz imaging

In accordance to the Rayleigh's criterion, the spatial resolution of THz wave far-field imaging is limited to a barely sub-millimeter range due to the long wavelengths associated to THz radiation. For example, the spatial resolution in the far-field for a wavelength corresponding to 1 THz is around 180 μm in vacuum (typically associated to the use of an off-axis parabolic mirror featured by 2 inches diameter and 2 inches focal length). Such resolution is often inadequate for

real world applications. For instances, many biological cells possess relevant features in the micron or sub-micron scale. THz has been also proposed as a tool to monitor carrier distribution in semiconductor devices, often exhibiting complicated morphology in the deeply sub-micron scale. Finally, macro-molecules cannot be discriminated by normal THz imaging, although they can possess very intense resonances in this spectral region. For this reason, a spatial resolution much smaller than typical THz wavelengths, so called THz sub-λ imaging, is desirable. Several approaches have been proposed and successfully implemented to obtain a sub-λ imaging resolution based on near-field techniques. We can talk of near-field imaging if the object distance from the source is shorter than the wavelength. According to Abbe, if a sub-λ scattering center is illuminated with light, then the result is a non-propagating wave component in the immediate vicinity of the sample, often denoted as the near-field contribution. Such static field component possesses a spatial dynamics induced by the scattering object morphology and decays quickly with distance. If a second sub-λ scattering object is placed in proximity of the first, a radiated field originates from the interaction of the two scattering elements. This principle (in a number of different embodiments) is commonly exploited to reconstruct images with sub-λ resolution.

We can classify here the typical approaches in either 'aperture' or 'apertureless' near-field techniques. The former usually involves a sub-λ size aperture to limit the detection or generation area. In essence the aperture locally converts the near-field component into a radiating field component. The aperture is then spatially translated enabling the point by point (raster scan) reconstruction of the field profile on the imaged plane. In the THz domain, this approach has been successfully implemented using circular, optical and rectangular sub-λ apertures, leading to spatial resolutions of 40 μm, 50 μm and 10 μm, respectively [65,66,68]. Yet, these methods are featured by some limitations. The circular aperture method suffers from a limited THz throughput scaling as r^6, where r is the transverse resolution. The optical aperture, also known as dynamic aperture, is also hampered by a low THz throughput. Besides, the samples used are typically restricted to semiconductor substrates. Although the THz throughput can be enhanced using rectangular apertures, the field enhancement is confined inside the slit and the sample size is restricted by the slit width.

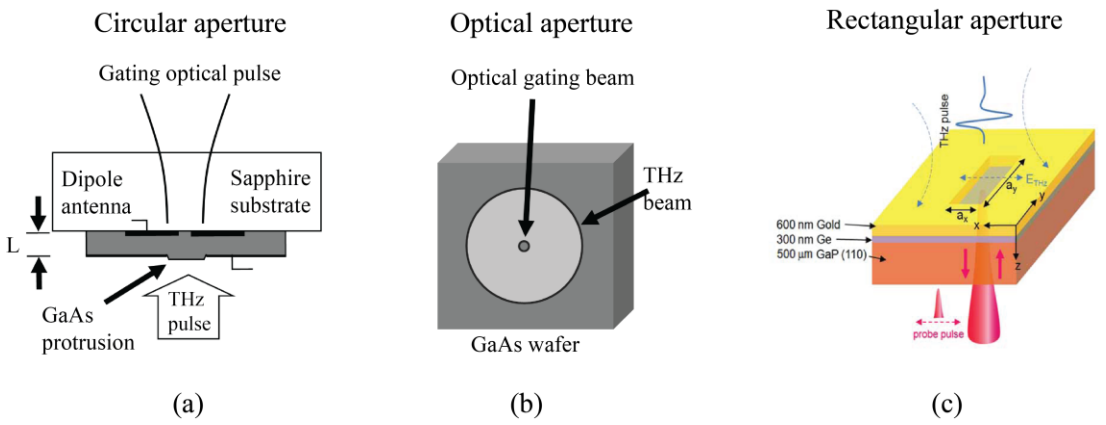

Figure 1.9 **Aperture-based near-field techniques. The image is realized based on raster scanning employing sub-λ apertures.**

THz near-field imaging has been further developed to achieve sub-λ resolution down to the nanometric scale based on apertureless approaches. These techniques employ sub-λ tips to scan the THz illuminated object, and are thus named tip scattering [69], tip absorption [70] and tip enhanced THz emission microscopy [71]. Although these approaches are capable to achieve spatial resolutions down to the sub-λ scale, they are usually suffering from a poor signal-to-noise ratio (SNR). The efficiency of a secondary scattering element in converting near-field into radiated field also scales approximately as r^6 following the Bethe's relation [72], where r is the aperture radius. Furthermore, such techniques generally suffer from the usage of fragile sub-micrometers metal tips, leading to difficult interactions between the tip and the sample surface.

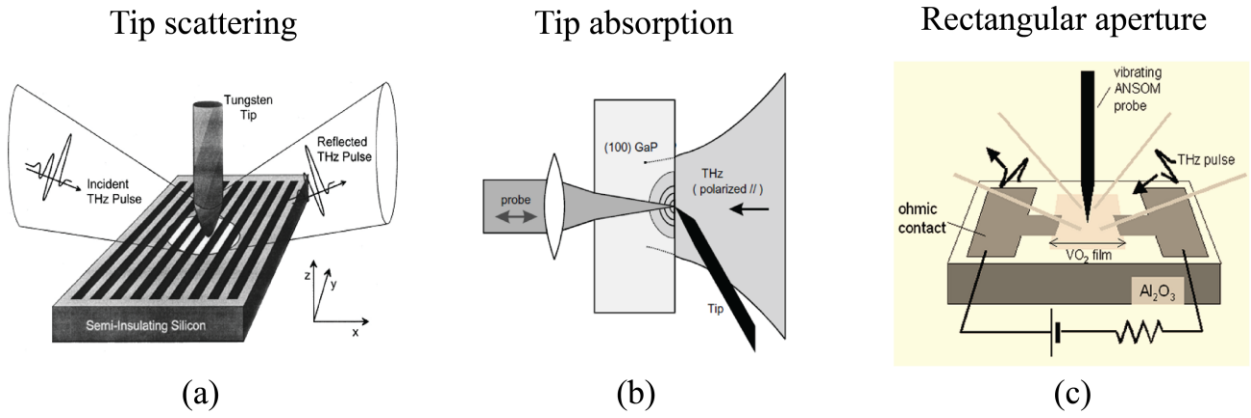

Figure 1.10 **Apertureless-based near-field techniques utilizing sub-λ tips for object scanning.**

Yuan *et al.* demonstrated that the SNR could be boosted using a sub-λ THz source via OR, by using a focalized optical pump to generate a THz field spatially localized on deeply sub-λ dimensions on the nonlinear crystal (see Section 1.2.1) [8-10]. Such a boost simply originates from the observation that localizing an optical wave generally increases the resulting local THz field intensity. Hence, by moving the THz source in proximity of a semitransparent object, the SNR of the image is not constrained by the Bethe's relation. In this dissertation, this method has been selected to generate an extremely localized THz source in the sub-λ scale.

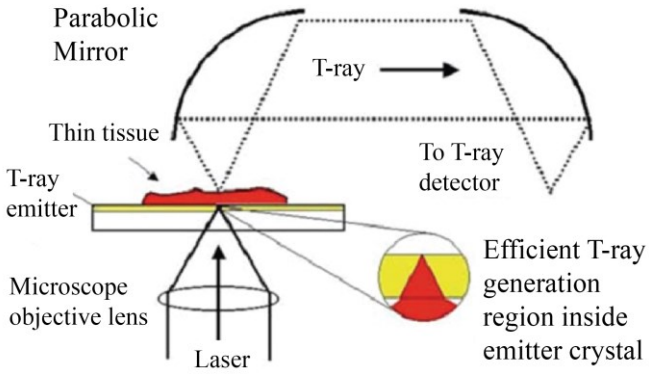

Figure 1.11 **THz source spatially localized on a nonlinear crystal, used to achieve sub-λ spatial resolution while improving the SNR.**

1.5 Dissertation objectives and organization

This dissertation aims to develop an understanding on the inherent aberration encountered in profiling sub-λ THz sources using a standard knife-edge (KE) technique and the corresponding solution. Besides, we proposed an all-optical knife-edge (AOKE) technique to characterize the sub-λ source, aiming to eliminate the use of actual blades. Furthermore, we achieved the objective of designing the first solid-state device for coherent THz detection, relying on the terahertz field-induced second harmonic generation achieved in a single micro-slit (specifically, in between a pair of electrodes immersed in silica).

The dissertation is arranged as follows. In this chapter, we have stated the objectives of this dissertation and we have introduced the general know-how at the basis of the works reported here, including some background on THz radiation, THz generation and detection, the choice of

the nonlinear medium used in THz generation and detection, the concepts of THz-TDS, THz imaging and the approaches usually employed to achieve sub-λ THz imaging.

In Chapter 2, we focus on the formalization of the key criterions related to the characterization of a sub–λ THz source using the standard KE technique, supporting our theory with experiments.

In Chapter 3, building on the experience acquired in performing the spatio-temporal KE characterization, we present a novel fully-optical optical knife-edge (AOKE) technique.

In Chapter 4, we introduce what is, to the best of our knowledge, the first solid-state design for THz coherent detection by means of electric field-induced second harmonic generation (EFISH), exploiting a sub-λ THz structure. In the last chapter, both conclusions and final remarks are reported.

2 EXACT RECONSTRUCTION OF TERAHERTZ SUB-WAVELENGTH SOURCE FEATURES IN KNIFE-EDGE MEASUREMENTS

2.1 Knife-edge measurements

A growing interest in THz imaging draws in turn an increasing attention on precise and convenient characterization techniques aimed to control and improve the quality of THz sources. The knife-edge (KE) technique is one of the most-established approaches for the characterization of the spatial profile of optical beams. In its classical implementation, it is based on measuring the optical power transmitted by a blade behaving like a semi-infinite plane, blocking a portion of the optical beam. By repeating the measurement for several transverse positions of the blade in its plane, it is possible to collect the integral of the source optical power along the direction spanned by the blade. Thus, in a large number of cases, the spatial source profile can be retrieved, e.g., by direct differentiation. This approach is very mature and has the striking advantage to provide an extremely accurate measurement of the beam spatial distribution without the need of external cameras. It has been exploited for the characterization of sub-λ features that cannot be addressed with standard far-field imaging techniques [73]. For the reasons above, the Knife-edge technique is widely used in the characterization of THz beams [74-76]. Apart from the knife-edge technique, several characterization methods have been developed for THz beam profiling, such as variable apertures, single-point detectors and electro-optics crystals in conjunction to CCD cameras. The variable aperture technique is the simplest among these methods. It is implemented by placing the aperture at the transverse plane of the beam and then by closing down such aperture incrementally. Yet, this technique is not able to provide the wavefront profile and it suffers from a number of limitations caused by the diffractive nature of the beam [77]. Using a power meter, Dickhoff and co-workers successfully raster-scanned the THz beam propagating in a small polyethylene waveguide [78]. Besides, single-point detectors have been developed employing electro-optic crystals [79] as well as GaAs dipole antennas with substrate lenses [80,81], in which the beam is scanned transversely through the beam, with the goal to examine the beam profile. On the one hand, the implementation of the latter technique is

often troublesome due to the need of realigning the laser beams during the scanning process, after measuring each individual position. On the other hand, Zhang *et al.* recorded the two dimensional map of the THz electrical field using an electro-optic crystal and a CCD camera. However, these measurements are restricted by the typical low dynamic range and signal-to-noise ratio [82-84]. Most importantly, these methods can only unveil the beam profile in the far-field. In comparison, the knife-edge technique provides advantages in terms of convenience of operation and significant reduction in the artefacts stemming from diffraction. In this dissertation, the characterization of sub-λ THz sources is conducted based on the implementation of KE measurements.

In general, the spatial features of a sub-λ THz source are not accessible using time-integrated KE techniques due to the non-separable space-time nature of the radiated field and to systematic modifications induced by the blade itself. In this chapter, we show that by combining the KE technique with a time-resolved EO sampling, the space-time coupling can be addressed and the source field profile exactly reconstructed. Let us recall some basic concepts considering the reference system in Fig. 2.1 for a beam propagating along the z coordinate. The blade is defined in the plane $z = 0$ and covers the optical field on $x_0 > 0$. If $I(x, y)\,dy$ is the intensity distribution of the optical field in the plane of the blade, the collection of the transmitted power for several positions of the blade edge x_0 (varied through small steps dx) basically implements the operation $\int_{-\infty}^{x_0}\int_{-\infty}^{\infty} I(x,y)dxdy$. This measurement, after performing a derivative along x, provides the x varying function $\int_{-\infty}^{\infty} I(x_0,y)dy$, i.e., the integral projection of the field intensity along y.

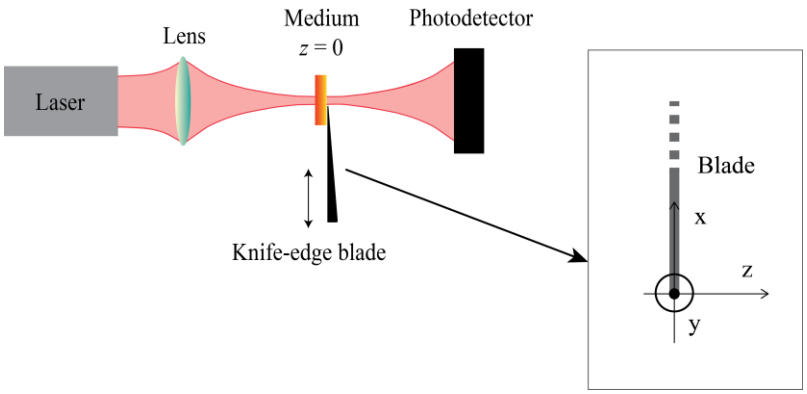

Figure 2.1 **The typical arrangement for a standard KE measurement and the reference system when the blade is in the plane $z = 0$ for $x_0 > 0$.**

When the intensity can be expressed as the product of two independent functions $I(x, y) = I_x(x)\, I_y(y)$, i.e., it is *separable* in x and y, the KE along x directly provides the estimation of the x varying component $I_x(x) \int_{-\infty}^{\infty} I_y(y)dy$, and the same consideration can be implemented for the y varying component (see, e.g., [85,86]). However, when the field exhibits a non-separable spatial distribution at the measuring plane, the KE fails to reconstruct the correct beam profile, not accessible in the single integral projection approach. The problem is usually addressed in a tomographic fashion, by cutting the transverse optical distribution with a blade at different angles in the x–y plane. The temporal dependence of the field under test is usually neglected in standard KE techniques. The method is historically designed to characterize paraxial beams described by a field distribution with a separable temporal and spatial dependence.

2.1.1 Space-time coupling in knife-edge measurements

Several kinds of wavepackets, as for instance those arising from second-order nonlinear interactions, can be featured by the non-separability of space and time [87]. In such cases, a separate spatial and temporal characterization of the field properties such as coherence [88,89] and the biphoton probability distribution [90,91] fails to provide the correct information. We remark that, at a fixed propagation distance z, the time axis t is here considered as the coordinate orthogonal to the transverse plane x-y, in the reference frame co-moving with the pulse group velocity.

When nonparaxiality is concerned, such as in the case of extremely localized sources, the field spatial and temporal coordinates are coupled, as it can be intuitively understood by considering the space-time profile of a spherical wave. This, in turn, limits the application of the standard KE technique, since the power measurement performed with an energy sensitive slow detector is equivalent to a temporal integration of the intensity distribution.

Figure 2.2 (a) and (b) shows the spatiotemporal distribution of a paraxial field in x and t (for simplicity we neglect the dependence along y) and its spatiotemporal spectrum in the space of the wavenumbers k and angular frequencies ω (please refer to Section 2.5 for the definitions of the Fourier transforms employed here). In this case the field can be factorized into two

independent temporal and spatial contributions: the profile of the field intensity along x, shown in (c) after an integration in time, provides a faithful estimation of the beam spatial distribution. Figure 2.2 (d), (e), (g), and (h) show a field with the same temporal spectrum of (a, b), but with different sub-λ spatial features. In the Fourier space, it is evident that the components of the field moved toward the straight lines $k_x = \pm\, \omega/c$. This is simply due to the nature of the Green function of the electromagnetic field that corresponds in the transformed domain to the transfer function

$$\breve{G} \propto \frac{1}{\sqrt{(\omega/c)^2 - k_x^2}} \tag{2.1}$$

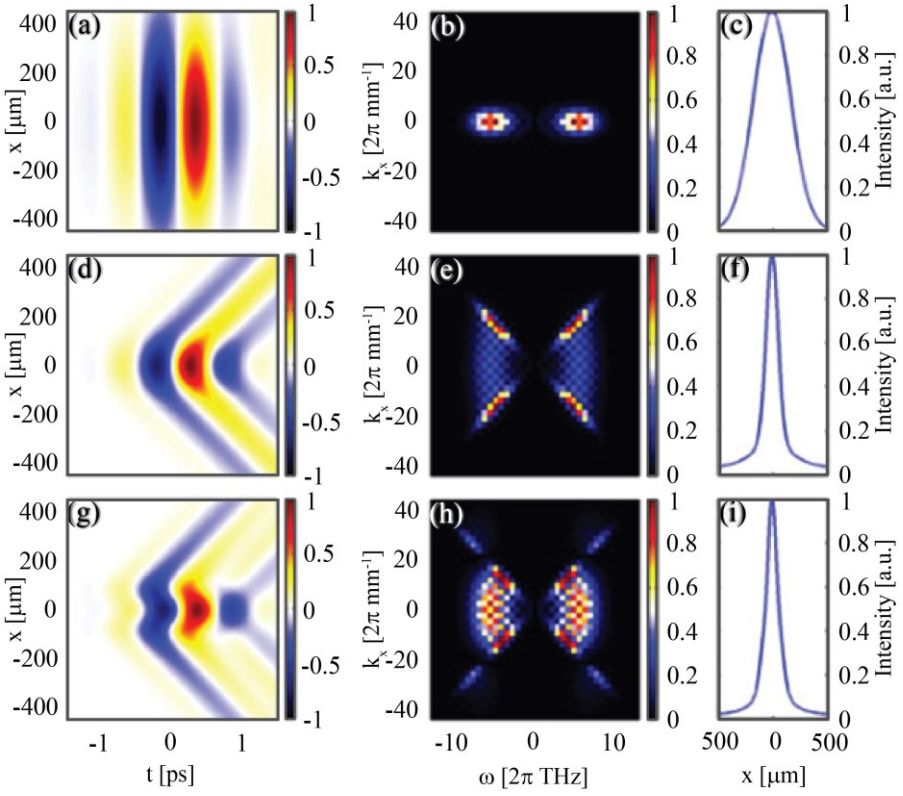

Figure 2.2 **(a)-(c) Propagation of a super-λ field: (a) field in space and time, (b) Fourier transform, and (c) intensity profile after the integration in time. (d)-(f) and (g)-(i) are the same as (a)-(c) for two different sub-λ distributions: different space-time profiles share the same intensity-reconstructed profile.**

Such function possesses a couple of complex conjugate poles on the straight lines $k_x = \pm\, \omega/c$, where the field is condensed, as it appears for the sub-λ distributions in Fig. 2.2 (e) and (h).

Such distributions evidently cannot be factorized into temporal and spatial spectral components (ω and k) in the Fourier domain, and consequently, the same holds for the direct domain (x, t).

As expected, the measurement of the intensity profile after a temporal integration does not provide a proper characterization of the field: while the cases (d), (e) and (g), (h) possess a clearly different behaviour in both space and time, their intensity profile along x is the same (f), (i). For a sub-λ distribution is, thus, necessary to address the whole spatiotemporal domain in order to obtain a reliable characterization of the field.

2.2 Combination of terahertz time-domain spectroscopy and knife-edge in characterization of a sub-wavelength terahertz source

As can be inferred from our previous considerations, a proper temporal resolution is essential to address the features of a sub-λ source. When THz is concerned, the commonly adopted detection approach, namely TDS, allows for a direct measurement of the THz electric field resolved in time. A typical example of TDS is the time-resolved EO sampling scheme [33,92]. A polarized optical probe is overlapped in space to the THz pulse under test in an EO crystal, such as Zinc Telluride (ZnTe). The duration of the THz electric-field oscillations typically largely exceeds those of the probe pulse. Hence, at different THz-optical probe delays, the probe experiences the action of a quasi-static electric field that, through the EO effect enabled by the crystal nonlinearity, translates into a modification of its polarization state. By resolving in time (via different delays) such polarization change, it is thus possible to directly map the THz electric field.

By combining a TDS approach with the KE technique, the characterization of sub-λ THz sources can take advantage of the temporal, field-resolved detection scheme, which is more than what is typically required by the 'separability' considerations expressed in the previous section. In its standard form, a time-resolved KE approach would require to measure the total power radiated by the source after the blade clipping [73]. In such a case, the measured quantity is the time-resolved energy (or average power) at different blade positions:

$$U(x_0, t) = \int_{-\infty}^{x_0} I(x, t)dx \tag{2.2}$$

where the spatiotemporal intensity profile can be readily obtained by a direct derivative of U (x_0, t) with respect to the blade coordinate. However, for sub-λ sources the requirement of collecting the total radiated power poses serious experimental issues. Conversely, for an electric-field-resolved measurement the most direct way to retrieve the spatiotemporal electric-field profile via KE would be to record a signal that is proportional to the integral of the electric field, rather than to the power. In such a case, the KE measurement would read:

$$e(x_0, t) \propto \int_{-\infty}^{x_0} e^{(i)}(x, t)dx \tag{2.3}$$

where $e^{(i)}$ (x, t) is the THz real-valued electric field under test (incident field) that may be obtained by a direct differentiation of the measured field $e(x_0, t)$. The electric field in the far-field $z \to \infty$ is proportional to the Fourier transform of the field at the blade plane. Its value at a point $x = 0$ is then proportional to the integral of the field radiated after the blade clipping, formally:

$$e(x = 0, z \to \infty, t) \propto \int_{-\infty}^{\infty} \mathbf{e}(x, z = 0, t)dx \tag{2.4}$$

(Note: we again consider only a single spatial dimension for the sake of simplicity). Thus, for an electric-field-resolved KE spatiotemporal imaging, in contrast to the classical intensity resolved case, it is sufficient to record the field at a point in the far-field of the blade plane. Operatively, the low THz fields emitted by optical rectification on sub-λ areas will require an optical system — with an impulse response h (x, y) — that allows performing TDS of a reasonably strong signal. The field in the reconstruction plane $z = z_{out}$ then reads:

$$e(x, y, z_{out}) = \iint_{-\infty}^{\infty} e(\xi, \eta, z = 0)h(x - \xi, y - \eta)d\xi d\eta \tag{2.5}$$

The field in the image plane sampled in the point $x = 0$, $y = 0$ is, thus, approximated by the integral of the field in the image plane, whenever the size of any spatial feature of interest is much smaller than the system spatial resolution:

$$\begin{aligned} e(x = 0, y = 0, z_{out}) &= \iint_{-\infty}^{\infty} e(\xi, \eta, z = 0)h(-\xi, -\eta)d\xi d\eta \\ &\approx \iint_{-\infty}^{\infty} e(\xi, \eta, z = 0)d\xi d\eta \end{aligned} \tag{2.6}$$

In our case this translates into the requirement of an impulse response function nearly constant over few wavelengths. For this purpose, we considered an imaging system composed by two off-axis parabolic mirrors of limited aperture. Since both the spatial resolution and the signal at the detection plane are directly proportional to the numerical aperture (NA) of the imaging system, a trade-off between a correct implementation of a field-resolved KE (low NA) and a reasonably high SNR in the detection (high NA) has to be found. It has to be noted that the imaged radiation is not monochromatic; hence, the effect of a finite NA also unavoidably translates into a high-pass temporal frequency filter, which accompanies our measurements. Finally, we point out that the broken radial symmetry determined by the vectorial effects accompanying non-paraxial focusing is not accounted for in our investigations [93].

2.3 Experimental setup

The experimental setup adopted for our study is sketched in Fig. 2.3. An 800 nm, 100 fs, 5 nJ train of pulses at a 80 MHz repetition rate, delivered by a Ti:sapphire ultrafast oscillator (MaiTai, Spectra Physics), is tightly focused by a 5 cm focal lens on a second-order nonlinear crystal. Due to the extreme divergence of the generated sub-λ THz field, the effective source dimension is limited by the crystal thickness. Hence, in order to produce a highly localized THz emission, the OR is excited in a <110>-oriented, 20μm-thick (sub-λ for THz) ZnTe crystal, bonded on a 500μm-thick <100> ZnTe substrate, which does not contribute to the generation. By varying the pump beam diameter in front of the lens, the effective THz beam waist can be controlled.

For the experiment reported here, the pump beam waist was set to 30 μm, i.e., nearly $\lambda/10$ of the generated THz wavelength (carrier wavelength $\simeq$ 300 μm). The THz radiation is then partially collimated by a gold coated, 2 inch aperture off-axis parabolic mirror, with a 2 inch equivalent focal length, setting the numerical aperture of the diagnostic at NA $\simeq$ 0.45 (compatible with the requirement of field integration on areas with radii < 150 μm). The collimated THz beam is finally focused into the detection crystal by a second parabolic mirror (identical to the first one), featured by a small aperture that allows an optical probe pulse to reach

the THz focus. The detection crystal is a 3 mm, <110> cut ZnTe, and a standard EO sampling scheme is employed for the THz time-resolved electric-field measurement.

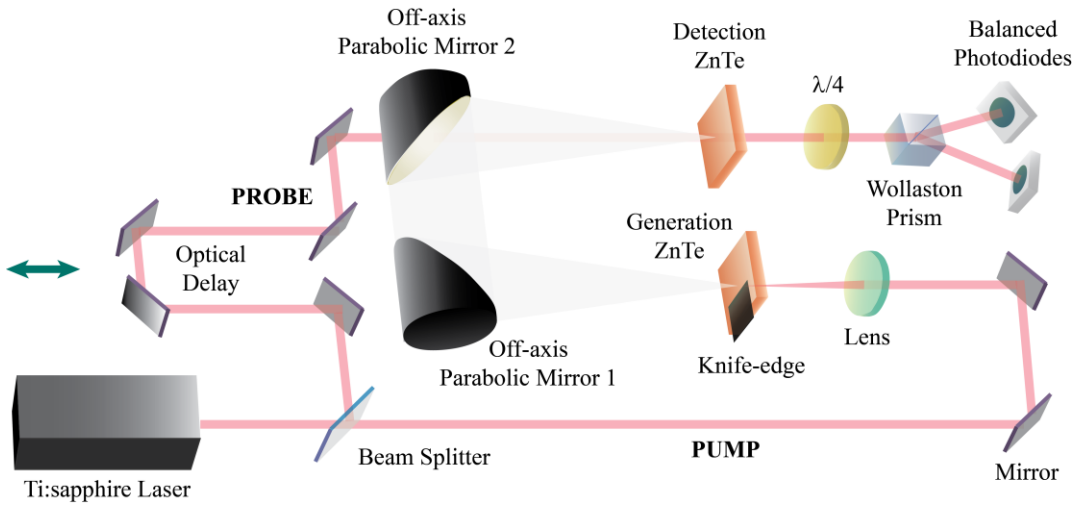

Figure 2.3 **Sketch of the experimental setup employed for the generation and characterization of the sub-λ THz source.**

The KE is performed via an aluminum blade attached directly to the surface of the generation crystal and the time-resolved electric field at the detection focus is then recorded for different blade-edge to optical pump beam distances x_0. Following our previous considerations, due to the limited NA of the imaging system, the TDS implements a time-resolved field sensitive detection, for any blade position, of the mean field at the blade plane (also the generation plane). The measured field is shown in Fig. 2.4 (a).

By taking the derivative of the measured time-resolved electric field along the blade coordinate, it is then possible to retrieve the spatiotemporal electric-field profile of the source, which is shown in Fig. 2.4 (b): an evident asymmetry along the spatial coordinate appears despite the expected spatial symmetry of the THz source. Such asymmetry observed in the spatio-temporal profile may be associated to a reduction of the signal amplitude and hence may lead to a potentially incomplete set of components in the corresponding spectrum. Such reduction in the amplitude and spectrum is particularly crucial in THz imaging and spectroscopy as the image of the sample could be distorted and the spectroscopic results might be inaccurate.

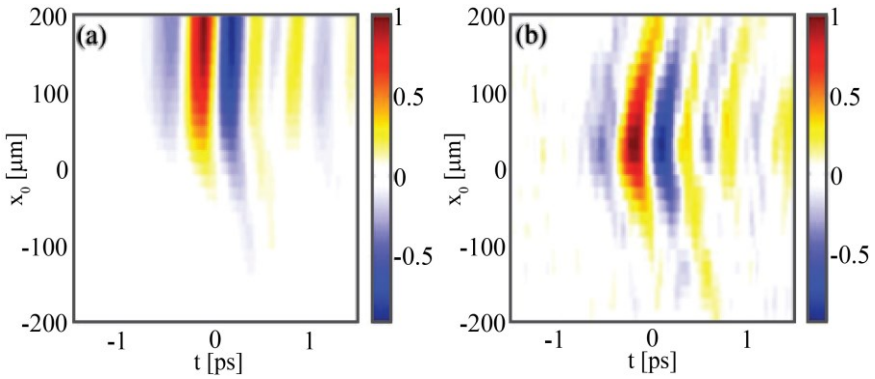

Figure 2.4 **(a) Electrical field measured in the focus of the second parabolic mirror, as a function of the blade position x_0 and time. (b) Electric field retrieved by means of spatial differentiation.**

2.4 Numerical modeling of the experimental setup

In order to investigate the asymmetry revealed by our experimental findings, we performed a set of numerical simulations with a FDTD numerical solver. We modeled all the main components of the experimental setup: a sub-λ, p-polarized (polarization parallel to the blade edge) THz source; a metallic blade; and the imaging system. The parabolic mirror sizes and foci have been chosen in order to match the NA of the experimental imaging system.

Due to computational constraints, we consider a reduced, 2D+1 geometry [$(x, z) + t$]. Although different from a full 3D+1 case, the results are qualitatively compatible with the prediction of a full 3D theory (see Section 2.5). We modeled the sub-λ source as a pulsed current source term in Maxwell's equations, polarized along y (corresponding to a p-polarization in our experiment), with a carrier wavelength, λ = 300 μm. The current source term has a 50 μm diameter (full width at 1/e) along the x-axis, no extension in the z direction, and a 0.5 ps duration (full width at 1/e).

A 10μm-thick metallic blade, extended for $x_0 > 0$ along the x-axis, was placed in the focus plane of the first parabolic mirror, 25 μm far from the source. We propagate the THz pulse for different blade-edge positions (x_0) and we monitored the electric field in a point located in the focal plane of the second parabolic mirror. The results of our simulations are reported in Fig. 2.5: panel (a) shows the field in the focus of the second parabolic mirror, while in panel (b) we plot

the reconstructed field obtained by performing the spatial derivative of the field in (a) along the moving blade direction.

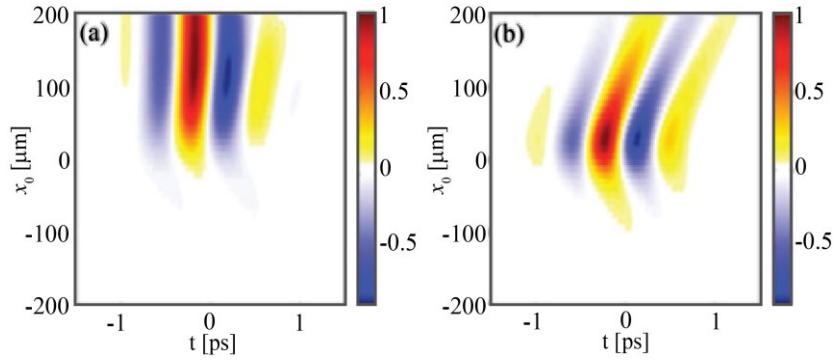

Figure 2.5 **(a) Electric field in the focus of the second parabolic mirror, evaluated through FDTD numerical simulations. (b) Electric field retrieved by means of calculating the derivative along x_0.**

The numerical results match qualitatively well the experimental findings, showing a similar asymmetry in the retrieved field. As we will see in the next section, this effect has to be regarded to as inherent to the investigated technique. In order to better understand the physical origin of this asymmetry, we developed an analytical model describing the interaction between the blade and the sub-λ source.

2.5 Theoretical establishment of field reconstruction through space-time knife-edge: a new transfer function

We present in this section the analytical derivation of the transfer function of an ideal KE+TDS system to be used for the characterization of the electric field. Under ideal conditions, the blade can be assumed as a perfectly conductive semi-infinite plane, with negligible thickness. In this case, it is possible to find an analytical rigorous solution of the scattered electric field: historically, the scattering of an electromagnetic field by a semi-infinite conductive plane is the first rigorous diffraction problem solved in electromagnetism; the solution was obtained by Sommerfeld in 1896. Here, we will directly employ the results for the derivation of the exact equation for the KE+TDS system in the case of a THz field p-polarized, i.e. parallel to the blade

edge (y polarized in the geometry depicted in Fig. 2.1). The case for a general transverse polarization is treated in Appendix 6.2. Before entering in the details, we define here the conventions on the Fourier transforms we adopt in the text: the THz electric field is defined in time t / frequency ω by the Fourier relation

$$\mathbf{e}(\mathbf{r},t) = 2\mathrm{Re}\int_{-\infty}^{\infty}\mathbf{E}(\mathbf{r},\omega)e^{-i\omega t}\frac{d\omega}{2\pi} \tag{2.7}$$

in the $\mathbf{r}$, ω space. Considering z as the propagation coordinate, it is useful to define a spatial Fourier transform for the transverse coordinates x, y as (we omit here the dependence on ω)

$$\breve{\mathbf{E}}(k_x,k_y,z) = \iint_{-\infty}^{\infty}\mathbf{E}(x,y,z)e^{-ik_x x-ik_y y}dxdy \tag{2.8}$$

that is, for the total spatiotemporal field:

$$\mathbf{e}(x,y,z,t) = 2Re\iiint_{-\infty}^{\infty}\breve{\mathbf{E}}(k_x,k_y,z,\omega)e^{ik_x x+ik_y y-i\omega t}\times\frac{dk_x dk_y d\omega}{(2\pi)^3} \tag{2.9}$$

We model the blade as a semi-infinite, perfectly conductive plane defined in $z = 0$ for $x_0 > 0$. As previously discussed, the TDS system implements the integral along x and y of a specific polarization associated with the field transmitted by the blade in the plane $z = 0^+$, i.e., for each position of the blade, we collect the quantity $\iint_{-\infty}^{\infty}\mathbf{E}(x,y,z=0^+,\omega)\cdot\hat{\boldsymbol{u}}dxdy$, where $\hat{\boldsymbol{u}}$ is a versor parallel to the transverse polarization detected by the system. This operation is equivalent to sampling the Fourier transform at zero:

$$\breve{\mathbf{E}}(k_x=0,k_y=0,z=0^+,\omega)\cdot\hat{\boldsymbol{u}} \tag{2.10}$$

With a scan along x we can then only reconstruct the integral along y of the electric field in $z = 0$, i.e., in the transformed space $\breve{\mathbf{E}}^{(i)}(k_x,k_y=0,z=0^+,\omega)$. For simplicity, we will omit the dependences on $z = 0^+$ and $k_y = 0$ in the expressions which will follow. If we consider a y-polarized input field $\mathbf{E}^{(i)} = \mathrm{E}^{(i)}\hat{\boldsymbol{y}}$ and a detection along $\hat{\boldsymbol{u}} = \hat{\boldsymbol{y}}$, we have the following exact relation between the incident $\mathrm{E}^{(i)}$ and the total integral of the field transmitted by the blade:

$$\breve{\mathrm{E}}(k_x=0,\omega) = \breve{\mathrm{E}}^{(i)}(k_x=0,\omega) - \int_{-\infty}^{\infty}\frac{2i}{s_x}\sqrt{1+\frac{cs_x}{\omega}}\breve{\mathrm{E}}^{(i)}(s_x,\omega)\,e^{is_x x_0}\frac{ds_x}{2\pi} \tag{2.11}$$

Equation (2.11) is directly obtained by evaluating the total field transmitted by a perfectly conductive half-plane, as can be found in several references (see, e.g., [80]) and reported in detail

in the Appendix 6.2. We define a "reconstructed" field e_R (x_0, t), function of the blade position coordinate x_0, by differentiating Eq. (2.11) with respect to x_0 and transforming back in the temporal domain. We, thus, obtain:

$$e_R(x_0,t) \propto \mathrm{Re}\iint_{-\infty}^{\infty}\sqrt{1+\frac{cs_x}{\omega}}\,\tilde{\mathrm{E}}^{(i)}(s_x,\omega)e^{is_x x_0-i\omega t}\frac{ds_x d\omega}{(2\pi)^2} \tag{2.12}$$

Equation (2.12) is formally equal to the Fourier transform (in the position of the blade x_0) of the input function $\tilde{\mathrm{E}}^{(i)}(s_x,\omega)$, multiplied by the radical term of Eq. (2.12). Considering that the Fourier transform of a real signal possesses a complex conjugate symmetry and that, by hypothesis, $\tilde{\mathrm{E}}^{(i)}(s_x,\omega)$ is the Fourier transform of a real signal, the relation $\tilde{\mathrm{E}}^{(i)}(s_x,\omega) = \mathrm{conj.}\,(\tilde{\mathrm{E}}^{(i)}(-s_x,-\omega))$ holds. Thus, in order to ensure that $e_R(x_0,t)$ is a real function, the radical term in Eq. (2.12) must possess a complex conjugate symmetry as well. It is easy to verify that this holds only when this term is real; thus, Eq. (2.12) can be rewritten as

$$e_R(x_0,t) \propto \iint_{-\infty}^{\infty} H\left(1+\frac{ck_x}{\omega}\right)\sqrt{1+\frac{ck_x}{\omega}}\,\tilde{\mathrm{E}}^{(i)}\times(k_x,\omega)e^{ik_x x_0-i\omega t}\frac{dk_x d\omega}{(2\pi)^2} \tag{2.13}$$

where H is the Heaviside theta function. Considering the Fourier transform of the reconstructed field, we get:

$$\tilde{\mathrm{E}}^{(R)}(k_x,\omega) \propto H\left(1+\frac{ck_x}{\omega}\right)\sqrt{1+\frac{ck_x}{\omega}}\,\tilde{\mathrm{E}}^{(i)}(k_x,\omega) \tag{2.14}$$

From Eq. (2.14), we obtain the transfer function of the KE+TDS system, where we consider explicitly the Heaviside theta function

$$\tilde{T}(k_x,\omega) \equiv \begin{cases}\sqrt{1+\frac{ck_x}{\omega}} & \text{for } k_x > -\frac{\omega}{c} \\ 0 & \text{for } k_x < -\frac{\omega}{c}\end{cases} \tag{2.15}$$

For fields with spatial localizations above the wavelength scale, the spectrum is localized in a region where the spatial frequency k_x is small when compared to ω/c, as also evident in the example in Fig. 2.2 (a) and (b). The effect of the transfer function on such fields is negligible as $\tilde{T}(k_x,\omega)$ tends to the unit value for small values of ck_x/ω. As heuristically expected, in this case the reconstructed field is proportional to the field under test, as shown in Fig. 2.6 (a) and (b)

where the distributions proposed in Fig. 2.2 (a) and (b) are multiplied in the transformed space by $\breve{T}(k_x, \omega)$ (see Eq. (2.15)).

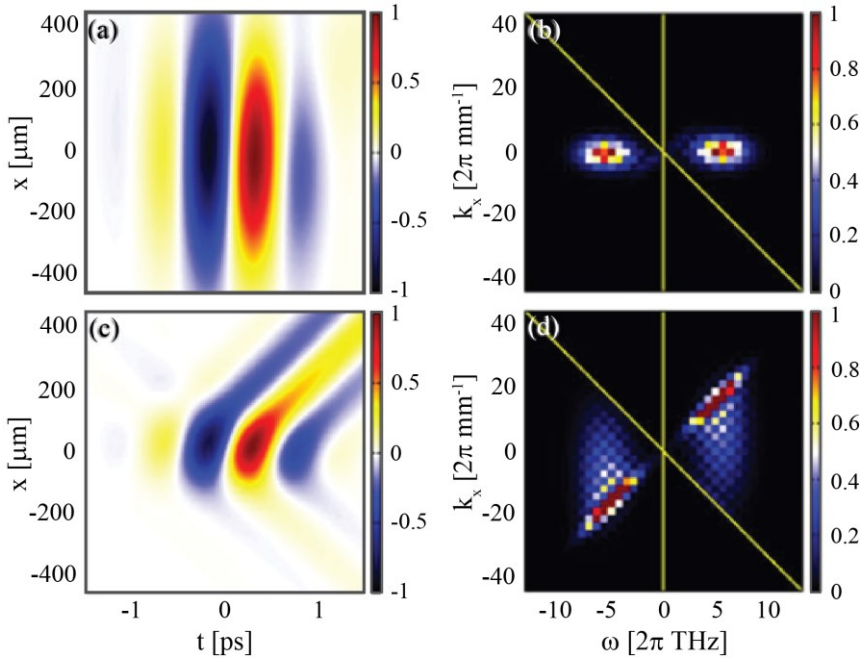

Figure 2.6 **Effect of the transfer function of the KE+TDS system for a super-λ (a), (b) and sub-λ (c), (d) fields (represented in pseudocolor). (a) and (b) Direct and transformed space of the function in Fig. 2.2 (a) and (b) after a multiplication with Eq. (2.15) in the transformed space. The lines indicate the boundaries of the region where Eq. (2.15) is zero. (c) and (d) Same for the sub-λ field in Fig. 2.2 (e) and (f).**

Conversely, the transfer function plays a relevant role for sub-λ localized fields, filtering out part of the spatiotemporal components of the reconstructed field: $\breve{T}(k_x, \omega)$ is zero for the superluminal components corresponding to the region bounded by the straight lines $k_x = -\omega/c$ and $\omega = 0$. The field reconstructed by the KE+TDS system then undergoes an asymmetric quenching of the spatiotemporal spectrum that translates into an asymmetric distribution in the direct space. This effect is shown in Fig. 2.6 (c) and (d) where $\breve{T}(k_x, \omega)$ is applied to the sub-λ distribution in the example of Fig. 2.2 (d) and (e). The asymmetric filtering effect can be now clearly recognized in the experimental and numerical results: the associated Fourier transforms, reported in Fig. 2.7 (a) and (b) respectively, possess components with low energy in the subluminal region where $\breve{T}(k_x, \omega)$ is zero.

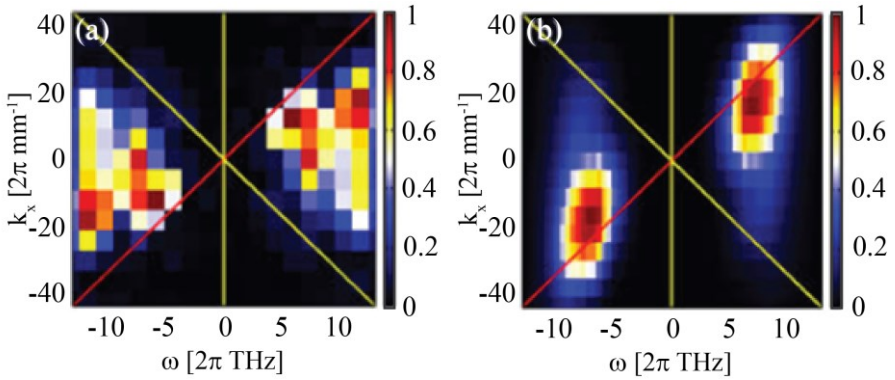

Figure 2.7 **(a) and (b) Spatio-temporal spectra of the experimental data in Fig. 2.4 and 2.5, respectively. A clear accumulation appears for $k_x = +\omega/c$ (red) and quenching for $k_x = -\omega/c$ (yellow).**

From this analysis, it is clear that the KE+TDS system can provide a measurement of the field under test only in the portion of the spatiotemporal spectrum where Eq. (2.15) is significant. However, when it is possible to guess a spatial symmetry in the field under test, this information is sufficient for the full reconstruction of the field. As the symmetry in the direct space corresponds to a symmetry in the transformed space, the missing components of the field for $k_x < -\omega/c$ are equal to the components for $k_x > \omega/c$ available in the measurement. Moreover, if the KE is implemented for negative x_0 (i.e., the blade acts for $x_0 < 0$), its transfer function becomes

$$\breve{T}_{-}(k_x,\omega) \equiv \begin{cases} -\sqrt{1-\frac{ck_x}{\omega}} & \text{for } k_x > \frac{\omega}{c} \\ 0 & \text{for } k_x < \frac{\omega}{c} \end{cases} \tag{2.16}$$

Remarkably, the term $\breve{T}(k_x,\omega)$ is significant where Eq. (2.15) is zero. In turn, a generic sub-λ field can be completely reconstructed when two different KE measurements are performed for positive and negative x_0. In this case, the investigated field in the Fourier domain can be determined with the aid of the two functions:

$$\breve{\mathrm{E}}_{\pm}^{(i)}(k_x,\omega) \propto \pm H\left(1 \pm \frac{ck_x}{\omega}\right)\sqrt{\frac{\omega}{\omega \pm ck_x}}\,\breve{\mathrm{E}}_{\pm}^{(R)}(k_x,\omega) \tag{2.17}$$

In the next section, we show the results obtained by exploiting the developed inversion method on the experimental and numerical data shown in Fig. 2.4 and 2.5.

2.6 Numerical and experimental data inversion

In order to retrieve the spatiotemporal field profile from the numerical and experimental data, we proceeded by dividing the spatiotemporal spectra by the KE transfer function *T*. After that, under the assumption of a symmetric source we recovered the missing information by imposing the spectral-spatial symmetry ($k_x \rightarrow -k_x$). Considering the source presented in Fig. 2.8 (a), and by applying the method described before on the simulated KE+TDS measurements (see Fig. 2.5), we retrieved the field shown in Fig. 2.8 (b), thus confirming the validity of the proposed method. We note however the appearance of a temporal phase shift of on the reconstructed spatiotemporal field that may be interpreted as a consequence of the *Gouy* phase shift, as recently commented by Yi *et al.* for sub-λ localized sources [95]. Finally, we performed the same analysis on the experimental data shown in Fig. 2.4.

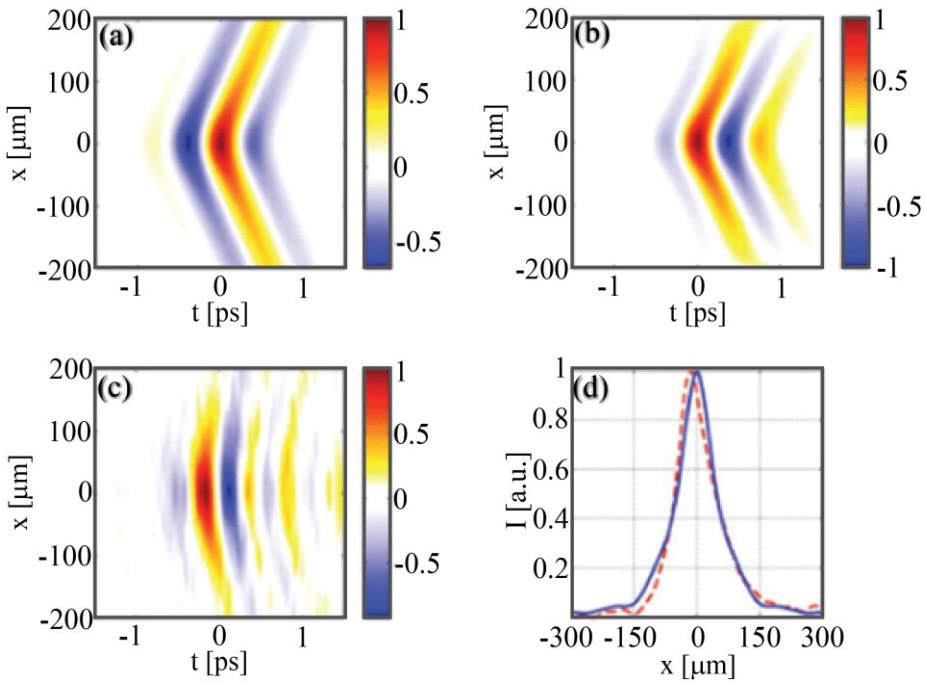

Figure 2.8 **Results from the data inversion considering the transfer function *T*. (a) Initial spatio-temporal field simulated via FDTD. (b) Retrieved field obtained via KE+TDS: under the hypothesis of a symmetric geometry. (c) Retrieved experimental field profile under the same conditions. (d) Comparison between the beam profile obtained by (blue, solid) and without (red, dashed) taking into consideration the effect of the asymmetric KE transfer function.**

The retrieved spatiotemporal field profile is presented in Fig. 2.8 (c), while in panel (d) we compare the time-integrated spatial beam profile obtained by evaluating the intensity of the retrieved field (blue) with the same quantity determined by the direct integration of the field in Fig. 2.4 (b), i.e. before the inversion through the *T*-function.

2.7 Conclusion

This chapter reports on our recent studies related to the characterization of sub-λ THz sources, the main ingredient for aperture-free THz near-field imaging. Starting from the consideration that extremely diffractive waves, e.g., non-paraxial, are featured by space-time coupling, we discussed the validity of the standard KE-based approach for a proper beam profiling. Exploiting the unique electric-field time-resolved capabilities offered by THz-TDS, we thus investigated experimentally and numerically a field-resolved spatiotemporal characterization technique relying on the combination of KE and EO sampling. We pointed out a systematic error affecting this field-resolved approach and, resorting to the exact Sommerfeld formulation of the scattering problem from an infinite, conducting half-plane, we provided a simple solution for retrieving the full spatiotemporal structure of the sampled field.

We stress that the proposed investigation is propaedeutic for properly addressing the issues related to raster-scan imaging of sub-λ structures, where systematic aberrations may arise as a consequence of an asymmetric transfer function, similarly to what presented here for a metallic blade. A transfer function is developed for the exact reconstruction of sub-λ THz field profiles, however we note that a conventional KE technique remains a mechanical technique, in which the characterization results are strongly dependent on the distance (i.e. deep-sub-λ distance) of the physical blade from the generation plane. We therefore proposed and demonstrated a novel all-optical KE (AOKE) technique, relying on the ultra-thin layer of photo-excited free carriers as the virtual blade at the exact THz source plane, to block the THz field in the characterization process. The use of a physical blade attached on the generation plane (under the constrain of a deep-sub-wavelength distance) can be eliminated and make the proposed technique more practical in real world scenarios. The relevant details will be explained in the next chapter.

3 TERAHERTZ BEAM PROFILING AT THE EMISSION PLANE VIA AN ALL-OPTICAL KNIFE-EDGE TECHNIQUE

3.1 Photo-excited free carrier as the virtual blade for sub-wavelength terahertz source characterization

In the previous chapter, we emphasized that the reconstruction of sub-λ sources by the KE technique is generally affected by the aberration caused by the non-separable space-time nature of the radiated field. We had dealt with the exact reconstruction of a sub-λ THz source by introducing a transfer function, yet the conventional KE technique is, undeniably, still a mechanical technique. In this chapter, we further investigated the issue associated to the characterization of sub-λ THz sources at the exact generation plane without using a physical KE blade. Here, we propose an all-optical KE (AOKE) technique, in which the THz field clipping is implemented by way of an ultra-thin layer of optically-excited free carriers as the virtual blade located at the output facet of the THz generation crystal. Such technique eliminates the use of a physical blade at the emission plane.

As mentioned previously, ZnTe is the nonlinear crystal of our choice (see Section 1.2.3) for both THz generation and detection. Zinc telluride is a binary chemical compound featured by a cubic crystal structure. It belongs to the category of II-IV semiconductor and possesses a band gap of 2.3 eV at a temperature T = 300 K [96]. In comparison with metals and insulators, the covalent bonds among atoms in semiconductor are moderately strong. When the temperature is equal to the absolute zero (T = 0 K), the electrons in the semiconductor are not free to move as they are bounded to their parent atoms, and hence, there is no electric current flowing in the material, where the valance bands are fully occupied and resulting in an empty conduction band. At temperature T > 0 K, the thermal effect on the semiconductor induces lattice vibrations and results in the breaking of the covalent bonds. Free electrons are then released, each of them being counter matched by a hole, i.e. a positive charge. The hole is filled up by the valence electrons from adjacent bonds and electron-hole pairs are thus generated, ultimately increasing the electric

conductivity of the semiconductor. This process is known as electron-hole pair generation, as shown in Fig. 3.1 (label **a**).

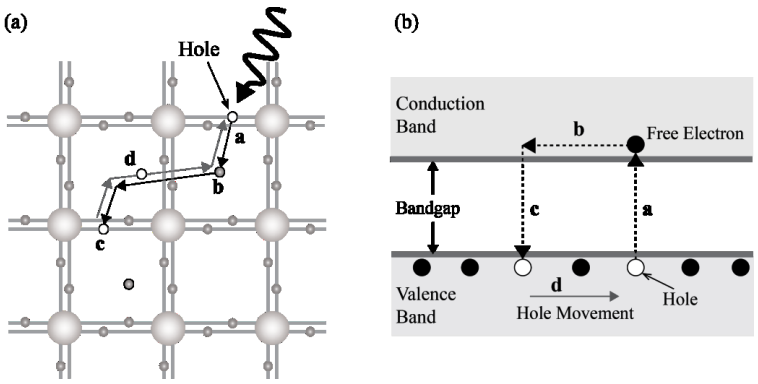

Figure 3.1 **Generation and recombination of an electron-hole pair: (a) presented in the two dimensional crystal lattice; (b) by way of an energy diagram [83].**

After a certain time period, the free electron will fill up another broken covalent bond elsewhere in the semiconductor (as shown by panel **b** in Fig. 3.1), thus "reducing" the existing hole at that particular moment. This process is known as electron-hole recombination, illustrated by panel **c** in Fig. 3.1.

Likewise, when an external field is applied on the semiconductor, the electrons distributed at the valance band and at the bottom of the conduction band gain enough kinetic energy to jump into the conduction band, as illustrated in Fig. 3.1 (b), resulting in the generation of free electrons. In semiconductors, free carriers are exclusively created through the process of electron-hole pair generation described above, following the absorption of laser light in the so-called "photon excitation mode" [98]. In one-photon absorption a single photon carries enough energy to excite an electron from a low to a high-energy state, as described by the following expression.

$$E = \frac{hc}{\lambda} \tag{3.1}$$

where E is the photon energy, h is the Planck's constant, c is the speed of light and λ is the associated wavelength. This formula shows that shorter (blue) wavelengths correspond to greater

photon energies. Ultraviolet radiation (λ = 400 nm, photon energy 3.1 eV) is a good candidate in exciting free carriers in a ZnTe crystal by providing sufficient photon energy, thus, the photo-excited free carrier layer can be induced on the ZnTe surface as a conductive mask to shield THz radiation, in turn working as a virtual blade. This thin conductive mask has a thickness orders of magnitude smaller that the THz wavelength, i.e. below hundred nanometers (i.e. in the scale of the skin-depth of ZnTe at 400 nm). The skin-depth or penetration depth, δ_p, is the depth below the surface of the conductor at which the optical intensity is reduced by a factor of $1/e$ (about 0.37) of its surface value [99].

$$\delta_p = \frac{1}{\sqrt{2\omega\mu_0\sigma}} = \frac{1}{\alpha} \tag{3.2}$$

where σ is the conductivity of the material (Ω^{-1} m^{-1}), ω is the angular frequency of the optical wave (rad.), μ_0 is the permeability of free space (H m^{-1}) and α is the absorption coefficient (m^{-1}).

In order to investigate the influence of the photo-excited free carriers layer on the transmission of a THz source through the surface of our ZnTe crystal, we extract and compare the spectral properties of the reference waveform with the signal waveform, where the reference waveform is referred as the THz waveform propagating through the ZnTe crystal when no photo-excitation is present, whereas the signal waveform is referred as the THz waveform transmitted through the photo-excited layer. The reference spectrum, $A_R(\omega)e^{-i\phi_R(\omega)}$, and the signal spectrum, $A_S(\omega)e^{-i\phi_S(\omega)}$, can be obtained by simply computing the Fourier transform of both the reference and signal waveforms, respectively. Here:

$$\alpha = \frac{1}{d}\ln\frac{A_R}{A_S} \tag{3.3}$$

where α is the absorption coefficient, n is the refractive index, d is the thickness of the photo-excited layer and finally c is the speed of light in vacuum [16].

3.2 Grating-patterned sub-wavelength terahertz source

In the previous chapter, we discussed the characterization of a non-paraxial sub-λ THz emission as a tightly focalized and highly localized source. In this chapter, we not only investigate the

proposed AOKE technique on a Gaussian-shaped super-λ THz source, but we also test the characterization technique on a grating-patterned sub-λ THz source, in order to test the practical reach of the proposed AOKE technique on various THz sources with different sizes and shapes. We made use of a Fresnel biprism to generate the grating-patterned sub-λ THz emission. A Fresnel biprism is able to form non-diffraction fringes when it is illuminated by a coherent plane wave. In other words, the grating-patterned THz source is generated by projecting such non-diffractive fringes onto the ZnTe generation crystal. Figure 3.2 shows a cross-sectional view of the Fresnel biprism featured by a refractive index n, a refractive angle θ_r, and a maximum thickness d, where d is (sufficiently) smaller than the observation distance. The z axis is defined as the original propagation direction of a collimated beam, while the x axis is defined along the wedge angle direction vertical to the z axis on the plane. A Fresnel biprism with an axial symmetrical structure and a rectangle aperture has been considered. The Fresnel biprism is illuminated by a monochromic plane wave propagating in the z direction, orthogonally to its input plane. The plane wave is then divided into two coherence waves by the thin biprism. According to Snell's law, these two waves are deflected toward the x and $-x$ directions, respectively.

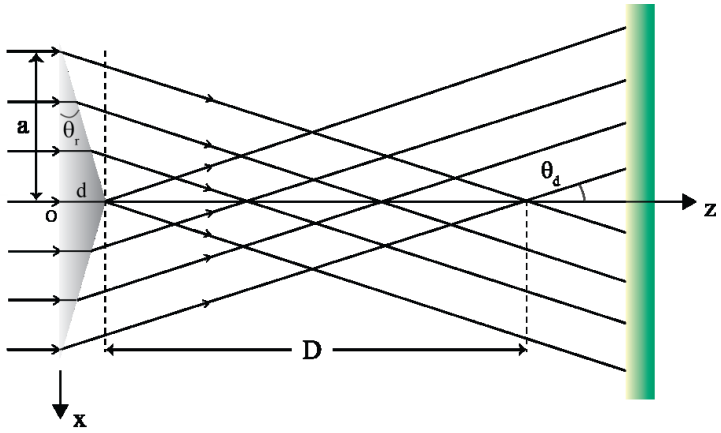

Figure 3.2 Geometric optics path induced by a thin biprism and the relevant notations.

When the refractive angle, θ_r, is small enough, the deflected angle can be simplified as

$$\theta_d = (n-1)\theta_r \tag{3.4}$$

where n is refractive index of the biprism material. The sample (green object in Fig. 3.2) must be located within the length of the maximum focal segment, D, along the z axis (expressed as below).

$$D = a(\cot\theta_d - \tan\theta_r) \tag{3.5}$$

When the sample is located at any plane $z < D$, we obtain the intensity distribution

$$I(x, y, z_1) = 2\{1 + \cos[2k(n-1)\theta_r x]\} \tag{3.6}$$

where $k = 2\pi/\lambda$ is the propagation constant. The spacing of the non-diffractive fringes at the observation plane can be calculated from Eq. (3.7) [100],

$$d_p = \frac{\lambda}{2\theta_d} = \frac{\lambda}{2(n-1)\theta_r} \tag{3.7}$$

In our experiment, a Fresnel biprism with a particular refractive angle and refractive index is mounted prior to the ZnTe generation crystal at the optimum distance within the length of the maximum focal segment, D, so that the non-diffractive fringes are shined onto the ZnTe to generate a grating-patterned sub-λ THz source.

3.3 Experimental setup

The experimental setup is sketched, in its main elements, in Fig. 3.3 (a): THz pulses are generated through OR of by way of the femtosecond optical pulses [32] generated by a Ti:sapphire regenerative amplifier (Spectra-Physics *Spitfire*). This source emits a train of 120 fs pulses with their optical spectrum centered at λ = 800 nm, featured by a repetition rate of 1 kHz. The input beam is split into three lines, i.e. the optical pump line (*pump,o*), the optical probe line (*probe,o*) and the ultraviolet (UV, at 400 nm) pump line (*pump,UV*). In the *pump,o* line, the pulse train of average power 200 mW illuminates a 20μm-thick free standing <110> ZnTe crystal, generating the THz output. Remarkably, the thickness of the generation crystal is much smaller than the lower wavelength limit of the emitted THz power spectrum (typically for a ZnTe source λ_{min} > 200 μm at -3 dB).

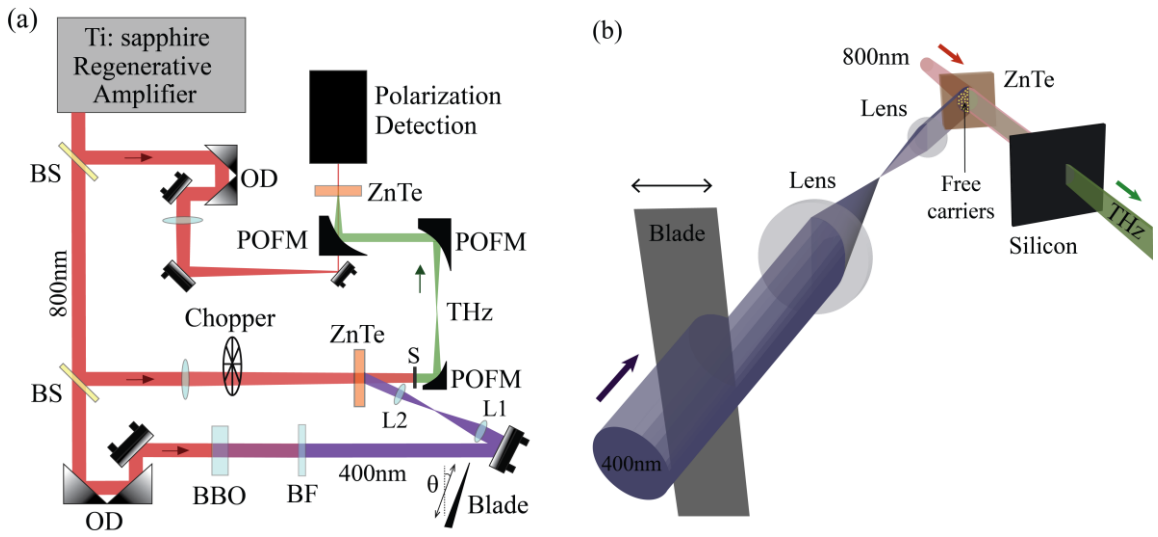

Figure 3.3 **(a) Experimental setup (BS: beam splitter, OD: optical delay, BF: bandpass filter, POFM: parabolic off-axis mirror, L1 & L2: lenses, S: silicon, WP: Wollaston prism); (b) free carriers induced by UV pulses in a blade-shaped area.**

A properly designed imaging system consisting of three parabolic mirrors reconstructs the Fourier's plane of the crystal emitting-surface onto a second ZnTe crystal of thickness 3 mm, exploited to implement a THz EO detection stage. The field is sampled at the center of the Fourier plane, thus returning (by definition) the average field profile (not the power!) in the source plane. Counter propagating UV femtosecond pulses (λ = 400 nm, photon energy = 3.1 eV) are exploited to induce a photo-carrier layer via single photon absorption in proximity of the output surface of the THz-emitting ZnTe crystal. Those pulses are generated through a type-I frequency doubling process of the 800 nm source in a 0.5mm-thick BBO crystal. A bandpass filter centered at 400 nm is exploited to isolate the second harmonic radiation. An imaging system consisting of the lenses L_1 and L_2 projects the transmission image of a blade onto the THz generation crystal using the produced UV light. The position of the boundary of the optical-induced conductive layer (Fig. 3.3 (b)), i.e. the knife-edge, is controlled by translating the blade. This thin conductive mask has a thickness order of magnitudes smaller that the THz wavelength, below hundred of nanometers (i.e. in the scale of the skin-depth of ZnTe at 400 nm). In addition it is positioned at a sub-λ distance with respect to the generating sections within the crystal volume.

It is important to stress here that both these conditions are required for the sub-λ profiling of the electromagnetic sources [101]. The synchronization of the free carrier generation and associated THz pulse is implemented via a tunable delay acting on the UV pump line. The THz time-domain waveforms are collected as the KE moves along the x_0-coordinate by translating the real blade. The experiments were performed under a dry nitrogen atmosphere in order to eliminate the typical THz ringing induced by water vapour. From now on in this chapter, x_0 denotes the blade position, while x denotes the coordinate on the generation crystal.

3.4 Experimental results

Figure 3.4 illustrates the detected THz wave peak for the ZnTe surface pumped by the UV radiation (fluence ≈ 330 μJ/cm^2), corresponding to a UV pump energy limited to 95 μJ - in order to prevent optical damage of the ZnTe crystal, while maximizing photo-carrier generation. The red plot shows the THz peak field against the delay between the UV pump and the THz pulse, $t_{pump,UV}$. Approximating the photo-excited region as a steep-wall metal layer, the dark grey plot shows the estimated exponential absorption, i.e. the product between the effective layer thickness d and its absorption coefficient α, estimated as $\alpha d = \ln (A_R/A_S)$, where A_R is the reference THz field and A_s is the signal detected after propagation through the layer [16]. The maximum attenuation is reached for a delay exceeding 6 ps, with approximately 85% of the total THz energy scattered back by the free carriers. In the inset, the peak field plotted for a maximum delay of 140 ps points out to a carrier recombination time within the time scale of 100 ps, consistent with the excitation of a very high photo-carrier population in the conduction band. To highlight the effect of the carrier temporal dynamics, AOKE measurements have been taken at several UV pump delay ($t_{pump,UV}$ = 1 ps, 3 ps, 5 ps, 6 ps, 7 ps, 8 ps, 10 ps and 15 ps), indicated by arrows in Fig. 3.4.

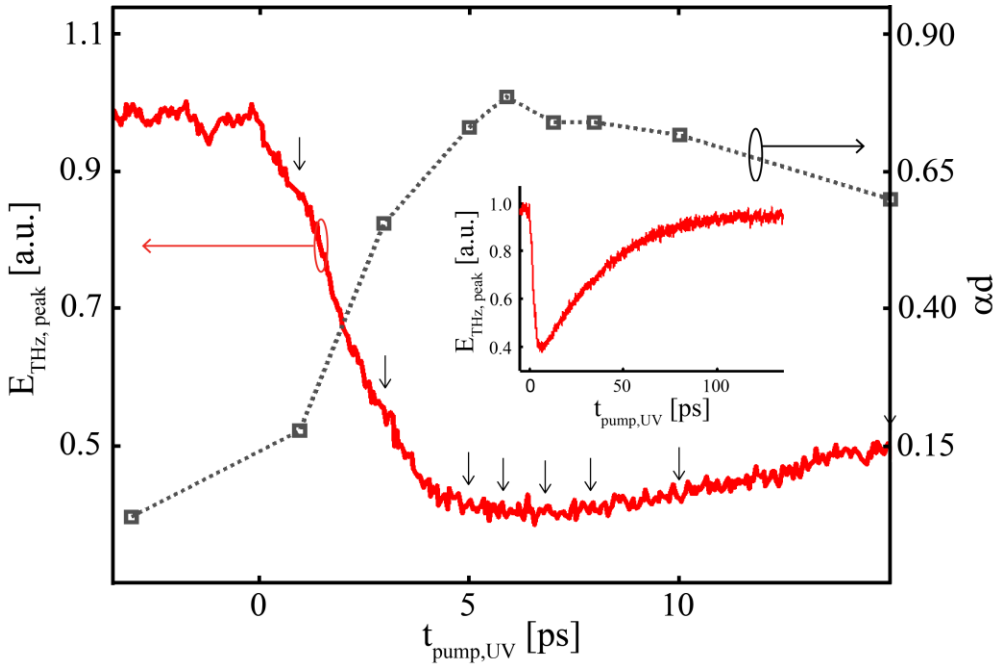

Figure 3.4 **(Red) Peak-THz field vs. the delay $t_{pump,UV}$ between the UV pump pulse and the THz pulse (for positive values the UV pump impinges before the THz pulse). In the inset, the same plot is presented in a much larger $t_{pump,UV}$ window, highlighting a typical carrier recombination time within the 100 ps scale. In dotted Grey, a simple estimation of the (exponential) absorption is calculated from the field decay. The arrows in the plot indicate the delays for which the KE measurement has been performed.**

Experimental results at each pump delay are plotted in Fig. 3.5. The set of data plotted in Fig. 3.5 (a) illustrates the dependence of THz absorption from the UV pump fluence. The AOKE measurement performed for a UV pump with fluence ≈ 330 μJ/cm^2, is shown in Fig. 3.5 (b) where the THz power obtained by the integral of the field square over time is plotted versus the blade position. We note that as the THz beam waist is significantly super-λ, the AOKE does not introduce significant changes in the field phase [101] (i.e. the waveform just scales as the beam is clipped by the edge). This is also highlighted by Fig. 3.5 (c) that presents the AOKE resolved around the frequency 1 THz (λ = 300 μm), extracted as the square-root of the THz power spectral density at 1 THz: the curve matches closely the one obtained from the full spectrum, at any tested delay.

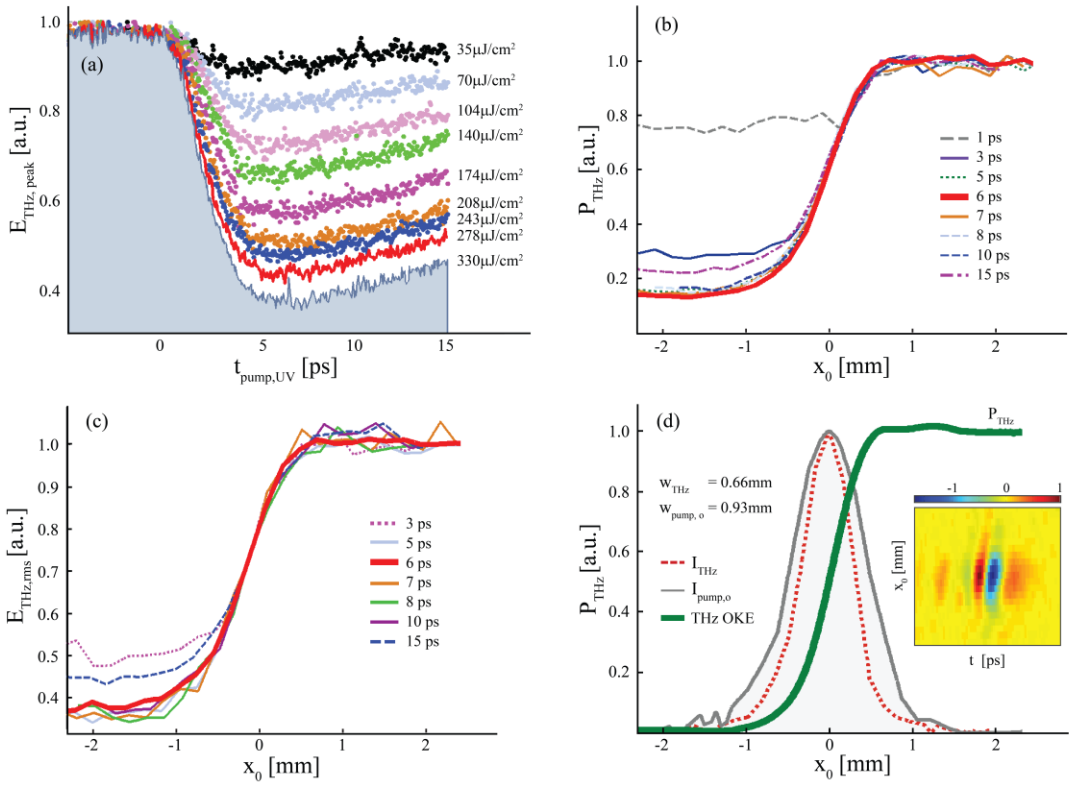

Figure 3.5 **(a) THz peak field vs. UV pump delay at different excitation fluencies; (b) The THz power vs. the blade position; (c) the AOKE measurements resolved at 1 THz are plotted in terms of THz field versus the blade position; (d) the AOKE measurement at a UV pump delay of 6 ps, compared with the beam waist of the optical pump. The inset shows the reconstructed spatio-temporal map.**

The spatial-temporal reconstruction of the THz field, $E_{THz}(x_0, y_0, t)$, is thus obtained (Fig. 3.5 (d)) at a pump delay $t_{pump,UV}$ = 6 ps, under the common hypothesis of a completely separable x and y dependence of the field profile, i.e. $E_{THz}(x_0, y_0, t) = a(x_0, t)\, b(y_0, t)$. The temporal THz waveform collected by the TDS system for each blade delay provides a spatio-temporal map, $EM(x_0, t)$. The THz field, $E_{THz}(x_0, t)$, is evaluated by performing a spatial derivative of the map $EM(x, t)$, as reported in the inset of Fig. 3.5 (d). The THz intensity profile is depicted by the red dotted line in Fig. 3.5 (d). The waist of the THz intensity profile, i.e. in arbitrary units $I_{THz}(x) = \int_{-\infty}^{\infty} |E_{THz}(t)|^2 dt$ (defined as the power at $1/e^2$ of the peak) is found to be w_{THz} = 0.66 mm. This is in perfect agreement with the estimated waist $w_{pump,o}$ = 0.93 mm of the Gaussian pump under the assumption that the beam waist of the generated THz is related to the pump waist by the relation $w_{THz} = w_{pump,o}/\sqrt{2}$ as the THz field is proportional to the optical pump intensity

[72,86,102]. We also validated the AOKE in the characterization of sub-λ THz sources, and especially at the THz source plane. A pump illumination pattern consisting of narrow bright fringes is generated by a Fresnel biprism made of BK7 (refractive index 1.51) with the apex angle of 177° (i.e. refractive angle, θ_r = 1.5 deg), mounted in the THz pump beam path, before the ZnTe generation crystal. The fringe spacing, d_p, from the field interference is simply determined by geometrical optics as $d_p = \lambda/[2(n\text{-}1)\theta_r] \approx 30$ μm, where λ is the 800 nm pump wavelength, n is refractive index of the biprism and θ_r is the refractive angle, as shown in Fig. 3.6 (a). Figure 3.6 (a) - (c) illustrate the AOKE measurement applied on the sub-λ modulated THz source and its reconstructed spatio-temporal profile with blade movement steps of 5 μm. Figure 3.6 (c) shows a better resolved acquisition performed using 1 μm blade position steps ranging from 0.5 to 0.7 mm .

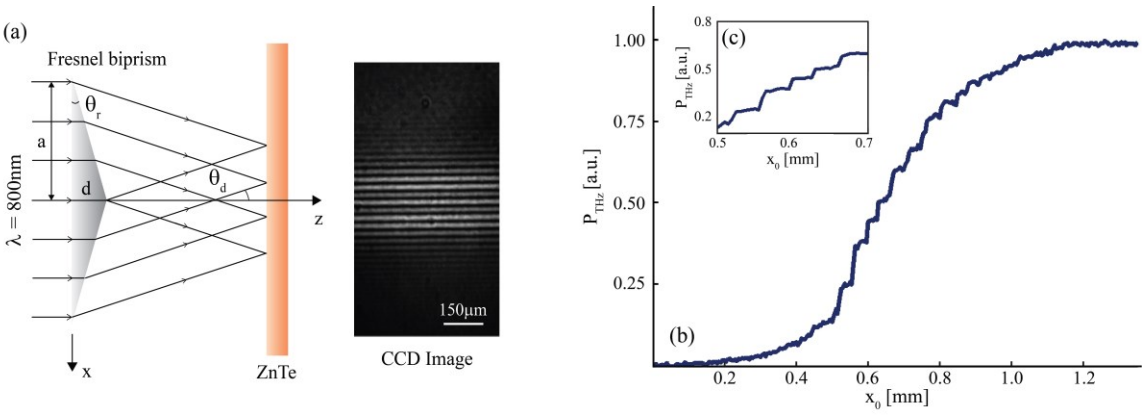

Figure 3.6 **(a) Camera capture of the THz pump profile, consisting of sub-λ fringes of period 30 μm generated by the Fresnel biprism; (b) characterization of the sub-wavelength THz fringes using the proposed AOKE technique; (c) a refined measurement taken with a 1μm blade movement step.**

Figure 3.7 (a) reports the reconstructed THz spatio-temporal field E_{THz} (x_0, t) evaluated as the spatial derivative of the map, EM (x_0, t), extracted by the time resolved AOKE experimental measurement on the sub-λ THz source. It shows that the THz fringes steps are imaged with an estimated resolution in the scale of 10 μm, which is indeed matching the diffraction limit of the telescope used to project the blade when a 400 nm pump is used. This result is compared in Fig. 3.7 (b) with the numerical prediction of the expected THz field distribution at the clipping section for a given optical pump profile (see Appendix 6.3 for details).

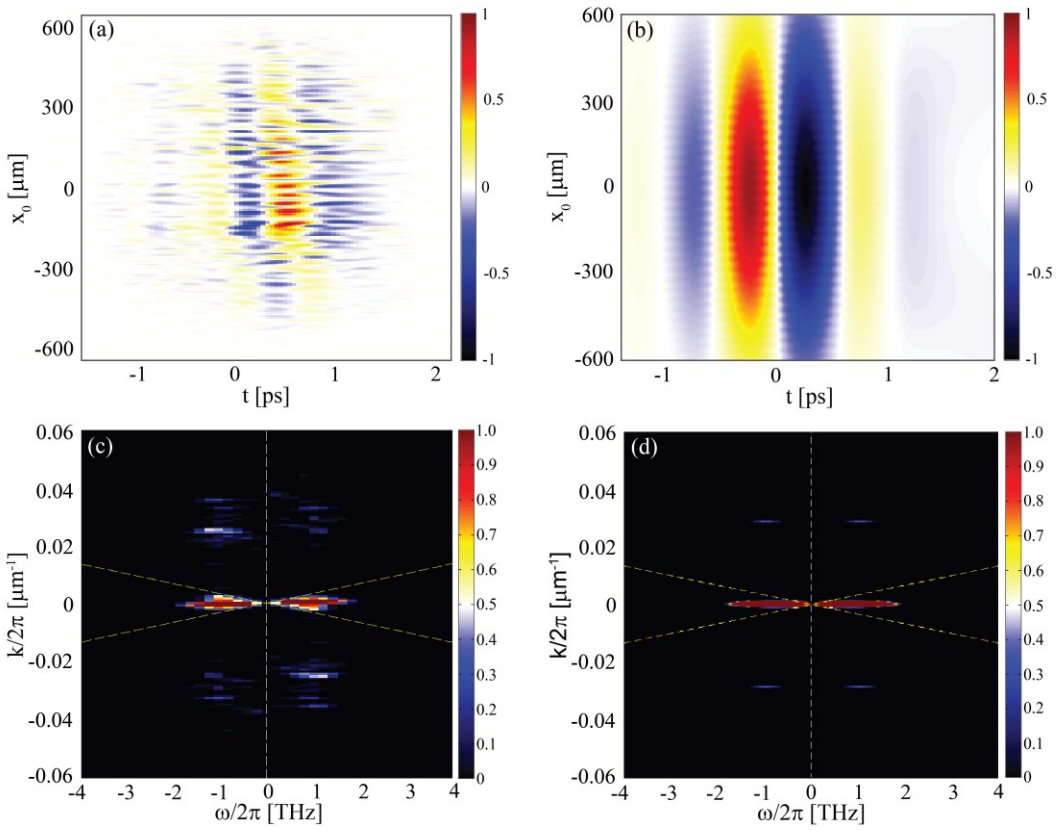

Figure 3.7 **THz field retrieved in space-time and in the transformed space. (a) Reconstructed spatio-temporal profile of the experimentally investigated grating-patterned sub-λ THz source and (b) the corresponding numerical finding. (c) Experimental spatio-temporal spectra obtained (a) in the spatio-temporal Fourier's space and (d) from the numerically predicted output spatio-temporal spectrum.**

In the experiment, optical blade translation increments of 5 μm were considered. A weak sub-λ modulation over the THz pulse is expected on the top of a super-λ profile (Fig. 3.7 (b)). The diffraction limit imposes that such modulation rapidly disappears in the THz propagation coordinate and it can be captured only by clipping the field at sub-λ distances from the generation plane. The reconstructed THz pulse in Fig. 3.7 (a) shows a strong contribution of the sub-λ fringes, indicating that the data are collected in proximity of the generation plane. This is particularly evident when the reconstructed field in the transformed space $E^{(R)}(k, \omega)$ is observed - as in Fig. 3.7 (c) - along with the calculated incident field $E^{(i)}(k, \omega)$ (see Appendix 6.3 for details). In the diagrams, we report the loci $k = \pm\omega/c$, which discriminate the super-λ ($|k| < |\omega|/c$) from the sub-λ regime ($|k| > |\omega|/c$). The strongly visible sub-λ components (corresponding to

$k/2\pi$ = 0.025 μm^{-1} and $\omega/2\pi$ = 1 THz) carry the information on the periodic modulation associated to the THz spatial profile. We remark that there is a strong asymmetry in the reconstructed THz field profile and a much stronger contribution of the sub-λ fringe features with respect to those predicted by a numerical model accounting for the sub-λ THz modulation. This is expected for a KE+TDS system (see Appendix 6.3 for details) that imposes a transfer function $\breve{T}(k_x, \omega)$, between the incident and the reconstructed fields in the Fourier transformed space:

$$\breve{E}^{(R)}(k_x, \omega) \propto \breve{T}(k_x, \omega)\breve{E}^{(i)}(k_x, \omega) \tag{3.8}$$

$$\breve{T}(k_x, \omega) \equiv \begin{cases} \sqrt{1 + \frac{ck_x}{\omega}} & \text{for } k_x > -\frac{\omega}{c} \\ 0 & \text{for } k_x < -\frac{\omega}{c} \end{cases} \tag{3.9}$$

where c is the speed of light. Such function cuts the superluminal components corresponding to the region bounded by the straight lines $k_x = -\omega/c$ and $\omega = 0$, but strongly enhances the features in the region between $k_x = \omega/c$ and $\omega = 0$. As shown in the work of Peccianti and co-worker, the KE+TDS system is particularly suitable to detect weak sub-λ details as far as the blade is positioned in close proximity to the sub-λ features to be characterized [101]. The proposed AOKE technique satisfies this stringent condition and allows the mapping of the sub-λ field inside the high refractive index medium where the THz is generated or where the modulation is imposed.

3.5 Conclusion

In conclusion, we demonstrate the possibility of a novel, all-optical, ultra-thin-thickness knife-edge as an effective and promising characterization technique for imaging sub-λ features in the terahertz spectral region. Specifically, our setting is directly applicable to field-profiling inside the generation crystal. We believe that this approach could readily lead, as a next step, to the realization of reconfigurable (active) metamaterials or other structures directly imprinted on the generating crystal.

4 MICRO-SLIT BASED COHERENT DETECTION OF TERAHERTZ PULSES IN BIASED, SOLID STATE MEDIA

4.1 Another alternative for THz coherent detection

Terahertz time-domain spectroscopy (THz-TDS) has recently emerged as a distinguished method for spectroscopy because it offers the coherent detection features which enables the simultaneous measurement of the amplitude and phase of a pulsed THz wave [103]. Photoconductive antennas [31] and EO crystals [33,54] are widely used as the detectors for coherently measuring THz waves in THz-TDS setups, yet PCA detection and EO sampling suffer from a number of limitations. It is well known that the lifetime of photo carriers in the semiconducting materials at the basis of a PCA detector antenna limit the temporal resolution achievable and hence the detection bandwidth.

Meanwhile, the experiments discussed in previous chapters were conducted by utilizing a ZnTe crystal as the detection medium, where the THz emission was characterized by performing EO sampling (taking advantage of the electro-optic effect in the crystal). The THz field induces an instantaneous birefringence in the EO medium, which is readily probed with a second near-infrared beam, initially split from the pump beam.

The linearly polarized probe beam is modified to an elliptical polarization through the EO process while THz emission propagates through the detection crystal, measured using a quarter-waveplate ($\lambda/4$), a Wollaston prism, and two balanced photodiodes. The quarter-wave plate biases the polarization state of the probe beam, whereas the Wollaston prism functions as an analyzer to split the probe beam into its s and p polarization components. A pair of balanced photodiode is used to measure a difference in the s and p polarization components when a THz electric field is present.

However, the detection efficiency and the bandwidth of the EO crystals are not only restricted by the absorption and phase mismatch but also perturbed by the étalon reflections from the crystal. Besides, THz fields of several hundred kilovolts per centimeter can induce phase

delays larger than π in an optical probe beam, when passing through the millimeter-thick crystal. In this case, a thin detection crystal is desirable because such large phase delays over-rotate the polarization of the optical probe beam, causing the EO sampling to deviate from the linear response, and consequently a distortion of the detected waveform to occur. For this reason, in this chapter, we would like to propose a device other than a PCA detector and/or an EO crystal as an alternative choice to standard detection schemes for THz characterization.

Here, we performed the time-resolved characterization of single-cycle THz pulses exploiting electric field induced second harmonic generation (EFISH) in an electrically biased thin silica (SiO_2) sample. Coherent THz electric field traces are indeed recorded making use of the terahertz field-induced second harmonic generation (TFISH) when a potential of up to few thousands volts is applied between an infinite slit made of a pair of gold (Au) electrodes and buried in SiO_2.

Regarding to the development of TFISH, Nahata and Heinz demonstrated the measurement of THz waveforms by means of optical second harmonic generation (SHG) through the well-known electric-field-induced second-harmonic generation (EFISH) in centrosymmetric media [90]. Furthermore, this method has been later used in measuring the liquid dynamics using a THz pump-optical probe setup [105]. To the best of our knowledge, up to now, coherent detection techniques relying on TFISH have mostly been demonstrated employing gasses as the nonlinear media, as shown for air-breakdown-coherent-detection [106] and air-biased-coherent-detection (ABCD) [107].

The ABCD technique, thanks to the low dispersion of air, can record THz fields with extremely large bandwidth (> 20 THz), yet cannot be easily miniaturized to the extent of few centimeters or less. Furthermore, it typically requires kV sources, since the detection signal to noise ratio (SNR) depends on the amplitude of the bias field [108]:

$$SNR = \frac{2I_{\omega}E_{THz}E_{bias}}{\delta I_{\omega}[(E_{THz})^2+(E_{bias})^2+2E_{THz}E_{bias}]} \tag{4.1}$$

and it is limited by the air breakdown voltage. In this chapter, we demonstrated the coherent characterization of THz waves by TFISH in solid state-based devices, consisting of a thin layer of silica biased by a couple of gold electrodes with a gap width in the micron scale. In our case the dimensions of the interaction region can be shrunk down to the millimeter or less where the probe power required for the detection is comparable to the values employed for EO sampling.

4.2 Terahertz field induced second harmonic in micro-slits

One of the symmetry properties of crystals is inversion symmetry. A centrosymmetric medium is one whose potential function, *U*, possesses a degree of symmetry with respect to negative and positive *x* displacements, as shown in Fig. 4.1 (a). In other words, it must be a medium that possesses a center of inversion symmetry.

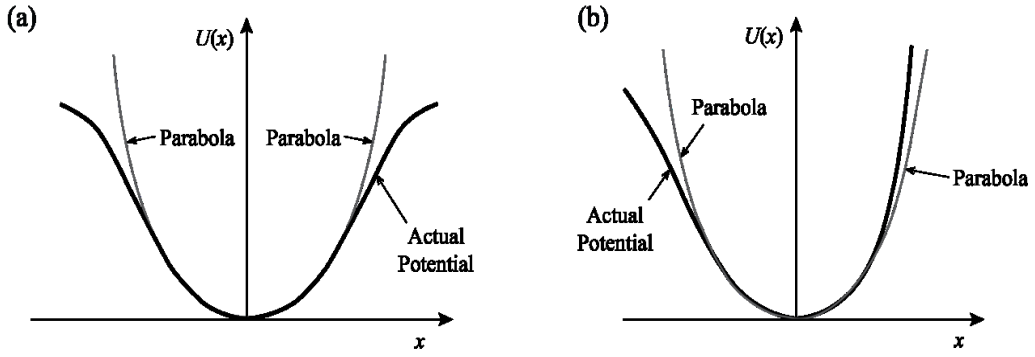

Figure 4.1 **(a) Potential energy function for a centrosymmetric medium. (b) Potential energy function for a noncentrosymmetric medium [34].**

On the contrary, a noncentrosymmetric medium possesses the potential energy function illustrated in Fig. 4.1 (b), containing both even and odd powers along the *x* displacement, showing a characteristic lack of inversion symmetry [34]. In centrosymmetric materials, the $\chi^{(2)}$ nonlinear susceptibility vanishes, therefore the lowest-order change in the refractive index depends quadratically on the strength of the applied DC (or low-frequency) field, which is a third-order contribution to the polarization described by a $\chi^{(3)}$ susceptibility. Consequently, second-order nonlinear optical interactions can occur only in noncentrosymmetric crystals (i.e. crystals that lack of inversion symmetry).

As we previously discussed, the detection of THz radiation is widely performed based on the second-order nonlinear optical effect. Several noncentrosymmetric materials, such as ZnTe, $LiNbO_3$, GaAs etc, have been developed and can be employed to measure THz pulses, making use of their high second-order nonlinear optical susceptibility. Apparently, centrosymmetric media cannot be utilized in THz detection due to their zero $\chi^{(2)}$. This limitation can be overcame employing the well-known electric field-induced second harmonic generation (EFISH) sampling

technique, in which the inversion symmetry of a centrosymmetric medium is broken by an external AC bias, i.e. a local oscillator. This creates a broader spectrum of possibilities in terms of choice of materials for THz coherent detection.

This familiar concept is used in terahertz field induced second harmonic generation (TFISH). TFISH can be understood as an extension of DC-electric field induced second harmonic generation (DC-EFISH). It results from a four-wave-mixing process as described below [104,105]:

$$E_{2\omega} \propto \chi^{(3)} E_\omega E_\omega E_{THz} \propto \chi^{(3)} I_\omega E_{THz} \tag{4.2}$$

where $\chi^{(3)}$ is the third-order susceptibility of the nonlinear medium, E_ω is the optical electric field and E_{THz} is THz electric field. We typically loose the phase information of the THz wave since the photomultiplier tube (PMT) detector only measures the second harmonic (SH) intensity. The measurement will be linearly proportional to the THz field if the superposition with a local oscillator is performed, which would turn the measurement into a coherent measurement. This concept can be expressed mathematically as:

$$\begin{aligned} I_{2\omega}^{measured} &= |E_{2\omega}|^2 = |E_{2\omega}^{THz} + E_{2\omega}^{local}|^2 \\ &= |E_{2\omega}^{THz}|^2 + |E_{2\omega}^{local}|^2 + 2E_{2\omega}^{THz} E_{2\omega}^{local} \cos(\phi) \end{aligned} \tag{4.3}$$

in which $E_{2\omega}^{THz}$ is the SH signal obtained by focusing the THz pulse collinearly with the optical probe beam, $E_{2\omega}^{local}$ is the SH signal rising from the local oscillator and ϕ is the phase difference between the local oscillator and the THz wave induced SH wave. The first term in the right side of Eq. (4.3) is proportional to the intensity of the THz wave. The second term occurs in the presence of the local oscillator. In our case, the local oscillator is made of a pair of electrodes deposited on a micro-slit device. An AC bias field (square wave) synchronized with the laser repetition rate is then applied to the metal pads. The third contribution is the cross term proportional to the THz field and appears as the coherent one in the THz-TDS measurements. While $\vec{E}_{2\omega}^{local}$ exists in the measurement, it interferes with $\vec{E}_{2\omega}^{THz}$. This interaction enable us to control the carrier-envelope phase of $\vec{E}_{2\omega}^{THz}$ from 0 to π by switching the direction of the bias field, meaning that the cross term in Eq. (4.4) possesses a fixed magnitude with alternating sign.

For this reason, the time-averaging notation can be cancelled out and the resulting expressions can be addressed as below by taking into account the bias field, E_{bias}.

$$E_{2\omega}^{THz} \propto \chi^{(3)} I_{\omega} E_{THz}$$

$$E_{2\omega}^{local} \propto \chi^{(3)} I_{\omega} E_{bias} \tag{4.4}$$

Substituting Eq. (4.4) into Eq. (4.3), we can then write the following expression.

$$I_{2\omega}^{measured} \propto (\chi^{(3)} I_{\omega})^2 [E_{THz}^2 + E_{bias}^2 \pm 2E_{THz}E_{bias}] \tag{4.5}$$

Recently, a metallic slit or an array of metallic slits have been widely employed for optical transmission enhancement [109-111]. The work opens the door for metallic slits to a variety of application, such as, light beaming [112], quarter-wave retarder [113], light funnelling [114] and near-field imaging across a broad frequency range [66]. Here, we explored another application of such metallic slit in measuring THz emission, instead of traditional field enhancement. In particular, we showed that an infinitely elongated metallic micro-slit filled with SiO_2 can be used as an effective detector for THz coherent detection by means of SHG. In our experiments, the local oscillator, $E_{2\omega}^{local}$ is dependent on the AC field-induced SHG in in a micro-slit deposited on a SiO_2 substrate. When the AC bias is high enough, it starts to generate 2ω components arising from the change in the polarizability and the orientation of the molecules of SiO_2 under the influence of the electric field of the probe beam and the applied bias field, as shown in Fig. 4.2 [115].

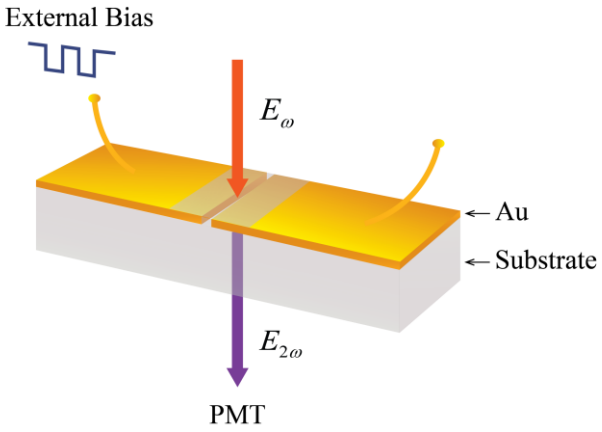

Figure 4.2 **Electric field-induced second harmonic when the external bias break the inversion symmetry of silica in the absence of a THz pulse.**

4.3 Micro-slit fabrication

The infinitely elongated metallic slit with a gap width of 30 μm was prepared by depositing two separate coplanar gold (Au) layers onto a 1mm-thick UV graded fused silica substrate which was previously cleaned with Nanostrip prior to the metal deposition (Fig. 4.3). Fused silica is one of the most manufactured materials and exhibits a higher transparency in the ultraviolet transmission with respect to most other common glasses. As such, it is an ideal candidate for applications in the ultraviolet spectral region. A 100nm-thick Au layer is deposited together with a very thin adhesive layer of 30nm-thick chromium (Cr) at both the bottom and the top of the sample, in order to have Au electrodes on both sides of the SiO_2 substrate.

Ultraviolet lithography patterning has been used to define the electrodes, where a resist (S1813) was spin-coated at 2000 rpm and baked at 115 °C for 2 minutes, leading to a layer of ~1.5 μm thickness. The resist was exposed to a Laser Writer (DWL 66fs from Heidelberg) and developed to define the electrode pattern into the resist. The deposited Au and Cr were etched by way of a chemical wet process, followed by PECVD to grow a 30μm-thick SiO_2 over the electrodes gap under an environment of SiH_4 and N_2O precursor gases at 390°C. As a result, the Au slit is filled with deposited SiO_2. Two silicon plates were used to cover the rest of the sample during the PECVD process so that only the central part of the sample was exposed to the deposition process. The Au electrodes are connected to a bipolar high voltage modulator. Four isolated Au slit samples were fabricated on the fused silica substrate to avoid damage on the sample induced by the dielectric breakdown field.

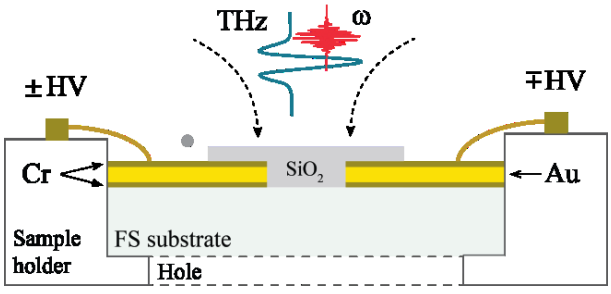

Figure 4.3 **Schematic drawing of the layer structure of a metallic slit sample deposited on the UV graded fused silica substrate by a PECVD process (HV: high voltage; Cr: chromium; Au: gold; FS: fused silica; THz: terahertz pulse; ω: probe pulse). Note that the drawing is not in scale.**

4.4 Experimental setup

The measurement is taken using the THz-TDS setup shown in Fig. 4.4 (a). The input delivered by a Ti:sapphire regenerative amplifier with a center wavelength of 800 nm, 120 fs pulse duration, and 1 kHz repetition rate is used in the experiment. The linearly polarized (*x*-polarized in our case) input pulse from the regenerative amplifier is split into a pump and a probe for THz generation and detection, respectively. THz radiation is produced via OR from a ZnTe crystal and further focused on the metallic slit for detection after it propagates through several parabolic off-axis mirrors.

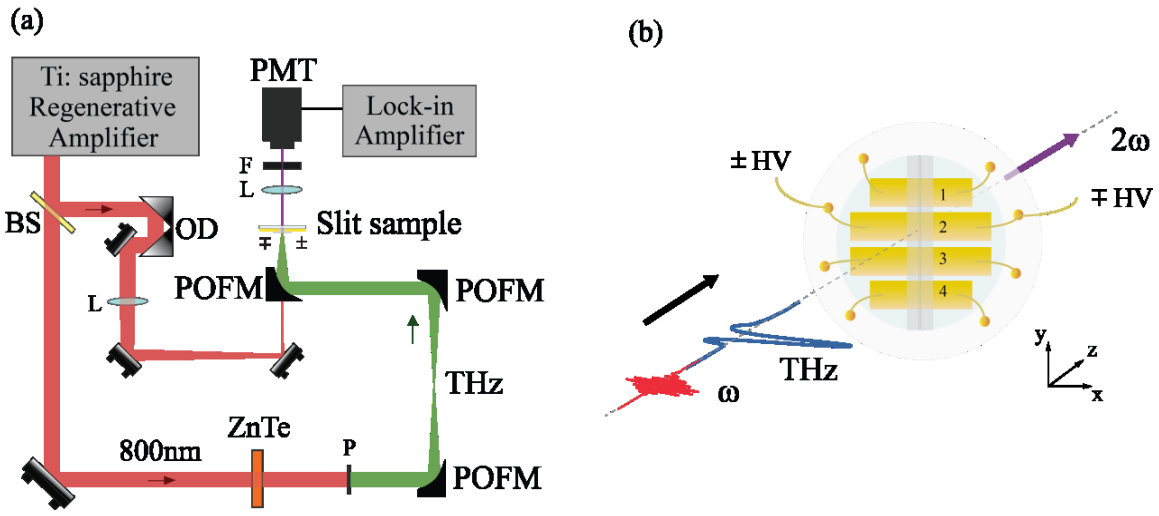

Figure 4.4 **(a) Experimental setup (BS: beam splitter, OD: optical delay, L: lens, POFM: parabolic off-axis mirror, ZnTe: zinc telluride, P: polyethylene, F: filter, PMT: photomultiplier tube). (b) The *x*-polarized optical probe pulse and THz pulse propagate through the metallic slit along the *z* axis (FS: fused silica, HV: high voltage).**

By substituting the detection ZnTe crystal with our micro-slit device and exchanging the balanced photodiodes with a photomultiplier tube it is possible to record the THz signal via the proposed technique. The probe beam (featured by an intensity of 350 W/cm^2) is focused using a 100 mm lens through a hole on the final parabolic mirror in the THz beam path, so that the co-propagating THz and probe beams are spatially overlapped into the same spot where the THz field induces a SH pulse through the process of four-wave-mixing on the SiO_2-filled slit. The slit is located across the focal spot. A bias field of ±2.5 kV, provided by a high voltage modulator delivering a bipolar square wave synchronized with the laser repetition rate, is applied between

the electrodes. The SH beam is filtered by a bandpass filter centered at 400 nm and is then detected by a PMT. The signal collected by the PMT is measured by a lock-in amplifier synchronized with a 500 Hz bias modulation frequency. The polarizations of the optical probe pulse and THz pulse are parallel to each other, where the slit's long side is parallel to the *y*-direction as shown in Fig. 4.4 (b) (TM polarization to the slit). While we scan the relative delay between the THz wave and the probe beam, the SH signal of the probe beam is observed when the probe beam and the THz wave are overlapped temporally. We measure the SH signal intensity as a function of the temporal delay between the THz wave and the probe beam.

4.5 Experimental results

Figure 4.5 (a) shows the coherently detected THz waveform. We note that, if the AC bias field is not applied, it is possible to measure the incoherent interaction signal. To that end, the lock-in amplifier is triggered at the laser repetition rate and we recorded the trace shown in Fig. 4.5 (b). Such trace is proportional to the intensity of the THz field rather than to the electric field squared. This is a consequence of the mismatch of two four-wave mixing processes that are responsible for the TFISH interaction (see e.g. [116]).

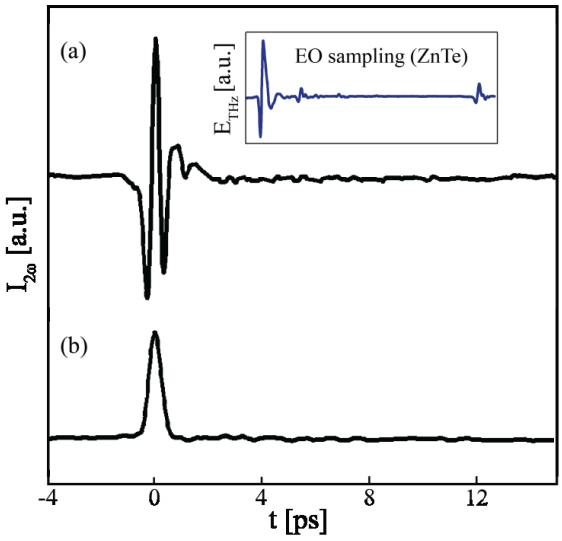

Figure 4.5 **Comparison of THz time-domain waveforms measured (a) with and (b) without AC bias field. The upper inset shows the internal crystal reflections, accompanied by the reflections between the generation and detection crystals in the EO sampling measurement.**

The measured waveforms at different AC biases are illustrated in Fig. 4.6 (a). The signal increases with higher AC bias fields indicating that the TFISH signal is amplified through the cross term of the stronger AC field-induced SHG (third term of Eq. 4.3). However, a degradation of the SH signal is observed when the AC bias field exceeds ±2.5 kV, which in turn reduces both the dynamic range (DR) (red line in Fig. 4.6 (b)) and the SNR (blue line in Fig. 4.6 (b)). Typically, the noise in the detected signal is shot-type noise, proportional to the optical average power, to the dark noise of the PMT and to the noise resulting from the electronics. Concerning the degradation of the DR and SNR observed at higher AC bias fields, the origin and mechanism behind this particular phenomenon is still under investigation. Figure 4.6 (c) shows the corresponding amplitude spectra of detected THz pulse at various AC bias field.

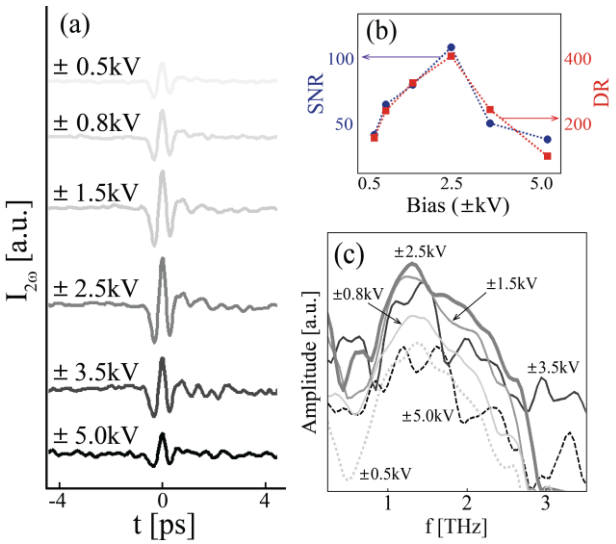

Figure 4.6 **(a) Dependence of the measured SH intensity on the different AC bias fields with fixed probe intensity 350 W/cm^2 measured in dry nitrogen gas. (b) Corresponding dynamic range (red line) and signal-to-noise ratio (blue line). (c) Amplitude spectra extracted from the time-domain waveforms.**

We further tested the proposed novel detection scheme against the well-known *Gouy* phase shift where a polarity reversal is expected. The Au slit sample was mounted on a translation stage in the *x*, *y* and *z* axis, in order to probe the THz wave along its focal region, by translating the slit at different *z* positions along the beam propagation direction (Fig. 4.7). A significant polarity reversal is observed along the detection region due to the *Gouy* effect, which introduces

an additional π phase shift for a focused beam as compared to a plane wave [117-119]. The THz waveform is flipped at the *z* position of 4.5 mm, where the SH signal has opposite phase, right after the beam passes through the focal point.

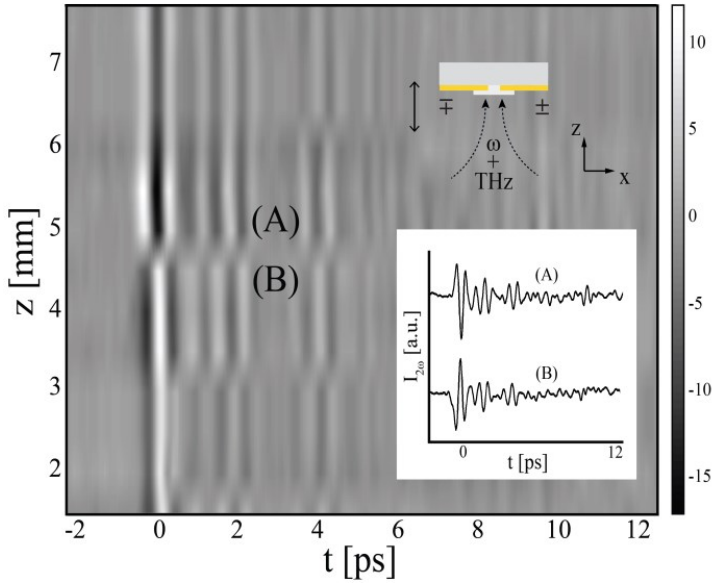

Figure 4.7 **Spatial evolution of the pulse shape along the *z* axis from *z* = 1 mm before the focus, through the focus (center), and then at z = 7.5 mm. A polarity reversal of the detected SH in the positions (A) and (B) - due to the Gouy phase shift- is observed, following measurements in the ambient air environment.**

4.6 Conclusion

In conclusions, we characterized the THz pulse by means of SH using an ultrathin SiO_2 layer with thickness in the sub-λ scale, deposited within a Au slit. The demonstrated technique not only avoids the issue of phase mismatching in thick crystals as well as strong Fabry-Pérot reflections in the thin EO crystal, but also eliminates the external optical reflections taking place in the propagation path between the generation and the detection crystals. A lower probe energy with respect to standard ABCD is required for the detection. Therefore, measurements based on our technique can be easily implemented using the standard oscillators which are currently among the most widely used laser systems in photonics research.

5 CONCLUSIONS

The aim of this work has been the realization of novel approaches for the precise characterization of THz emission, which is essential for improving and manipulating THz sources in real world applications.

The knife-edge technique is a well-established characterization technique and it is widely used in laser beam profiling. In this dissertation, we addressed the important criterions to be considered when the THz field is characterized using the standard KE technique. To validate the standard KE technique as a proper method in sub-λ THz source characterization, we first investigated the origin of the inherent aberrations induced by the combination of the KE techniques and EO sampling in a TDS setup. The aberration is observed by resolving the spatio-temporal electric-field profile, where an unexpected asymmetric field distribution is obtained along the spatial coordinate. We addressed this issue by considering the transmission of an electromagnetic field from a perfectly conducting half-plane with the exact Sommerfeld approach. Besides, we have also shown that the standard KE technique introduced an aberration into the spatio-temporal profile, which may eventually restrict the reliability of certain sub-λ imaging protocols based on raster scanning. We note that the aberration is dependent on the distance between the object to be imaged and the THz generation plane. We derived the explicit form of the transfer function of the KE measurement, which allows the retrieval of the original source profile from the measured data.

Despite the development of a transfer function for the exact profile retrieval mentioned above, KE remains a mechanical technique that requires a physical blade at the emission plane of the source, hence we further demonstrated a novel all-optical knife-edge (AOKE) technique to characterize the THz source, which eliminates the usage of a physical blade at a sub-λ distance from the THz generation plane. The proposed AOKE technique relies on the generation of a photo-excited free carrier layer acting as a virtual blade - exactly located on the generation plane and shielding the THz emission. Ultraviolet radiation is employed to project a sharp blade-shaped image on the output facet of the generation crystal, while in turn the photo-excited area blocks the THz emission. Thus, the AOKE measurement can be implemented as a 'remote-based KE' using the virtual blade. This technique is first tested on a super-λ THz source, and is later

applied to the characterization of a grating-patterned sub-λ THz source to validate its practicality for different sizes and shapes. We roughly expect a quadratic dependence between the fringe intensity profile and the THz intensity profile, hence a quite steep increment (respect to the fringe period) induced by each fringe in the AOKE measurement. The corresponding spatio-temporal profile showed that the step pattern of a grating-patterned THz source is assessed with a resolution in the 10 μm scale, matching well with the relevant diffraction limit of the imaging system used to project the blade-shaped image by using ultraviolet radiation.

The characterizations discussed prior to this paragraph were conducted using an EO crystal, i.e. a ZnTe crystal, as the detection crystal. However, THz detection through a EO crystal is usually limited by the absorption and phase mismatch. In addition, it also suffers from the étalon reflections from the crystal. Besides, the fact that a strong THz field gives rise to phase retardations larger than π in the optical probe beam when it propagates through the thick EO crystal draws a strong interest in developing alternative devices to overcome such limitations. Hence, we proposed and demonstrated that the ABCD scheme can be translated in the solid state to detect THz pulses featured by a broad bandwidth. We performed a novel implementation of the ABCD protocol relying on the TFISH in a few micron thick SiO_2 device, by applying an external bias field acting as the local oscillator. In the experiment, the large breakdown voltage and the high nonlinearity of glasses have been exploited to achieve a high SNR detection using a (comparably) weak optical probe.

To the best of our knowledge, this is the first solid-state device for coherent THz detection relying on TFISH and operating over a broad bandwidth. The preliminary results reported in this dissertation were collected by measuring the THz pulse using a single and infinitely long 30 μm slit written in gold and SiO_2. The THz is focused on the detection region, where it is co-propagated with the probe pulse and focused collinearly (spatially and temporally) on the same spot. The results are later compared with the THz pulse measurements performed via EO sampling. A high signal-to-noise ratio of nearly 100 is achieved in the presence of a 2.5 kV external bias. An incoherent interaction signal can be detected in the absence of the external bias. Such signal is proportional to the THz intensity rather than to the THz field squared, which is attributed to the mismatch of the two four-wave-mixing processes that describe the TFISH interaction.

To recap, the work reported in this dissertation firstly provides a mean to perform the exact profile retrieval of a THz sub-λ source using the KE technique combined with the THz-TDS technique. Further, an AOKE technique has been demonstrated to eliminate the need of attaching the physical blade to the emission plane of the THz source, in order to fit practical applications. Finally, we showed that it is possible to perform THz detection by replacing the EO crystal with a very thin SiO_2 layer deposited within an Au slit, where an external bias field is applied. The results reported here give an intriguing perspective in developing new approaches for both THz source and image characterization.

6 APPENDICES

6.1 Common units and their conversion at 1 THz

Frequency: $\nu = 1$ THz = 1000 GHz

Angular frequency: $\omega = 2\pi\nu = 6.28$ THz

Period: $\tau = 1/\nu = 1$ ps

Wavelength: $\lambda = c/\nu = 0.3$ mm = 300 μm

Wavenumber: $\bar{k} = k / 2\pi = 1/\lambda = 33.3$ cm^{-1}

Photon energy: $h\nu = \hbar\omega = 4.14$ meV

Temperature: T = $h\nu / k_B = 48$ K

where c is the speed of light in vacuum, h is Plank's constant, and k_B is Boltzmann's constant [57].

6.2 Diffraction from a metallic half-plane

6.2.1 Definition of the vector potential equations for the KE

We will treat the diffraction problem from a half-plane and define the polarization-dependent transfer function of the KE with the aid of the vector potential **A**. In the (**r**, ω) space, **A** is defined by the relations with the electric field

$$\mathbf{E} = \frac{1}{i\omega\varepsilon_0}(\nabla\nabla\cdot\mathbf{A} + k_0^2\mathbf{A}) \qquad (6.1)$$

where ε_0 is the vacuum dielectric constant and $k_0 = \omega/c$ is the wavenumber in vacuum. The THz field is generated by optical rectification under the hypothesis of weak generation, i.e., the pump is not depleted/modified by the generation itself. In this case, the optical field acts as a pure source for the THz field, proportional to a current source $\mathbf{J}^{(i)}$ (defined in the space z < 0) by way

of the nonlinear second-order tensor. Using the definition in (6.1), the vector potential satisfies the wave equation

$$\nabla^2\mathbf{A} + k_0^2\mathbf{A} = \mathbf{J} \tag{6.2}$$

It is important to note that the vector potential **A** is always parallel to the current source. As it physically represents the optical field, that is paraxial along the propagation coordinate *z*, neither the current $\mathbf{J}^{(i)}$ nor the vector potential $\mathbf{A}^{(i)}$ possess longitudinal components along *z*. Moreover, if the optical beam is *x* (*y*) polarized, we obtain a vector potential that is *x* (*y*) polarized. As discussed previously, the quantity under test is $\breve{\mathbf{E}}^{(i)}(k_x, k_y = 0, z = 0, \omega)$. We can express this quantity in function of the spatial Fourier transform $\breve{\mathbf{A}}^{(i)}(k_x, k_y, z = 0)$ of the vector potential in the plane of the blade, $z = 0$. For $z > 0$ we have

$$\mathbf{A}(x, y, z) = \int \breve{\mathbf{A}}\big(k_x, k_y, z = 0\big) e^{ik_x x + ik_y y + i|z|\sqrt{k_0^2 - k_x^2 - k_y^2}} \frac{dk_x dk_y}{(2\pi)^2} \tag{6.3}$$

Substituting into (2.10) for $z = 0^+$ (the field transmitted at the plane z = 0 is referred with a sign of "+") and $k_y = 0$ (we will omit this dependence for simplicity), we obtain

$$\begin{bmatrix} \breve{E}_x^{(i)}(k_x, \omega) \\ \breve{E}_y^{(i)}(k_x, \omega) \\ \breve{E}_z^{(i)}(k_x, \omega) \end{bmatrix} = \frac{1}{i\omega\varepsilon_0} \begin{bmatrix} (k_0^2 - k_x^2)\breve{A}_x^{(i)}(k_x, \omega) \\ k_0^2 \breve{A}_y^{(i)}(k_x, \omega) \\ -k_x\sqrt{k_0^2 - k_x^2}\breve{A}_x^{(i)}(k_x, \omega) \end{bmatrix} \tag{6.4}$$

Note that if we have a *y*-polarized source, the field on the blade will be *y*-polarized; conversely, for an *x*-polarized source the field will have a zero *y* component. If we can reconstruct $\breve{\mathbf{A}}^{(i)}(k_x, \omega)$, (6.4) will then provide the electric field $\breve{\mathbf{E}}^{(i)}(k_x, \omega)$. We now take into account the quantity measured by the TDS system (2.10) and substitute into (A1). Considering that **A** does not have longitudinal components, we obtain

$$\breve{\mathbf{E}}\big(k_x = 0, k_y = 0, z = 0^+\big) \cdot \hat{\boldsymbol{u}} = -i\omega\eta_0 \breve{\mathbf{A}}\big(k_x = 0, k_y = 0, z = 0^+\big) \cdot \hat{\boldsymbol{u}} \tag{6.5}$$

As discussed in the next sections, the integral of the total vector potential at the output of the blade $z = 0^+$ is

$$\breve{\mathbf{A}}\big(k_x = 0, k_y = 0, z = 0^+\big) \cdot \hat{\boldsymbol{u}} = \mathbf{A}^{(i)}\big(k_x = 0, k_y = 0, z = 0^+\big) \cdot \hat{\boldsymbol{u}}$$

$$-\int \frac{2i}{s_x}\sqrt{1+\frac{cs_x}{\omega}}\breve{\mathbf{A}}^{(i)}\left(s_x, k_y=0, z=0^+\right)\cdot\hat{\boldsymbol{u}}e^{is_x x_0}\frac{ds_x}{2\pi} \quad (6.6)$$

We can substitute (6.6) into (6.5), and differentiate for x_0 and transform back in time, as done for (2.12). This yields:

$$\mathbf{e}_R(x_0,t) \propto \mathrm{Re}\iint_{-\infty}^{\infty} -i\omega\eta_0\sqrt{1+\frac{csk_x}{\omega}}\breve{\mathbf{A}}^{(i)}\times(k_x,\omega)e^{is_x x_0-i\omega t}\frac{dk_x d\omega}{(2\pi)^2} \quad (6.7)$$

Following the same considerations applied previously on the radical function, and addressing two different KE measurements for positive and negative x_0, we can reconstruct the two functions

$$\breve{\mathbf{A}}_{\pm}^{(i)}(k_x,\omega)\cdot\hat{\boldsymbol{u}} \propto \pm H\left(1\pm\frac{ck_x}{\omega}\right)\sqrt{\frac{\omega}{\omega\pm ck_x}}\frac{\breve{\mathbf{E}}_{\pm}^{(R)}(k_x,\omega)}{-i\omega\eta_0}\cdot\hat{\boldsymbol{u}} \quad (6.8)$$

If we now distinguish the two polarizations x and y, considering (6.4) we obtain:

$$\begin{bmatrix}\breve{E}_{x,\pm}^{(i)}(k_x,\omega)\\ \breve{E}_{y,\pm}^{(i)}(k_x,\omega)\\ \breve{E}_{z,\pm}^{(i)}(k_x,\omega)\end{bmatrix} \propto \begin{bmatrix}\left(1-\left(\frac{ck_x}{\omega}\right)^2\right)H\left(1\pm\frac{ck_x}{\omega}\right)\sqrt{\frac{\omega}{\omega\pm ck_x}}\breve{\mathrm{E}}_{\boldsymbol{x},\pm}^{(R)}(k_x,\omega)\\ H\left(1\pm\frac{ck_x}{\omega}\right)\sqrt{\frac{\omega}{\omega\pm ck_x}}\breve{\mathrm{E}}_{\boldsymbol{y},\pm}^{(R)}(k_x,\omega)\\ -\frac{ck_x}{\omega}\sqrt{1-\left(\frac{ck_x}{\omega}\right)^2}H\left(1\pm\frac{ck_x}{\omega}\right)\sqrt{\frac{\omega}{\omega\pm ck_x}}\breve{\mathrm{E}}_{\boldsymbol{x},\pm}^{(R)}(k_x,\omega)\end{bmatrix} \quad (6.9)$$

Equation (6.9) generalizes (2.17) for both polarizations. In the next sections, we will treat the problem of the scattering of an electric field by a perfectly conductive half-plane and we shall derive the relations in (2.10) and (6.6), employed in the paper for finding the transfer function of the KE+TDS system.

6.2.3 Definition of the scattering problem for the vector potential

We model the blade as a semi-infinite perfectly conductive plane at $z = 0$ for $x_0 > 0$. The total field **E** is considered as the superposition of an incident field $\mathbf{E}^{(i)}$ and a scattered field $\mathbf{E}^{(s)}$, generated, respectively, by the input source $\mathbf{J}^{(i)}$ in the free space and by an induced current $\mathbf{J}^{(s)}$ on the metallic plane. In particular, the tangential component of the total field E on the metallic

plane is zero. As discussed previously, since the optical source is transversely polarized with respect to the metallic plane we consider the input source parallel to the half-plane. For the vector potential, the following relation holds:

$$A_z^{(i)} = A_z^{(s)} = 0 \tag{6.10}$$

We now look for the requirements associated with the vector potential in order to satisfy the following condition on the half-plane:

$$\mathbf{E}_{||}^{(i)} + \mathbf{E}_{||}^{(s)} = 0 \text{ for z = 0 and } x > x_0 \tag{6.11}$$

Using the relation on the electric field in (6.1), (6.10) and (6.11) for the vector potential, we have:

$$\begin{bmatrix} \partial_{xx} + k_0^2 & \partial_{xy} \\ \partial_{xy} & \partial_{yy} + k_0^2 \end{bmatrix} \left(\mathbf{A}^{(i)} + \mathbf{A}^{(s)}\right) = 0 \tag{6.12}$$

Since the operator acting on the vector potential is linear, the condition in (6.12) implies that

$$\mathbf{A}^{(s)}(x, y, 0) = -\mathbf{A}^{(i)}(x, y, 0) + \mathbf{A}_0^{(s)} \text{ for } x > x_0 \tag{6.13}$$

where $\mathbf{A}_0^{(s)}$ is the solution to the equation

$$\begin{bmatrix} \partial_{xx} + k_0^2 & \partial_{xy} \\ \partial_{xy} & \partial_{yy} + k_0^2 \end{bmatrix} \mathbf{A}_0^{(s)} = 0 \tag{6.14}$$

valid on the plane of the blade $z = 0$. We now calculate the operator in the transformed wavevectors Fourier space, $\mathbf{k} = (k_x, k_y, k_z)$ of the spatial coordinate $\mathbf{r} = (x, y, z)$, that is:

$$\begin{bmatrix} -k_x^2 + k_0^2 & -k_x k_y \\ -k_{xy} & -k_y^2 + k_0^2 \end{bmatrix}. \tag{6.15}$$

The determinant of this operator is zero when

$$k_x^2 + k_y^2 = k_0^2 \tag{6.16}$$

i.e., $\mathbf{A}_0^{(s)}$ is a field that propagates parallel to the blade. As we are not interested in these components, we can consider $\mathbf{A}_0^{(s)} = \mathbf{0}$. Hence, the relation in (6.11) can be rewritten as:

$$\mathbf{A}^{(s)}(x, y, 0) = -\mathbf{A}^{(i)}(x, y, 0) \text{ for } x > x_0 \tag{6.17}$$

6.2.4 Solution for the driven wave equation

The scattered field is generated by a 2-D spatial current distribution on the plane $z = 0$:

$$\mathbf{J}(\mathbf{r}) = \mathbf{J}^{(s)}(x, y) 2\pi\delta(z) \tag{6.18}$$

Equivalently, in the 2-D transformed space it holds:

$$\mathbf{J}^{(s)}(x, y) = \int \check{\mathbf{J}}^{(s)}\left(k_x, k_y\right) e^{ik_x x + ik_y y} \frac{dk_x dk_y}{(2\pi)^2} \tag{6.19}$$

Substituting (6.19) into (6.1), we obtain the solution for the scattered electromagnetic potential

$$\mathbf{A}^{(s)}(x, y, z) = -\frac{i}{2} \int \frac{\check{\mathbf{J}}_0^s(k_x, k_y)}{\sqrt{k_0^2 - k_x^2 - k_y^2}} e^{ik_x x + ik_y y + i|z|\sqrt{k_0^2 - k_x^2 - k_y^2}} \frac{dk_x dk_y}{(2\pi)^2} \tag{6.20}$$

or equivalently, we obtain that the Fourier transform on the section $z = 0^+$ of the scattered field is:

$$\check{\mathbf{A}}^{(s)}(k_x, k_y, z = 0^+) = -\frac{i}{2} \frac{\check{\mathbf{J}}_0^s(k_x, k_y)}{\sqrt{k_0^2 - k_x^2 - k_y^2}} \tag{6.21}$$

6.2.5 Scattering current induced by a plane wave

The scattering problem in (6.17) is valid only for $x > x_0$. Hence, we can rewrite the identity in terms of a function that coincides with the opposite incident field on the blade, but is an arbitrary function $\mathbf{f}(x, y)$ for $x < x_0$. With the help of the Heaviside theta function $H(x)$, we define (in both the direct and the transformed space)

$$\mathbf{C}(x, y) = -\mathbf{A}^{(i)}(x, y, 0) H(x - x_0) + \left(1 - H(x - x_0)\right) \mathbf{f}(x, y) \tag{6.22a}$$

$$\check{\mathbf{C}}(k_x,k_y)=\pi\left[\check{\mathbf{f}}(k_x,k_y)-\breve{\mathbf{A}}^{(i)}(k_x,k_y,z=0)\right]+\left[\check{\mathbf{f}}(k_x,k_y)+\breve{\mathbf{A}}^{(i)}(k_x,k_y,z=0)\right]\otimes\left(\frac{i}{k_x}e^{-ik_xx_0}\right) \tag{6.22b}$$

where the symbol $\otimes$ stands for the convolution with respect to k_x. Substituting (6.20) into (6.17) for $z = 0$, we have

$$-\frac{i}{2}\iint\frac{\check{\mathbf{J}}^{(s)}(k_x,k_y)}{\sqrt{k_0^2-k_x^2-k_y^2}}e^{ik_xx+ik_yy}\frac{dk_xdk_y}{(2\pi)^2}=\iint\check{\mathbf{C}}(k_x,k_y)e^{ik_xx+ik_yy}\frac{dk_xdk_y}{(2\pi)^2}=0\ \text{ for } x>x_0 \tag{6.23}$$

The solution of (6.23) must account for the fact that the current is zero where the blade is not present

$$\int e^{ik_yy}\frac{dk_y}{2\pi}\int\check{\mathbf{J}}^{(s)}(k_x,k_y)e^{ik_xx}\frac{dk_x}{2\pi}=0 \tag{6.24}$$

To solve the integral problem in (6.23) and (6.24) for the scattering current $\check{\mathbf{J}}^{(s)}(k_x,k_y)$, we introduce a support function $\check{\mathbf{J}}_{\mathbf{0}}^{(s)}(k_x,k_y,s_x)$ defined as

$$\check{\mathbf{J}}^{(s)}(k_x,k_y)=\int\check{\mathbf{J}}_0^{(s)}(k_x,k_y,s_x)e^{ik_xx_0}\frac{ds_x}{2\pi} \tag{6.25}$$

As long as the term in (6.25) converges, the condition in (6.24) can be simplified in

$$\int\check{\mathbf{J}}_0^{(s)}(k_x,k_y,s_x)e^{[ik_x(x-x_0)]}\frac{dk_x}{2\pi}=0\ \text{ for }\ x<x_0\quad\ \forall k_y,\forall ks_x \tag{6.26}$$

We can look for a function $\check{\mathbf{J}}_{\mathbf{0}}^{(s)}(k_x,k_y,s_x)$ that satisfies the conditions necessary to apply Jordan's lemma in k_x $\forall k_y$, $\forall ks_x$ and that has no poles in the complex lower half-plane im(k_x) < 0: in this case, the condition in (6.26) is verified. If we now impose $\check{\mathbf{f}}(k_x,k_y)=\breve{\mathbf{A}}^{(i)}(k_x,k_y,z=0)$, we obtain that **C**(*x, y*) is also related to the input field $\breve{\mathbf{A}}^{(i)}(k_x,k_y,z=0)$ through an integral relation

$$\check{\mathbf{C}}(k_x,k_y)=\breve{\mathbf{A}}^{(i)}(k_x,k_y,z=0)*\left(\frac{2i}{k_x}e^{-ik_xx_0}\right)=2ie^{-ik_xx_0}\int\frac{\breve{\mathbf{A}}^{(i)}(s_x,k_y,z=0)}{k_x-s_x}e^{-is_xx_0}\frac{ds_x}{2\pi} \tag{6.27}$$

Substituting (6.27) into (6.23), the problem simplifies to:

$$\int \left[\frac{\check{\mathbf{J}}_0^{(s)}(k_x,k_y,s_x)}{\sqrt{k_0^2-k_x^2-k_y^2}} + 4\frac{\breve{\mathbf{A}}^{(i)}(s_x,k_y,z=0)}{k_x-s_x} e^{is_x x_0} \right] * e^{[ik_x(x-x_0)]} \frac{dk_x}{2\pi} = 0 \ , \ x > x_0 \ , \ \forall k_y, \forall k s_x \qquad (6.28)$$

Since $\breve{\mathbf{A}}^{(i)}(s_x, k_y, z=0)$ is a constant in the integral, (6.28) and (6.26) represent the problem of the scattering of a single plane wave by the conductive half-plane. To solve (6.28), we could simply require that $\check{\mathbf{J}}_0^{(s)}(k_x, k_y, s_x) = -4\breve{\mathbf{A}}^{(i)}(s_x, k_y, z=0) * e^{is_x x_0} \frac{\sqrt{k_0^2-k_x^2-k_y^2}}{k_x-s_x}$

However, we note that the function would not satisfy Jordan's lemma, as it is not zero for $|k_x| \rightarrow \infty$, and would not satisfy (6.26). We also note that the term $1/\sqrt{k_0^2 - k_x^2 - k_y^2}$in the integral gives rise to a couple of complex conjugate poles $k_x = \pm\sqrt{k_0^2 - k_y^2}$, and only the pole $k_x = \sqrt{k_0^2 - k_y^2}$ falls in the upper complex plane, being thus relevant for the integration with Jordan's lemma. Then, also the following relation satisfies the condition in (6.28):

$$\check{\mathbf{J}}_0^{(s)}(k_x, k_y, s_x) = -4\breve{\mathbf{A}}^{(i)}(s_x, k_y, z=0) e^{is_x x_0} * \frac{\sqrt{\sqrt{k_0^2-k_y^2}-k_x}\sqrt{\sqrt{k_0^2-k_y^2}-s_x}}{k_x-s_x} \qquad (6.29)$$

Since (6.29) has only a pole in the upper complex plane, it also satisfies (6.26).

6.2.6 Total diffracted field

Summarizing the previous results, the Fourier transform of the field in the section of the blade $z = 0^+$ is such that:

$$\breve{\mathbf{A}}(k_x, k_y, z=0^+) = \mathbf{A}^{(i)}(k_x, k_y, z=0^+) + \mathbf{A}^{(s)}(k_x, k_y, z=0^+) \qquad (6.30)$$

Using (6.21) and (6.29) into (6.13), we obtain

$$\breve{\mathbf{A}}^{(s)}(k_x, k_y, z=0^+) = 2i \int \breve{\mathbf{A}}^{(i)}(s_x, k_y, z=0^+) * \frac{\sqrt{\sqrt{k_0^2-k_y^2}+s_x}}{\sqrt{\sqrt{k_0^2-k_y^2}+k_x}} \frac{e^{[i(s_x-k_x)x_0]}}{(k_x-s_x)} \frac{ds_x}{2\pi} \qquad (6.31)$$

By substituting (6.31) into (6.30), the total field can be propagated using (6.3) for $z > 0$. By letting $k_x = 0$ and $k_y = 0$, we finally obtain (6.6).

6.3 KE+TDS system transfer function

The THz electric field is defined in time, t, and in frequency, ω, by the Fourier relation:

$$\mathbf{e}(\mathbf{r}, t) = 2\mathrm{Re} \int_{-\infty}^{\infty} \mathbf{E}(\mathbf{r}, \omega) e^{-i\omega t} \frac{d\omega}{2\pi} \tag{6.32}$$

Considering z as the propagation coordinate, a spatial Fourier transform for the transverse coordinates x, y is defined as:

$$\breve{\mathbf{E}}\left(k_x, k_y, z, \omega\right) = \iint_{-\infty}^{\infty} \mathbf{E}(x, y, z, \omega)\, e^{-ik_x x - ik_y y} dxdy \tag{6.33}$$

For simplicity we consider an incident field distribution $\mathrm{E}^{(i)}(x, \omega)\hat{y}$ that is invariant and polarized along y, i.e. parallel to the blade edge. The blade is in the plane $z = 0$. At a coordinate $z = 0^+$, the field transmitted by the blade can be calculated with the Sommerfeld integral:

$$\breve{\mathrm{E}}(k_x, z = 0^+, \omega) = \breve{\mathrm{E}}^{(i)}(k_x, \omega) + 2i \int \frac{\sqrt{k_0 + s_x}}{\sqrt{k_0 + k_x}} \breve{\mathrm{E}}^{(i)}(s_x, \omega) \frac{e^{i(s_x - k_x)x_0}}{k_x - s_x} \frac{ds_x}{2\pi} \tag{6.34}$$

For each position of the blade moving along x, the TDS system implements the integral along x and y of the transmitted field for a specific polarization, i.e. for a field polarized along y we collect the quantity: $\iint_{-\infty}^{\infty} \mathbf{E}(x, z = 0^+, \omega) \cdot \hat{y} dxdy$. Or equivalently (i.e. in the Fourier space), the TDS samples the function in $k_x = 0$: $\breve{\mathbf{E}}(k_x = 0, z = 0^+, \omega) \cdot \hat{y}$. Combining this result with the Sommerfeld integral, we find that the map extracted by the KE+TDS in function of the blade position x_0 is:

$$\breve{\mathrm{E}}(k_x = 0, \omega) = \breve{\mathrm{E}}^{(i)}(k_x = 0, \omega) - \int_{-\infty}^{\infty} \frac{2i}{s_x} \sqrt{1 + \frac{cs_x}{\omega}} \breve{\mathrm{E}}^{(i)}(s_x, \omega) e^{is_x x_0} \frac{ds_x}{2\pi} \tag{6.35}$$

Deriving along x_0 and transforming back in the temporal domain we get the reconstructed field:

$$\mathrm{e}_R(x_0,t) \propto \mathrm{Re}\iint_{-\infty}^{\infty}\sqrt{1+\frac{cs_x}{\omega}}\,\breve{\mathrm{E}}^{(i)}(s_x,\omega)e^{is_x x_0-i\omega t}\frac{ds_x d\omega}{(2\pi)^2} =$$

$$\iint_{-\infty}^{\infty}\breve{T}(k_x,\omega)\breve{\mathrm{E}}^{(i)}(k_x,\omega)e^{ik_x x_0-i\omega t}\frac{dk_x d\omega}{(2\pi)^2} \tag{6.36}$$

That leads to the transfer function:

$$\breve{T}(k_x,\omega) \equiv \begin{cases}\sqrt{1+\frac{ck_x}{\omega}} & \text{for } k_x > -\frac{\omega}{c} \\ 0 & \text{for } k_x < -\frac{\omega}{c}\end{cases} \tag{6.37}$$

7 REFERENCES

[1] O. Mitrofanov, I. Brener, R. Harel, J. D. Wynn, L. N. Pfeiffer, K. W. West and J. Federici, "Terahertz near-field microscopy based on a collection mode detector," *Appl. Phys. Lett.* **77**, 22, 3496-3498 (2000).

[2] O. Mitrofanov, I. Brener, M. C. Wanke, R. R. Ruel, J. D. Wynn, A. J. Bruce and J. Federici, "Near-field microscope probe for far infrared time domain measurements," *Appl. Phys. Lett.* **77,** 4, 591-593 (2000).

[3] D. V. Palanker, G. M. H. Knippels, T. I. Smith and H. A. Schwettman, "Fast IR imaging with sub-wavelength resolution using a transient near-field probe," *Nucl. Instrum. Meth. Phys. Res. Sect. B* **144**, 1-4, 240-245 (1998).

[4] D. V. Palanker, G. M. H. Knippels, T. I. Smith and H. A. Schwettman, "IR microscopy with a transient photo-induced near-field probe (tipless near-field microscopy)," *Opt. Commun.* **148**, 4-6, 215-220 (1998).

[5] S. Hunsche, M. Koch, I. Brener and M. C. Nuss, "THz near-field imaging," *Opt. Commun.* **150**, 1-6, 22-26 (1998).

[6] B. Knoll and F. Keilmann, "Near-field probing of vibrational absorption for chemical microscopy," *Nature* **399**, 134-137 (1999).

[7] H.-T. Chen, R. Kersting and G. C. Cho, "Terahertz imaging with nanometer resolution," *Appl. Phys. Lett.* **83**, 15, 3009-3011 (2003).

[8] J. Z. Xu and X.-C. Zhang, "Optical rectification in an area with a diameter comparable to or smaller than the center wavelength of terahertz radiation," *Opt. Lett.* **27,** 12, 1067-1069 (2002).

[9] T. Yuan, S. P. Mickan, J. Z. Xu, D. Abbott and X.-C. Zhang, "Towards an apertureless electro-optic T-ray microscope," CFD3, *The Conference of Laser and Ellectro-Optics (CLEO).* Long Bech, CA (2002).

[10] T. Yuan, J. Z. Xu and X.-C. Zhang, “Development of terahertz wave microscopes,” *Infrared Phys. Technol.* **45,** 5-6, 417-425 (2004).

[11] F. Buccheri, M. Peccianti, A. Busacca, T. Ozaki and R. Morandotti, “Spatial and spectral properties of small area THz generation for sub-wavelength microscopy,” *35th Int. Conf. Infrared Millimeter and Terahertz Waves.* Rome, Italy (2010).

[12] H. Lin, C. Fumeaux, B. M. Fischer and D. Abbott, “Modelling of sub-wavelength THz sources as Gaussian apertures,” *Opt. Express* **18,** 17, 17672-17683 (2010).

[13] H. Lin, C. Fumeaux, B. S. Y. Ung and D. Abbott, “Comprehensive modeling of THz microscope with a sub-wavelength source,” *Opt. Express* **19,** 6, 5327-5338 (2011).

[14] E. Brüdermann, H.-W. Hübers and M. F. Kimmitt, *Terahertz Techniques.* Springer-Verlag Berlin Heidelberg (2012).

[15] K. E. Peiponen, A. Zeitler & K.-G. Makoto, *Terahertz Spectroscopy and Imaging.* Springer-Verlag Berlin Heidelberg, USA (2013).

[16] X.-C. Zhang and J. Xu, *Introduction to THz Wave Photonics.* Springer Science+Business Media, New York (2010).

[17] J. M. Chamberlain, R. E. Miles, C. E. Collins and D. P. Steenson, “New directions in terahertz technology,” *Proceedings of the NATO Advanced Research Workshop.* Château de Bonas, Castéra-Verduzan, France. Kluwer Academic Publishers, Dordrecht, The Netherlands (1997).

[18] T. W. Crowe, T. C. Grein, R. Zimmerman and P. Zimmerman, “Correction to "progress toward solid-state local oscillators at 1 THz",” *IEEE Microw Guided Wave Lett.* **6**, 10, 207-208 (1996).

[19] H. Eisele, A. Rydberg and G. Haddad, “Recent advances in the performance of InP Gunn devices and GaAs TUNNETT diodes for the 100-300-GHz frequency range and above,” *Trans. Microw Theory Tech.* **48**, 4, 626-631 (2000).

[20] CLF (Central Laser Facility), Rutherford Appleton Laboratory Annual Report. Édit Wyborn B (Rutherford Appleton Laboratory, Oxford, United Kingdom) (2002).

[21] J. Faist, F. Capasso, D. L. Sivco, C. Sirtori, A. L. Hutchinson and A. Y. Cho, "Quantum Cascade Laser," *Sci* 2**64**, 5158, 553-556 (1994).

[22] D. M. Mittleman, "Frontiers in terahertz sources and plasmonics," *Nature Photon* **7**, 9, 666-669 (2013).

[23] D. H. Auston, "Picosecond optoelectronic switching and gating in silicon," *Appl. Phys. Lett.* **26**, 3, 101-103 (1975).

[24] C. H. Lee, "Picosecond optoelectronics switching in GaAs," *Appl. Phys. Lett.* **30**, 2, 84-86 (1977).

[25] C. H. Lee and V. K. Mathur, "Picosecond photoconductivity and its applications," *IEEE J. Quantum Electron.* **17**, 10, 2098-2112 (1981).

[26] G. A. Mourou, C. Stancampiano, A. Antonetti and A. Orszag, "Picosecond microwave pulses generated with a subpicosecond laser driven semiconductor switch," *Appl. Phys. Lett.* **39**, 4, 295-365 (1981).

[27] J. A. Valdmanis, G. A. Mourou and C. W. Gabel, "Subpicosecond electrical sampling," *IEEE J. Quantum Electron.* **19**, 4, 664-667 (1983).

[28] D. H. Auston, "Impulse response of photoconductors in transmission lines," *IEEE J. Quantum Electron.* **19**, 4, 639 (1983).

[29] P. R. Smith, D. H. Auston and M. C. Nuss, "Subpicosecond photoconductive dipole antennas," *IEEE J. Quantum Electron.* **24**, 2, 255-260 (1988).

[30] M. V. Exter, C. Fattinger and D. Grischkowsky, "Terahertz time-domain spectroscopy of water vapor," *Opt. Lett.* **14**, 20,1128-1130 (1989).

[31] D. Grischkowsky, S. Keiding, M. van Exter and C. Fattinger, "Far-infrared time-domain spectroscopy with terahertz beams of dielectrics and semiconductors," *J. Opt. Soc. Am B* **7**, 10, 2006-2015 (1990).

[32] A. Rice, Y. Jin, X. F. Ma, X.-C. Zhang, D. Bliss, J. Larkin and M. Alexander, "Terahertz optical rectification from <110> zinc-blende crystals," *Appl. Phys. Lett.* **64**, 11, 1324-1326 (1994).

[33] Q. Wu and X.-C. Zhang, "Free-space electro-optic sampling of terahertz beams," *Appl. Phys. Lett.* **67**, 24, 3523-3525 (1995).

[34] R. W. Boyd, *Nonlinear Optics.* Academic Press, USA, 2nd Edition (2003).

[35] L. Xu, X.-C. Zhang and D. H. Auston, "Terahertz beam generation by femtosecond optical pulses in electro-optic materials," *Appl. Phys. Lett.* **61,** 15, 1784 (1992).

[36] X.-C. Zhang, Y. Jin and X. F. Ma, "Coherent measurement of THz optical rectification from electro-optic crystals," *Appl. Phys. Lett.* **61**, 23, 2764 (1992).

[37] T. J. Carrig, G. Rodriguez, T. S. Clement, A. J. Taylor and K. R. Stewart, "Scaling of terahertz radiation via optical rectification in electro-optic crystals," *Appl. Phys. Lett.* **66,** 2, 121 (1995).

[38] A. Nahata, A. S. Weling and T. F. Heinz, "A wideband coherent terahertz spectroscopy system using optical rectification and electro-optic sampling," *Appl. Phys. Lett.* **69**, 16, 2321 (1996).

[39] P. Y. Han and X.–C. Zhang, "Coherent, broadband midinfrared terahertz beam sensors," *Appl. Phys. Lett.* **73**, 21, 3049 (1998).

[40] Q. Chen and X.-C. Zhang, "Polarization modulation in optoelectronic generation and detection of terahertz beams," *Appl. Phys. Lett.* **74**, 23, 3435 (1999).

[41] M. Bass, P. A. Franken, J. F. Ward and G. Weinreich, "Optical rectification," *Phys. Rev. Lett.* **9**, 11, 446-448 (1962).

[42] K. H. Yang, P. L. Richards, and Y. R. Shen, "Generation of far-infrared radiation by picosecond light pulses in $LiNbO_3$," *Appl. Phys. Lett.* **19**, 9, 320 (1971).

[43] X. F. Ma and X.–C. Zhang, "Determination of ratios between nonlinear-optical coefficients by using subpicosecond optical rectification," *J. Opt. Soc. Am. B* **10**, 7, 1175-1179 (1993).

[44] P. N. Saeta, B. I. Greene and S. L. Chuang, "Short terahertz pulses from semiconductor surfaces: the importance of bulk difference-frequency mixing," *Appl. Phys. Lett.* **63**, 25, 3482-3484 (1993).

[45] A. Corchia, C. M. Ciesla, D. D. Arnone, E. H. Linfield, M. Y. Simmons and M. Pepper, "Crystallographic orientation dependence of bulk optical rectification," *J. Mod. Optics* **47**, 11, 1837-1845 (2000).

[46] X.-C. Zhang, X. F. Ma, Y. Jin, T.-M. Lu, E. P. Boden, P. D. Phelps, K. R. Stewart and C. P. Yakymyshyn, "Terahertz optical rectification from a nonlinear organic crystal," *Appl. Phys. Lett.* **61**, 26, 3080-3082 (1992).

[47] T. Yajima and N. Takeuchi, "Spectral properties and tunability of far-infrared difference frequency radiation produced by picosecond laser pulses," *Jpn. J. Appl. Phys.* **10**, 7, 907-915 (1971).

[48] X.-C. Zhang and D. H. Auston, "Optoelectronic measurement of semiconductor surfaces and interfaces with femtosecond optics," *J. Appl. Phys.* **71**, 1, 326 (1992).

[49] A. M. Sinyukov and L. M. Hayden, "Generation and detection of terahertz radiation with multilayered electro-optic polymers films," *Opt. Lett.* **27**, 1, 55-57 (2002).

[50] B. I. Greene, J. F. Federici, D. R. Dykaar, R. R. Jones and P. H. Bucksbaum, "Interferometric characterization of 160 fs far-infrared light pulses," *Appl. Phys. Lett.* **59**, 8, 893 (1991).

[51] E. Budiarto, J. Marglies, S. Jeong, S. Son and J. Bokor, "High-intensity terahertz pulses at 1-kHz repetition rate," *IEEE J. Quantum Electron.* **59**, 10, 893 (1996).

[52] P. U. Jepsen, C. Winnewisser, M. Schall, V. Schyja, S. R. Keiding and H. Helm, "Detection of THz pulses by phase retardation in lithium tantalate," *Phys. Rev. E* **53**, 4, R3052 (1996).

[53] A. Nahata, D. A. Auston, T. F. Heinz and C. Wu, "Coherent detection of freely propagating terahertz radiation by electro-optic sampling," *Appl. Phys. Lett.* **68**, 2, 150 (1996).

[54] Q. Wu, M. Litz and X.-C. Zhang, "Broadband detection capability of ZnTe electro-optic field detectors," *Appl. Phys. Lett.* **68**, 21, 2924-2926 (1996).

[55] Q. Wu, T. Hewitt and X.-C. Zhang, "Two-dimensional electro-optic imaging of THz beams," *Appl. Phys. Lett.* **69**, 8, 1026-1028 (1996).

[56] S. Kono, M. Tani and K. Sakai, "Coherent detection of mid-infrared radiation up to 60 THz with an LT-GaAs photoconductive antenna," *IEEE Proc. Optoelectron.* **147**, 3, 105-109 (2002).

[57] Y.-S. Lee, *Principles of Terahertz Science and Technology.* Springer Science+Business Media, LLC, New York, USA (2009).

[58] M. Reid and R. Fedosejevs, "Quantitative comparison of terahertz emission from (100) InAs surfaces and a GaAs large-aperture photoconductive switch at high fluences," *Appl. Opt.* **44**, 1, 149-153 (2005).

[59] C. H. Townes and G. Melnick, "Atmospheric transmission in the far-infrared at the south pole and astronomical applications," *Publ. Astron. Soc. Pac.* **102**, 357-367 (1989).

[60] H. P. Roser, "Heterodyne spectroscopy for submillimeter and far infrared wavelengths," *Infrared Phys.* **32**, 385-407 (1991).

[61] B. B. Hu and M. C. Nuss, "Imaging with terahertz waves," *Opt. Lett.* **20**, 16, 1716-1718 (1995).

[62] E. Abbe, "E. Beitrage zur heorie des mikroskops und der mikroskopischen wahrnehmung," *Arch Mikr Anat* **9**, 1, 413-418 (1873).

[63] E. Abbe, "A contribution to the theory of the microscope and the nature of microscopic vision," *Bristol Naturalists' Society.* p 200-261 (1874).

[64] L. Rayleigh, "On the theory of optical images with special reference to the microscope," *Philos. Mag.* **42**, 255, 167-195 (1896).

[65] O. Mitrofanov, M. Lee, J. W. P. Hsu, L. N. Pfeiffer, K. W. West, J. D. Wynn and J. F. Federici, "Terahertz pulse propagation through small apertures," *Appl. Phys. Lett.* **79**, 7, 907 (2001).

[66] M. A. Seo, A. J. L. Adam, J. H. Kang, J. W. Lee, K. J. Ahn, Q. H. Park, P. C. M. Planken and D. S. Kim, "Near field imaging of terahertz focusing onto rectangular apertures," *Opt. Express* **16**, 25, 20484-20489 (2008).

[67] F. Federici, O. Mitrofanov, M. Lee, J. W. P. Hsu, I. Brener, R. Harel, J. D. Wynn, L. N. Pfeiffer and K. W. West, "Terahertz near-field imaging," *Phys. Med. Biol.* **47**, 21, 3727-3734 (2002).

[68] Q. Chen, Z. Jiang, G. X. Xu and X.-C. Zhang, "Near-field terahertz imaging with a dynamic aperture," *Opt. Lett.* **25**, 15, 1122-1124 (2000).

[69] H. T. Chen, S. Kraatz, G. C. Cho, and R. Kersting, "Identification of a resonant imaging process in apertureless near-field microscopy," *Phys. Rev. Lett*. **93,** 267401 (2004).

[70] P. C. M. Planken, C. E. W. M. van Rijmenam and R. N. Schouten, "Opto-electronic pulsed THz systems," *Semicond. Sci. Technol.* **20,** S121-S127 (2005).

[71] H. Zhan, V. Astley, M. Hvasta, J. A. Deibel, D. M. Mittleman and Y.-S. Lim, "The metal-insulator transition in *VO*2 studied using terahertz apertureless near-field microscopy," Appl. Phys. Lett. **91,** 162110 (2007).

[72] H. Bethe, "Theory of diffraction by small holes," *Phys. Rev.* **66**, 7-8, 163-182 (1944).

[73] A. H. Firester, M. E. Heller and P. Sheng, "Knife-edge scanning measurements of subwavelength focused light beams," *Appl. Opt.* **16**, 7, 1971-1974 (1977).

[74] Y. Wang, Z. Zhao, Z. Chen, L. Zhang, and K. Kang, "Analysis of terahertz pulse propagation through a dielectric edge," *Proc. SPIE* **7277,** 72770R-1–72770R-8 (2009).

[75] A. Dobroiu, M. Yamashita, Y. N. Ohshima, Y. Morita, C. Otani, and K. Kawase, "Terahertz imaging system based on a backward-wave oscillator," *Appl. Opt.* **43,** 5637–5646 (2004).

[76] H Lin, C. Fumeaux, B. M. Fischer, and D. Abbott, "Modelling of subwavelength THz sources as Gaussian apertures," *Opt. Express* **18,** 17672–17683 (2010).

[77] A. Podzorov, A. Wojdyla, and G. Gallot, "Beam waist measurement for terahertz time-domain spectroscopy experiments," *Opt. Lett.* **35,** 7, 901-903 (2010).

[78] R. Dickhoff, C. Jastrow, A. Steiger, R. Muller, T. Keline-Ostmann, and T. Schrader, "Characterization of THz Beams," in *Proc. Quantum Electron Laser Sci. Conf.*, OSA Technical Digest (CD) (Optical Society of America), JThB116 (2011).

[79] A. Gurtler, C. Winnewisser, H. Helm, and P. Uhd Jensen, "Terahertz pulse ¨ propagation in the near field and the far field," *J. Opt. Soc. Amer. A* **17,** 74–83 (2000).

[80] P. Uhd Jepsen, R. H. Jacobsen, and S. R. Keidling, "Generation and detection of terahertz pulses from biased semiconductor antennas," *J. Opt. Soc. Amer. B* **13,** 2424–2436 (1996).

[81] A. Bitzer, H. Hel, and M. Walther, "Beam-profiling and wavefront-sensing of THz pulses at the focus of a substrate-Lens," *IEEE J. Select. Topics Quantum Electron.* **14,** 476–480 (2008).

[82] Q. Wu, T. D. Hewitt, and X. C. Zhang, "Two-dimensional electro-optic imaging of THz beams," *Appl. Phys. Lett.* **69,** 1026–1028 (1996).

[83] Z. P. Jiang and X. C. Zhang, "2D measurement and spatio-temporal coupling of few-cycle THz pulses," *Opt. Express* **5,** 243–248 (1999).

[84] Z. P. Jiang and X. C. Zhang, "Terahertz imaging via electro-optic effect," *IEEE Trans. Microwave Theory Tech.* **47,** 2644–2650 (2000).

[85] R. M. O'Connell and R. A. Vogel, "Abel inversion of knife-edge data from radially symmetric pulsed laser beams," *Appl. Opt.* **26,** 13, 2528–2532 (1987).

[86] M. A. C. De Araújo, R. Silva, E. De Lima, D. P. Pereira, and P. C. De Oliveira, "Measurement of Gaussian laser beam radius using the knife-edge technique: improvement on data analysis," *Appl. Opt.* **48,** 2, 393-396 (2009).

[87] O. Jedrkiewicz, M. Clerici, E. Rubino and P. D. Trapani, "Generation and control of phase-locked conical wave packets in type-I seeded optical parametric amplification," *Phys. Rev. A* **80**, 3, 033813 (2009).

[88] O. Jedrkiewicz, A. Picozzi, M. Clerici, D. Faccio and P. D. Trapani, "Emergence of X-shaped spatiotemporal coherence in optical waves," *Phys. Rev. Lett.* **97**, 24, 243903 (2006).

[89] O. Jedrkiewicz, M. Clerici, A. Picozzi, D. Faccio and P. D. Trapani, "X-shaped space-time coherence in optical parametric generation," *Phys. Rev. A* **76**, 3, 033823 (2007).

[90] A. Gatti, E. Brambilla, L. Caspani, O. Jedrkiewicz and L. Lugiato, "X entanglement: The nonfactorable spatiotemporal structure of biphoton correlation," *Phys. Rev. Lett.* **102**, 22, 223601 (2009).

[91] L. Caspani, E. Brambilla and A. Gatti, "Tailoring the spatiotemporal structure of biphoton entanglement in type-I parametric down-conversion," *Phys. Rev. A* **81**, 3, 033808 (2010).

[92] M. C. Nuss and J. Orenstein, "Terahertz time-domain spectroscopy," *in Millimeter and Submillimeter Wave Spectroscopy of Solids.* Springer-Verlag Berlin Heidelberg, Germany (1998).

[93] R. Dorn, S. Quabis and G. Leuchs, "The focus of light - linear polarization breaks the rotational symmetry of the focal spot," *J. Mod. Opt.* **50,** 12, 1917-1926 (2003).

[94] M. Born and E. Wolf, *Principles of Optics: Electromagnetic Theory of Propagation, Interference and Diffraction of Light*. Cambridge Univ. Press. Cambridge, U.K (1990).

[95] M. Yi, K. Lee, J.-D. Song and J. Ahn, "Terahertz phase microscopy in the sub-wavelength regime," *Appl. Phys. Lett.* **100**, 16, 161110 (2012).

[96] M. Schall and P. U. Jepsena, "Above-band gap two-photon absorption and its influence on ultrafast carrier dynamics in ZnTe and CdTe," *Appl. Phys. Lett.* **80**, 25, 4771 (2002).

[97] R. M. Sharma, *Physical properties of semiconductor.* Scribd. http://www.scribd.com/doc/191628434/physical-properties-of-semiconductors (2013).

[98] T. F. Boggess, K. M. Bohnert, K. Mansour, S. C. Moss, I. W. Boyd and A. L. Smirl, "Simultaneous measurement of the 2-photon coefficient and free-carrier cross-section above the bandgap of crystalline silicon," *IEEE J. Quantum Electron.* **22**, 2, 360-368 (1986).

[99] B. E. A. Saleh and M. C. Teich, *Fundamentals of Photonics.* John Wiley & Sons, Inc., New Jersey, USA, 2nd Edition (2007).

[100] Z. Liping, G. Jianghong and X. Long, "Non-diffraction fringes produced by thin biprism," *Opt. Appl.* **XLII**, 4 (2012).

[101] M. Peccianti, M. Clerici, A. Pasquazi, L. Caspani, S. P. Ho, F. Buccheri, J. Ali, A. Busacca, T. Ozaki and R. Morandotti, "Exact reconstruction of THz sub-λ source features in knife-edge measurements," *IEEE J. Sel. Topics Quantum Electron.* **19**, 1, 8401211 (2013).

[102] A. Tomasino, A. Parisi, S. Stivala, P. Livreri, A. C. Cino, A. C. Busacca, M. Peccianti and R. Morandotti, "Wideband THz time domain spectroscopy based on optical rectification and electro-optic sampling," *Sci. Rep.* **3**, 3116, 1-8 (2013).

[103] B. Ferguson and X.-C. Zhang, "Material for terahertz science and technology," *Nature Materials* **1**, 26-33 (2002).

[104] A. Nahata and T. F. Heinz, "Detection of freely propagating terahertz radiation by use of optical second-harmonic generation," *Opt. Lett.* **23**, 1, 67-69 (1998).

[105] D. J. Cook, J. X. Chen, E. A. Morlino and R. M. Hochstrasser, "Terahertz-field-induced second-harmonic generation measurements of liquid dynamics," *Chem. Phys. Lett.* **309**, 3-4, 221-228 (1999).

[106] J. Dai, X. Xie and X.-C. Zhang, "Detection of broadband terahertz waves with a laser-induced plasma in gases," *Phys. Rev. Lett.* **97**, 10, 103903 (2006).

[107] N. Karpowicz, J. Dai, X. Lu, Y. Chen, M. Yamaguchi, H. Zhao, X.-C. Zhang, L. Zhang, C. Zhang, M. Price-Gallagher, C. Fletcher, O. Mamer, A. Lesimple and K. Johnson, "Coherent heterodyne time-domain spectrometry covering the entire "terahertz gap"," *Appl. Phys. Lett.* **92**, 0111131, 1-3 (2008).

[108] X. Lu and X.-C. Zhang, "Balanced terahertz wave air-biased-coherent detection," *Appl. Phys. Lett.* **98**, 15, 151111 (2011).

[109] T. W. Ebbesen, H. J. Lezec, H. F. Ghaemi, T. Thio and P. A. Wolf, "Extraordinary optical transmission through sub-wavelength hole arrays," *Nature* **391**, 667-669 (1998).

[110] Y. Takakura, "Optical resonance in a narrow slit in a thick metallic screen," *Phys. Rev. Lett.* **86**, 24, 5601-5603 (2001).

[111] A. Novitsky, A. M. Ivinskaya, M. Zalkovskij, R. Malureanu, P. U. Jepsen and A. V. Lavrinenk, "Non-resonant terahertz field enhancement in periodically arranged nanoslits," *J. Appl. Phys.* **112**, 074318, 1-10 (2012).

[112] H. J. Lezec, A. Degiron, E. Devaux, R. A. Linke, L. Martin-Moreno, F. J. Garcia-Vidal and T. W. Ebbesen, "Beaming light from a subwavelength aperture," *Sci* **297**, 5582, 820-822 (2002).

[113] P. F. Chimento, P. F. A. Alkemade, N. V. Kuzmin, G. W. T. Hooft, J. Bosman and E. R. Eliel, "A subwavelength slit as a quarter-wave retarder," *Opt. Express* **19**, 24, 24219-24227 (2011).

[114] D. C. Adams, S. Inampudi, T. Ribaudo, D. Slocum, S. Vangala, N. A. Kuhta, W. D. Goodhue, V. A. Podolskiy and D. Wasserman, "Funneling light through a subwavelength aperture with epsilon-near-zero materials," *Phys. Rev. Lett.* **107**, 13, 133901 (2001).

[115] R. W. Terhune, P. D. Maker and C. M. Savage, "Optical harmonic generation in calcite," *Phys. Rev. Lett.* **8**, 10, 404-406 (1962).

[116] M. Clerici, D. Faccio, L. Caspani, M. Peccianti, O. Yaakobi, B. E. Schmidt, M. Shalaby, F. Vidal, F. Legare, T. Ozaki and R. Morandotti, "Spectrally resolved wave-mixing between near- and far-infrared pulses in gas," *New J. Phys.* **15**, 125011 *(2013)*.

[117] D. You and P. H. Bucksbaum, "Propagation of half-cycle far infrared pulses," *J. Opt. Soc. Am. B* **14**, 7, 1651-1655 (1997).

[118] S. Feng, H. G. Winful and R. W. Hellwarth, "Gouy shift and temporal reshaping of focused single-cycle electromagnetic pulses," *Opt. Lett.* **23**, 5, 385-387 (1998).

[119] A. B. Ruffin, J. V. Rudd, J. F. Whitaker, S. Feng and H. G. Winful, "Direct observation of the Gouy phase shift with single-cycle terahertz pulses," *Phys. Rev. Lett.* **83**, 17, 3410-3413 (1999).

8 LIST OF PUBLICATIONS

8.1 Peer Review Journal Publications

[1] S. P. Ho, A. Mazhorova, M. Shalaby, M. Peccianti, M. Clerici, A. Pasquazi, Y. Ozturk, J. Ali, and R. Morandotti, "Sub-wavelength terahertz beam profiling of a terahertz source via an all-optical knife-edge technique," Scienctific Reports 5, 8851 (2015).

[2] M. Peccianti, M. Clerici, A. Pasquazi, L. Caspani, S. P. Ho, F. Buccheri, J. Ali, A. Busacca, T. Ozaki, and R. Morandotti, "Exact reconstruction of THz sub-λ source features in knife-edge measurements," IEEE Journal of Selected Topics in Quantum Electronics 19 (1) 8401211 (2013).

[3] M. K. Bhuyan, F. Courvoisier, S. P. Ho, O. Jedrkiewicz, S. Recchia, P. Di Trapani, J. M. Dudley, "Laser micro- and nanostructuring using femtosecond Bessel beams," European Physical Journal: Special Topics 199 (1) 101-110 (2011).

8.2 Conferences and Presentations

8.2.1 Invited talks:

[1] S. P. Ho, M. Peccianti, M. Clerici, A. Pasquazi, L. Caspani, F. Buccheri, J. ALi, A. Busacca, and R. Morandotti, "Time-resolved approach for exact reconstruction of sub-wavelength THz sources via knife-edge technique," Photonics North, Ottawa, Canada, June 3-5, 2013.

[2] S. P. Ho, M. Clerici, M. Peccianti, F. Buccheri, A. Busacca, T. Ozaki, J. Ali, R. Morandotti, “Sub-wavelength scale THz source via optical rectification and its spatio-temporal properties,” Photonics Prague, Prague, Czech Republic, August 24-26, 2011.

[3] M. Clerici, S. P. Ho, A. Mazhorova, M. Peccianti, A. Pasquazi, L. Razzari, D. Faccio, J. Ali, and R. Morandotti, "Broadband terahertz detection in solid state media," SPIE/COS Photonics Asia, Beijing, China, October 9-11, 2014.

[4] P. Tannouri, M. Clerici, M. Peccianti, A. Pasquazi, M.J. Strain, S. P. Ho, I. Rowe, K.A. Rutkowska, M. Sorel, R. Morandotti, "Nonlinear notch shift in AlGaAs Bragg grating

waveguides", International Conference on Nanoscience, Engineering & Advanced Computing (ICNEAC), Narsapur, Andhra Pradesh, India, July 8-10, 2011.

8.2.2 Conferences:

[1] M. Clerici, S.-P. Ho, A. Mazhorova, M. Peccianti, A. Pasquazi, L. Razzari, J. Ali, R. Morandotti, “Micro-slit assisted coherent broadband terahertz detection,” Conference on Lasers and Electro-Optics/Europe and the European Quantum Electronics Conference (CLEO®/Europe-EQEC), Munich, Germany, June 21-25, 2015 (oral).

[2] S. P. Ho, A. Mazhorova, M. Shalaby, M. Peccianti, M. Clerici, A. Pasquazi, Y. Ozturk, R. Morandotti, "Rectangular-shaped sub-wavelength terahertz beam profiling via an all-optical knife-edge technique," Conference in Lasers and Electro-Optics (CLEO), San Jose, USA, June 8-13, 2014 (poster).

[3] A. Mazhorova, S. P. Ho, M. Clerici, M. Peccianti, A. Pasquazi, L. Razzari, J. Ali and R. Morandotti, "Terahertz field induced second harmonic coherent detection scheme based on a biased nonlinear micro-slit," Conference in Lasers and Electro-Optics (CLEO), San Jose, USA, June 8-13, 2014 (oral).

[4] M. Clerici, S. P. Ho, A. Mazhorova, M. Peccianti, A. Pasquazi, L. Razzari, J. Ali, and R. Morandotti, "Fully-coherent terahertz detection via biased nonlinear micro-slit," International Conference on Metamaterials, Photonic Crystals and Plasmonics (META), Singapore, May 20-23, 2014 (oral).

[5] S. P. Ho, A. Mazhorova, M. Shalaby, M. Peccianti, M. Clerici, A. Pasquazi, Y. Ozturk, J. Ali, R. Morandotti, "Grating-patterned sub-wavelength terahertz beam characterization via an all-optical knife-edge technique," Photonics North, Montreal, Canada, May 28-30, 2014 (oral).

[6] A. Mazhorova, S.P. Ho, M. Clerici, M. Peccianti, A. Pasquazi, L. Razzari, J. Ali and R. Morandotti, "Terahertz field induced second harmonic coherent detection scheme based on a biased nonlinear micro-slit," Photonics North, Montreal, Canada, May 28-30, 2014 (oral).

[7] S. P. Ho, A. Mazhorova, M. Shalaby, M. Peccianti, M. Clerici, A. Pasquazi, Y. Ozturk, J. Ali, and R. Morandotti, "Grating-patterned sub-wavelength terahertz beam profiling through an all-optical knife-edge technique," 8th North American ION Conference (IONS-NA 8), Montreal, Canada, May 25-27, 2014 (oral).

[8] S. P. Ho, A. Mazhorova, M. Shalaby, M. Peccianti, M. Clerici, A. Pasquazi, Y. Ozturk, J. Ali, and R. Morandotti, "Grating-patterned sub-wavelength terahertz beam profiling through an all-optical knife-edge technique," Colloque de Plasma-Québec, Montreal, Canada, June 4-6, 2014 (poster).

[9] M. Clerici, A. Mazhorova, S.-P. Ho, M. Peccianti, A. Pasquazi, L. Razzari, J. Ali and R. Morandotti, "On chip broadband terahertz detection via four-wave mixing in electrically biased silica micro-slits," Nonlinear Photonics (NP), Barcelona, Spain, July 27-31, 2014 (oral).

[10] S. P. Ho, M. Shalaby, M. Peccianti, M. Clerici, A. Pasquazi, Y. Ozturk, J. Ali, R. Morandotti, "Terahertz characterization via an all-optical, ultra-thin-knife-edge technique," Conference in Lasers and Electro-Optics (CLEO), San Jose, USA, June 11-13, 2013 (poster).

[11] S. P. Ho, M. Shalaby, M. Peccianti, M. Clerici, A. Pasquazi, Y. Ozturk, J. Ali and R. Morandotti, "An all-optical, zero-thickness knife-edge for terahertz characterization," Photonics North, Ottawa, Canada, June 3-5, 2013 (oral).

[12] S. P. Ho, M. Shalaby, M. Peccianti, M. Clerici, A. Pasquazi, Y. Ozturk, J. Ali, R. Morandotti, "An all-optical, ultra-thin-knife-edge technique for terahertz characterization," Canadian Association of Physicists (CAP) Congress, Montreal, Canada, May 27-31, 2013 (poster).

[13] S. P. Ho, M. Peccianti, M. Clerici, A. Pasquazi, L. Caspani, F. Buccheri, J. Ali, A. Busacca, R. Morandotti, "Time-resolved approach for exact reconstruction of sub-wavelength THz sources via knife-edge technique," Canadian Association of Physicists (CAP) Congress, Montreal, Canada, May 27-31, 2013 (poster).

[14] S. P. Ho, M. Peccianti, M. Clerici, A. Pasquazi, L. Caspani, F. Buccheri, J. Ali, A. Busacca and R. Morandotti, "Exact reconstruction of sub-wavelength THz source profile via combination of knife-edge technique and time-domain spectroscopy," International Workshop on Optical Terahertz Science and Technology (OTST), Kyoto, Japan, April 1-5, 2013 (poster).

[15] S. P. Ho, M. Shalaby, M. Peccianti, M. Clerici, A. Pasquazi, Y. Ozturk, J. Ali and R. Morandotti, "A novel optical approach for THz radiation features characterization," International Workshop on Optical Terahertz Science and Technology (OTST), Kyoto, Japan, April 1-5, 2013 (oral).

[16] P. Tannouri, M. Clerici, M. Peccianti, M.J. Strain, A. Pasquazi, S. P. Ho, K. A. Rutkowska, M. Sorel and R. Morandotti, "Notch nonlinear frequency blue shift and observation of second harmonic generation in AlGaAs Bragg grating waveguides", Photonics North, Montreal, Canada, June 6-8, 2012 (oral).

[17] M. Peccianti, S. P. Ho, F. Buccheri, M. Clerici, A. Busacca, T. Ozaki, J. Ali, R. Morandotti, "Space-time features of THz emission from optical rectification in sub-wavelength areas," Conference in Lasers and Electro-Optics (CLEO), Baltimore, USA, May 1-6, 2011 (oral).

[18] S. P. Ho, M. Clerici, M. Peccianti, F. Buccheri, A. Busacca, T. Ozaki, J. Ali, R. Morandotti, "Spatio-temporal characteristics of THz emission at the subwavelength scale via optical rectification," OSA Topical Meeting, Optical Sensors (Sensors), Toronto, Canada, June 12-15, 2011 (oral).

[19] M. Peccianti, S. P. Ho, F. Buccheri, M. Clerici, A. Busacca, T. Ozaki, J. Ali, R. Morandotti, "Space-time features of THz emitted from optical rectification occurring in sub-wavelength scales," International Workshop on Optical Terahertz Science and Technology (OTST), Santa Barbara, USA, March 13-17, 2011 (poster).

[20] S. P. Ho, M. Peccianti, F. Buccheri, M. Clerici, A. Busacca, T. Ozaki, J. Ali, R. Morandotti, "Space-time features of THz emitted from optical rectification occurring in sub-wavelength scales," Photonics North, Ottawa, Canada, May 16-18, 2011 (oral).

[21] M. Clerici, M. Peccianti, M.J. Strain, P. Tannouri, A. Pasquazi, S.P. Ho, I. Rowe, K. A. Rutkowska, M. Sorel, R. Morandotti, "Notch nonlinear frequency shift in AlGaAs Bragg grating waveguides", Conference in Lasers and Electro-Optics (CLEO), Baltimore, USA, May 1-6, 2011 (oral).

[22] M. Peccianti, S. P. Ho, F. Buccheri, M. Clerici, A. Busacca, T. Ozaki, J. Ali, R. Morandotti, “Space-time features of THz emission from optical rectification in sub-wavelength areas”, Conference in Lasers and Electro-Optics (CLEO), Baltimore, USA, May 1-6, 2011 (oral).

[23] P. Tannouri, M. Clerici, M. Peccianti, A. Pasquazi, M.J. Strain, S.P. Ho, I. Rowe, K.A. Rutkowska, M. Sorel, R. Morandotti, "Nonlinear notch shift in AlGaAs Bragg grating waveguides", 7th International Workshop on Fibre Optics and Passive Components (WFOPC), Montreal, Canada, July 13-15, 2011 (poster).

[24] P. Tannouri, M.J. Strain, M. Clerici, M. Peccianti, A. Pasquazi, S.P. Ho, I. Rowe, K.A. Rutkowska, M. Sorel, R. Morandotti, "Nonlinear notch blue-shift in AlGaAs Bragg grating waveguides", Advanced Photonics Congress, Toronto, Canada, June 12-15, 2011 (oral).

[25] P. Tannouri, M. Clerici, M. Peccianti, A. Pasquazi, M.J. Strain, S.P. Ho, I. Rowe, K.A. Rutkowska, M. Sorel, R. Morandotti, "Exploitation d'effets non-linéaires dans un guide d'ondes d'AlGaAs à réseau de Bragg pour la commutation tout-optique", Colloque de Plasma-Québec, Montreal, Canada, May 25-27, 2011 (poster).

[26] P. Tannouri, M. Clerici, M. Peccianti, A. Pasquazi, M.J. Strain, S.P. Ho, I. Rowe, K.A. Rutkowska, M. Sorel, R. Morandotti, "Nonlinear notch blue-shift in AlGaAs Bragg grating waveguides", Photonics North, Ottawa, Canada, May 16-18, 2011 (oral).